Ψ_k **Scientific Highlight Of The Month**

No. 160 **January 2026**

Investigating finite temperature effects by means of the alloy analogy model

Sergiy Mankovsky[1,*], Jan Minar[2], and Hubert Ebert[1]

[1] *Department Chemie, Physikalische Chemie, Universität München, Butenandtstr. 5-13, 81377 München, Germany*

[2] *New Technologies-Research Centre, University of West Bohemia, Univerzitni 8, 30100 Pilsen, Czech Republic*

Abstract

Accounting for a finite temperature within first-principles electronic structure calculations for a solid allows to investigate the temperature dependence of its properties. These concern the equilibrium properties, as for instance the magnetization and magnetic anisotropy in magnetic materials, as well as the nonequilibrium, e.g. transport or spectroscopic, properties. Usually, the temperature regime of interest may reach up to several thousands Kelvin. At least for metals only a relatively weak re-population of the electronic states occurs in the vicinity of the Fermi energy for this temperature regime leading usually to a negligible impact on their physical properties. Much more pronounced temperature induced changes of the properties may be associated with different types of thermally induced excitations, as for example lattice vibrations and spin fluctuations. In magnetic materials in particular transverse spin fluctuations can be easily excited already at room temperature with a strong impact on their magnetic properties. In the present review we describe an approach, which allows to account for the impact of thermally induced spin and lattice excitations on the electronic structure and related properties making use of the so-called alloy analogy. The KKR (Korringa-Kohn-Rostoker) Green function method is a very convenient tool for corresponding electronic structure calculations, as it is a well established scheme to investigate disordered alloys by making use of the single-site Coherent Potential Approximation (CPA) alloy theory. As the dynamics of phonons and magnons is much slower compared to the electronic propagation the corresponding thermal displacements and spin fluctuations give rise to a quasi static disorder in the system. The corresponding thermal average can therefore be treated as the chemical disorder in an alloy. Neglecting the correlation between the thermal displacements and spin fluctuations of neighboring atoms, as it is well justified for not too low temperatures, allows to treat them within the mean-field approximation and in particular to use the CPA for the necessary thermal averaging. This approach, developed by the authors and called alloy analogy model (AAM), has been applied during the last years to deal with the temperature dependence of a large variety of properties. The great success and applicability of this rather simple and efficient approach is demonstrated by results obtained for various magnetic, response as well as spectroscopic properties.

*manpc@cup.uni-muenchen.de

Investigating finite temperature effects by means of the alloy analogy model

Sergiy Mankovsky

Department Chemie, Physikalische Chemie, Universität München, Butenandtstr. 5-13, 81377 München, Germany

Jan Minar

New Technologies-Research Centre, University of West Bohemia, Univerzitni 8, 30100 Pilsen, Czech Republic

Hubert Ebert

Department Chemie, Physikalische Chemie, Universität München, Butenandtstr. 5-13, 81377 München, Germany

April 2025

Abstract. Accounting for a finite temperature within first-principles electronic structure calculations for a solid allows to investigate the temperature dependence of its properties. These concerns the equilibrium properties, as for instance the magnetization and magnetic anisotropy in magnetic materials, as well as the non-equilibrium, e.g. transport or spectroscopic, properties. Usually, the temperature regime of interest may reach up to several thousands Kelvin. At least for metals only a relatively weak re-population of the electronic states occurs in the vicinity of the Fermi energy for this temperature regime leading usually to a negligible impact on their physical properties. Much more pronounced temperature induced changes of the properties may be associated with different types of thermally induced excitations, as for example lattice vibrations and spin fluctuations. In magnetic materials in particular transverse spin fluctuations can be easily excited already at room temperature with a strong impact on their magnetic properties. In the present review we describe an approach, which allows to account for the impact of thermally induced spin and lattice excitations on the electronic structure and related properties making use of the so-called alloy analogy. The KKR (Korringa-Kohn-Rostoker) Green function method is a very convenient tool for corresponding electronic structure calculations, as it is a well established scheme to investigate disordered alloys by making use of the single-site Coherent Potential Approximation (CPA) alloy theory. As the dynamics of phonons and magnons is much slower compared to the electronic propagation the corresponding thermal displacements and spin fluctuations give rise to a quasi static disorder in the system. The corresponding thermal average can therefore be treated as the chemical disorder in an alloy. Neglecting the correlation between the thermal displacements and spin fluctuations of neighboring atoms, as it is well justified for not too low temperatures, allows to treat them within the mean-field approximation and in particular to use the CPA for the necessary thermal averaging. This approach, developed by the authors and called alloy analogy model (AAM), has been applied

during the last years to deal with the temperature dependence of a large variety of properties. The great success and applicability of this rather simple and efficient approach is demonstrated by results obtained for various magnetic, response as well as spectroscopic properties.

1. Introduction

A finite temperature may have a crucial influence on the electronic structure of a solid and as a consequence on its various properties. Accordingly, it is of great interest to describe the modification of the electronic structure by a finite temperature while staying within the framework of density-functional theory. The most common thermal effect for a solid is represented by the temperature-dependent Fermi-Dirac distribution function characterizing the population of the electronic states. Accounting for this in a self-consistent way when calculating the electron spin and charge densities, one should in principle obtain the temperature induced change of the electronic states and corresponding changes of the physical and chemical properties of a material. This effect can be crucial for the thermodynamics of solids, in particular for their phase stability; but substantial changes of the electronic structure are normally observed only at very high temperatures (see, e.g. Ref. [1]). As for moderate temperatures only small changes of the Fermi-Dirac distribution occur in a narrow region around the Fermi energy its impact can normally be ignored when considering transport and optical properties of metallic systems for temperatures up to $\sim 1 - 2000$ K. For that reason we ignore here the impact of changes of the Fermi-Dirac distribution with temperature i.e. of a finite electronic temperature.

Another important source for changes of the electronic structure with temperature are temperature induced lattice and spin excitations, i.e. phonons and magnons. A way to take this mechanism into account is to perform as a first step first-principles calculations for the phonon and magnon eigen states and energies $\omega(\vec{q})$. In the case of magnetic systems, corresponding results can already be used to obtain the temperature dependent magnetization in the low-temperature limit by accounting for the temperature dependent population of the magnon states [2, 3]. Dealing in addition explicitly with the coupling of the electron with the phonons or magnons, respectively, allows to determine the resulting renormalization of the electronic structure. This can be represented by the spectral function $A(\vec{k}, E)$ [4, 5, 6, 7, 8]

$$A(\vec{k}, E) = -\frac{1}{\pi} \frac{|\Im\Sigma(\vec{k}, E)|}{[E - E_0(\vec{k}) - \Re\Sigma(\vec{k}, E)]^2 + [\Im\Sigma(\vec{k}, E)]^2}\,, \tag{1}$$

where $E_0(\vec{k})$ stands for the non-distorted band dispersion and $\Sigma(\vec{k}, E)$ is a complex self-energy. For phonons the self-energy contains full information about the electron-phonon interaction [9] and is calculated making use of the electron-phonon spectral function $\alpha^2 F(\omega)$ (see, e.g. Ref. [10, 11, 12]). In the case of magnetic systems, the electron-magnon self-energy has to be determined in a corresponding way [13, 14].

The temperature dependence of the self-energy is determined by the population of the respective boson, i.e., phonon or magnon, states raising with temperature and leading to a corresponding temperature dependent modification of the electronic structure expressed by Eq. (1) [4, 6, 15]. The resulting renormalization of the electronic band structure can be monitored by angular resolved photoemission that shows in particular the so-called phonon kink [16]. In pure and ordered metallic systems at room temperature, the electron-phonon scattering is the dominant mechanism giving rise to the electrical resistivity [17, 4]. As the self energy determines the relaxation time $\tau^{-1}(\vec{k},T) = \frac{2\pi}{\hbar}\Im\Sigma(\vec{k},T)$ that represents the electron-phonon scattering within the Boltzmann theory of electronic transport, it can be used to calculate the transport properties as electrical or thermal resistivity [4, 18, 19, 20].

Calculating X-ray absorption spectra another simpler concept taken over from X-ray diffraction is widely used to account for finite temperatures. In this case lattice vibrations are represented by the Debye-Waller (DW) factor, which simulates the observed temperature induced damping of the absorption signal by the weighting factor $e^{-W(T)}$, with $W(T) \approx 2k^2u^2(T)$ where k and $u^2(T)$ are the wave number and mean square displacement, respectively [21]. A more sophisticated approach was used for example in a many-body description of X-ray photoelectron diffraction (XPD) accounting for the Debye-Waller and Franck-Condon factors in XPD spectra at finite temperature [22], as well as for the impact of displaced core wave functions [23]. The treatment of temperature induced lattice vibrations in terms of uncorrelated displacements of the atoms was used also to describe the temperature dependence of transport properties [3]. The positions for the displaced atoms at finite temperature were obtained in a first step via ab-initio molecular dynamics calculations. The resistivity was subsequently calculated using the Landauer-Büttiker formalism. The results obtained this way for non-magnetic systems showed good agreement with that obtained in an alternative way Ref. [18]. A similar approach was used by the authors to account for temperature induced spin fluctuations in magnetic materials, which also led to good agreement with experiment. In fact, this approach is rather close to the alloy analogy model (AAM) discussed below.

Obviously, we do not give a comprehensive overview of all approaches to account for finite temperature effects when dealing with the electronic structure of solids and their related properties. As this is an important issue, one can find in the literature a large variety of works on a model and ab-initio level. Here we highlighted two ways to account for thermal excitations treating them as quasi particles or as local thermal perturbations. From a formal point of view, the first one is surly more satisfying than the second one. One the other hand, the second one is computationally much less demanding. More important, however, accounting for the finite electronic lifetime due to thermally induced disorder via the AAM or similar approaches allows to describe the temperature dependence of many electronic properties in a quantitative way. This will be demonstrated by corresponding work published by the authors during the last 15 years.

Finally, it should be mentioned that the alloy analogy concept was suggested many years ago by Hubbard when studying the instability of the ferromagnetic state on the basis of the model Hubbard Hamiltonian [24, 25]. In this approach the time average, which arises because of the continuous rearrangement of the electron spin, is represented by a configurational average that can be handled as for the alloy problem. For the electrons having spin character σ, the corresponding two types of sites are seen as two different atoms A and B with the electron states in atoms $\epsilon_A = 0$ and $\epsilon_B = U$, respectively (with U the intra-atomic Coulomb repulsion parameter), depending on whether the states are occupied or not by the electrons with the opposite spin $-\sigma$. Such a system could be seen as an effective alloy $A_{1-n_{-\sigma}}B_{n_{-\sigma}}$, with $n_{-\sigma}$ standing for the average number of electrons per site with spin $-\sigma$. While the coherent potential approximation (CPA) alloy thepry was not used by Hubbard, it was applied later by other authors, dealing with generalized Hubbard Hamiltonians and in particular with real binary alloy systems [26, 27, 28].

The idea to take over the techniques - in particular the CPA - to deal with the configurational average in case of a disordered alloy to deal with fluctuating states on the atomic sites can of course be applied as well to handle other types of disorder in a system. This is demonstrated in this contribution for the temperature induced lattice vibrations and spin fluctuations that can be seen as quasi-static when compared to the dynamics of the electrons and give rise to temperature dependent disorder with respect to the spin-dependent electronic potential.

2. Theory: electronic structure and properties of disordered alloys

2.1. Electronic structure in terms of Bloch states and Green functions

The vast majority of ab-initio methods for calculating the electronic structure of solids is based on the variational method for solving the Kohn-Sham equation, and rely on translational symmetry. The latter property implies that the solutions of the Kohn-Sham equations, $\psi_{j\vec{k}}(\vec{r})$, obey the Bloch theorem and that the corresponding Bloch states are eigen functions of the translation operator

$$\mathcal{T}_{\vec{R}}\psi_{j\vec{k}}(\vec{r}) = e^{i\vec{k}\cdot\vec{R}}\,\psi_{j\vec{k}}(\vec{r})\,. \tag{2}$$

As a consequence, states characterized by different wave vectors $\vec{k}$ are orthogonal. This simplifies the solution of the band structure problem essentially when using a variational basis set of Bloch-like functions characterized by the same $\vec{k}$ vector to represent the wave function $\psi_{j\vec{k}}(\vec{r})$. This leads in particular to a secular equation with finite dimension for each $\vec{k}$-vector

$$\left[\underline{\underline{H}}^{\vec{k}} - E_{j\vec{k}}\,\underline{\underline{S}}^{\vec{k}}\right]\,\underline{\alpha}_{j\vec{k}} = \underline{0} \tag{3}$$

with the Hamiltonian and overlap matrices, $\underline{\underline{H}}^{\vec{k}}$ and $\underline{\underline{S}}^{\vec{k}}$, referring to the basis functions and $E_{j\vec{k}}$ and $\underline{\alpha}_{j\vec{k}}$ the associated eigenvalues and -vectors, respectively. There is a large

number of methods and corresponding computer codes available that are based on this [29].

On the other hand, it is often very advantageous to represent the solution of the Kohn-Sham equation in terms of the electronic Green's function (GF), having in particular a direct access to the density of states $n(E)$ and electron density $n(\vec{r})$, respectively:

$$n(E) = -\frac{1}{\pi}\Im \,\mathrm{Tr} \int d^3r\, G^+(\vec{r},\vec{r},E) \tag{4}$$

$$n(\vec{r}) = -\frac{1}{\pi}\Im \,\mathrm{Tr} \int^{E_\mathrm{F}} dE\, G^+(\vec{r},\vec{r},E)\ . \tag{5}$$

where $G^+(\vec{r},\vec{r}\,',E)$ is the retarded single-particle Green function.

The use of the Green function offers many advantages when dealing with embedded subsystems, response functions, spectroscopy, disorder or the many-body problem. To a large extent this is due to the Dyson equation that allows to express the Green function $G^+(\vec{r},\vec{r}\,',E)$ of a complex system on the basis of that of a simpler reference system ($G_0^+(\vec{r},\vec{r}\,',E)$) and the arbitrary perturbing Hamiltonian $\mathcal{H}_\mathrm{pert}(\vec{r})$ that connects the two systems:

$$G^+(\vec{r},\vec{r}\,',E) = G_0^+(\vec{r},\vec{r}\,',E) + \int_\Omega \mathrm{d}^3r\,'' \, G_0^+(\vec{r},\vec{r}\,'',E) \mathcal{H}_\mathrm{pert}(\vec{r}\,'')\, G^+(\vec{r}\,'',\vec{r}\,',E)\ , \tag{6}$$

with Ω the region for which $\mathcal{H}_\mathrm{pert}(\vec{r})$ has to be accounted for. For a substitutional impurity this would include the atomic cell of the impurity and the region of the neighboring host atoms that are distorted by the impurity.

For practical use, the retarded single-particle Green function $G^+(\vec{r},\vec{r}\,',E)$ can be determined via the so-called Lehmann spectral representation [30]

$$G^+(\vec{r},\vec{r}\,',E) = \lim_{\epsilon\to 0}\sum_{j\vec{k}} \frac{\psi_{j\vec{k}}(\vec{r})\,\psi^\dagger_{j\vec{k}}(\vec{r}\,')}{E-E_{j\vec{k}}+i\epsilon}\ , \tag{7}$$

that, however, needs the whole spectrum of the eigenvalue solutions for the underlying electronic Hamiltonian making the scheme inefficient for applications.

2.2. Green function within multiple scattering theory

An alternative to this is offered by the multiple scattering theory-based KKR (Korringa-Kohn-Rostoker) formalism. The approach leads to the following expression for $G^+(\vec{r},\vec{r}\,',E)$ [31, 32, 33, 34]

$$\begin{aligned} G^+(\vec{r},\vec{r}\,',E) = &\sum_{\Lambda\Lambda'} Z^m_\Lambda(\vec{r},E)\tau^{mn}_{\Lambda\Lambda'}(E)Z^{n\times}_{\Lambda'}(\vec{r}\,',E) \\ &- \delta_{mn}\sum_\Lambda Z^n_\Lambda(\vec{r},E)J^{n\times}_{\Lambda'}(\vec{r}\,',E)\Theta(r'_n-r_n) \\ &+ J^n_\Lambda(\vec{r},E)Z^{n\times}_{\Lambda'}(\vec{r}\,',E)\Theta(r_n-r'_n)\ , \end{aligned} \tag{8}$$

given here in the most general fully relativistic formulation. Here $\vec{r}, \vec{r}\,'$ refer to points within atomic cells around sites $\vec{R}_m, \vec{R}_n$, respectively, with $\Phi^n_\Lambda(\vec{r}, E) = \Phi_\Lambda(\vec{r}_n, E) = \Phi_\Lambda(\vec{r} - \vec{R}_n, E)$ being a a spin-angular function centered at site $\vec{R}_n$. In Eq. (8), the functions Z^n_Λ and J^n_Λ stand for the regular and irregular, respectively, solutions to the single-site Dirac equation for site n with the associated single-site scattering t-matrix $t^n_{\Lambda\Lambda'}$. The corresponding scattering path operator $\tau^{nn'}_{\Lambda\Lambda'}$ accounts for all scattering events connecting the sites n and n'. For the spin-angular representation used here, the combined quantum number $\Lambda = (\kappa, \mu)$ stands for the relativistic spin-orbit and magnetic quantum numbers κ and μ, respectively [35, 32, 33].

The matrix representation of scattering path operator with $\tau^{nn'}_{\Lambda\Lambda'} = [\underline{\underline{\tau}}^{nn'}]_{\Lambda\Lambda'}$ is given in real space representation by a solution of the following equation of motion:

$$\underline{\tau}^{nn'}(E) = \underline{t}^n(E)\delta_{nn'} + \underline{t}^n(E) \sum_{k \neq n} \underline{G}^{\,0,nk}(E) \underline{\tau}^{kn'}(E) \; , \tag{9}$$

For a finite system this equation is solved straightforwardly by a matrix inversion [36]:

$$\underline{\underline{\tau}}(E) = \left[\underline{t}(E)^{-1} - \underline{\underline{G}}^0(E)\right]^{-1} \; . \tag{10}$$

The inverse matrix $\underline{\underline{\tau}}^{-1}(E)$ determines the so-called real-space KKR matrix $\underline{\underline{M}}(E) = \left[\underline{t}(E)^{-1} - \underline{\underline{G}}^0(E)\right]$. The double underline indicates matrices with respect to the site indices n and relativistic quantum numbers Λ. Thus, their dimension is determined by the number of sites (N) in the system and the angular momentum cut-off l_{max}.

Dealing with a three-dimensional periodic system, Eq. (10) can be solved exactly by Fourier transformation, given by the expression [37, 38]

$$\underline{\tau}^{nn'}(E) = \frac{1}{\Omega_{\rm BZ}} \int_{\Omega_{\rm BZ}} d^3k \left[(\underline{t}(E)^{-1} - \underline{G}^0(\vec{k}, E) \right]^{-1} e^{i\vec{k}\cdot(\vec{R}_n - \vec{R}_{n'})} \; , \tag{11}$$

with the (reciprocal space) structure constants matrix $\underline{G}^0(\vec{k}, E)$ being the Fourier transformed of the real-space structure constants matrix $\underline{G}^0(E)$.

As it was pointed out above, the GF $G^+(\vec{r}, \vec{r}\,', E)$ gives access to most electronic properties as indicated above for the electron density and the density of states (DOS). For a more detailed representation of the electronic structure, the Bloch spectral function $A^{\rm B}(\vec{k}, E)$ may be used that is defined via the Fourier transformed Green function $G^+(\vec{r}, \vec{r}\,', E)$ as follows [31]:

$$A^{\rm B}(\vec{k}, E) = -\frac{1}{\pi} \Im \, {\rm Tr} \sum_{n,m} e^{i\vec{k}\cdot(\vec{R}_n - \vec{R}_m)} \int d^3r G^+(\vec{r} + \vec{R}_n, \vec{r} + \vec{R}_m, E) \; . \tag{12}$$

2.3. Configurational averaging for random alloys via the CPA

As was pointed out by Faulkner [39], the KKR method is one of the few first-principles methods which can be generalized to describe the electronic structure for ordered solids as well as for disordered alloys without making use of the super cell technique. The Green function formalism is particularly useful when dealing with the electronic structure of disordered systems. By using the concept of the molecular field, Soven [40] introduced the Coherent Potential Approximation (CPA) approach when dealing with disordered

substitutional alloys. The central idea of the CPA is represented by Fig. 1. It introduces a hypothetical effective CPA medium playing the role of a molecular field, which is constructed such that it represents the configurational average for the alloy. In its

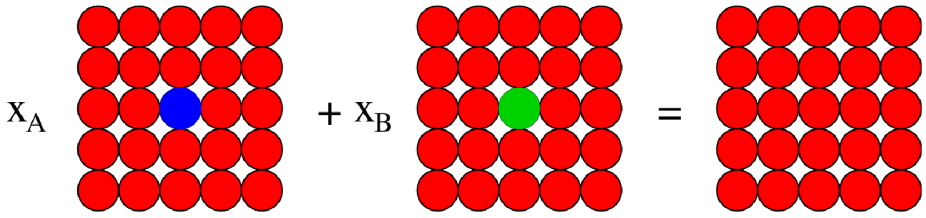

Figure 1. Basic idea of the CPA: the embedding of one of the components of an alloy A_xB_{1-x} (with $x_A = x$ and $x_B = 1 - x$) into the CPA medium should not change its properties if the concentration-weighted average is taken.

standard formulation, the CPA makes use of the single-site approximation (see Fig. 1), that implies that the occupation of neighboring sites is uncorrelated. Within the KKR approach the CPA medium is determined by requiring that for a random substitutional A_xB_{1-x} alloy the embedding of an A- or B-atom into the CPA medium should on the average lead to no additional scattering [34, 41]. This is expressed by the following equation

$$x\,\underline{\tau}_{\mathrm{A}}^{nn} + (1-x)\,\underline{\tau}_{\mathrm{B}}^{nn} = \underline{\tau}_{\mathrm{CPA}}^{nn}\ , \tag{13}$$

where the component-projected scattering path operators

$$\underline{\tau}_{\alpha}^{nn} = \left[(\underline{t}_{\alpha}^{-1} - (\underline{t}_{\mathrm{CPA}})^{-1} + (\underline{\tau}_{\mathrm{CPA}})^{-1}\right]^{-1} \tag{14}$$

characterize the embedding of the alloy component α into the CPA medium according to Eq. (6). These quantities together with the corresponding component-related wave functions $Z_{\Lambda}^{\alpha}(\vec{r}, E)$ and $J_{\Lambda}^{\alpha}(\vec{r}, E)$ give access to the component-specific Green function $G_{\alpha}^{+}(\vec{r}, \vec{r}', E)$ via Eq. (8) and with this to all component-specific properties of an alloy. Corresponding results for the disordered ferromagnetic alloy fcc-$Ni_{0.8}Pd_{0.2}$ are shown in Fig. 2. The left panel gives the spin-resolved band structure in terms of the Bloch spectral function $A_{\sigma}^{\mathrm{B}}(\vec{k}, E)$ that can be seen as the Fourier transform of the real space Green function $G_{\sigma}^{+}(\vec{r}, \vec{r}', E)$, while the middle and right panels give the spin-resolved element-projected density of states $n_{\sigma}^{\alpha}(E)$ for $\alpha =$ Ni and Pd, respectively. Comparison of $A_{\sigma}^{\mathrm{B}}(\vec{k}, E)$ on the left panel with the dispersion relation $E_{j\sigma}(\vec{k})$ of fcc-Ni clearly shows the smearing-out of the energy bands for the alloy in particular in the regime of the d-states, that implies a finite life time of the electronic states and reflects the fact that for the disordered alloy the wave vector $\vec{k}$ is not a good quantum number. As a consequence of the band smearing, the fine structure present in the DOS for pure Ni is washed out for the case of Ni-projected DOS $n_{\sigma}^{\mathrm{Ni}}(E)$ for $Ni_{0.8}Pd_{0.2}$. Furthermore, the width of the $A_{\sigma}^{\mathrm{B}}(\vec{k}, E)$ functions for each $\vec{k}$ point can be interpreted as a measure for the electronic life time to be used in the calculation of the residual resistivity on the basis of the Boltzmann formalism [43].

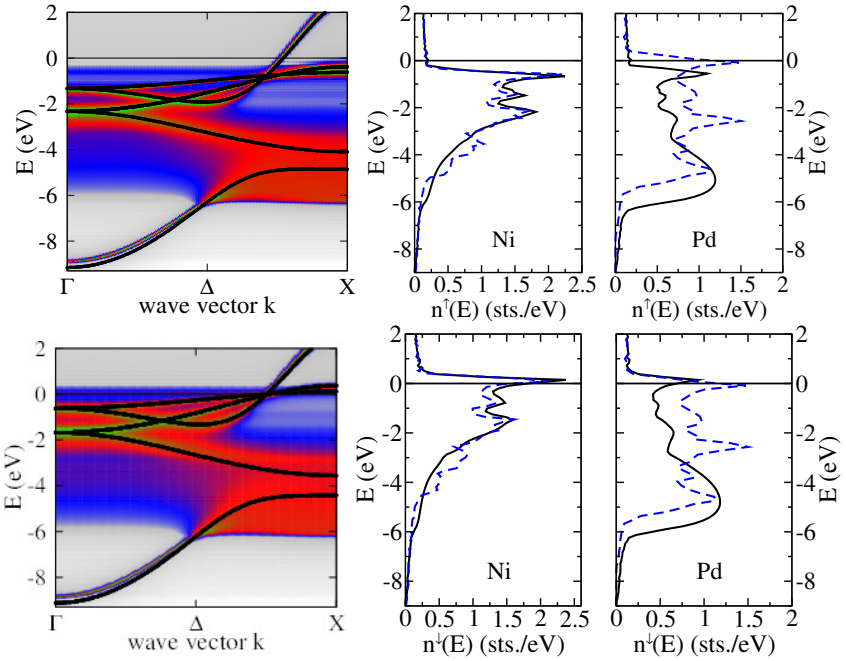

Figure 2. Left: spin-resolved Bloch spectral function $A^{\mathrm{B}}_{\sigma}(\vec{k},E)$ of the disordered ferromagnetic alloy fcc-$Ni_{0.8}Pd_{0.2}$ calculated on the basis of the CPA. Middle and right column: corresponding spin-resolved partial density of states $n^{\alpha}_{\sigma}(E)$ for $\alpha =$ Ni and Pd, respectively. The top and bottom row give results for spin up and down, respectively. As a reference the dispersion relation $E_{j\vec{k}\sigma}$ of pure Ni is superimposed as a black line to $A^{\mathrm{B}}_{\sigma}(\vec{k},E)$ (left). In addition $n^{\mathrm{Ni}}_{\sigma}(E)$ for pure ferromagnetic Ni (middle) and of $n^{\mathrm{Pd}}_{\sigma}(E)$ for pure paramagnetic Pd (right) are included in the figures as dashed lines [42].

It is important to note that the concept of the CPA is not restricted to alloys but can be applied to any type of disorder making use of the alloy analogy model [26, 27, 28, 44] which will be discussed below.

2.4. Treatment of response quantities, vertex corrections

In the following special attention will be paid to the response quantities of materials, for which any type of disorder plays a key role and should be properly taken into account.

A rather general basis for corresponding investigations is provided by Kubo's linear response formalism [45]. This gives access to the response shown by an observable induced by the perturbation that are represented by the operators B and A, respectively. In the case of $A = \hat{j}$ and $B = \hat{j}$ standing both for current density operators, one is led to the Kubo equation [45] for the conductivity

$$\sigma_{\mu\nu} = V \int_0^{(k_B T)^{-1}} d\lambda \int_0^{\infty} dt \ < \hat{j}_{\nu} \hat{j}_{I,\mu}(t + i\hbar\lambda) > e^{i(\omega + i\delta)t} \ , \tag{15}$$

consisting primarily of a current-current correlation function.

For a practical application of the Kubo equation the electronic system is represented by a single-particle density matrix. Imposing more and more restrictions one is led to the sequence Kubo-Bastin [46], Kubo-Středa [47] and the Kubo-Greenwood [48] equation, respectively. The most general Kubo-Bastin equation giving in particular access to the full conductivity tensor $\underline{\sigma}$ is given by the following expression [46]

$$\sigma_{\mu\nu} = \frac{i\hbar}{\Omega}\int_{-\infty}^{\infty} dE f(E) \mathrm{Tr}\left\langle \hat{j}_\mu \frac{dG^+(E)}{dE}\hat{j}_\nu \delta(E-\hat{H}) - \hat{j}_\mu \delta(E-\hat{H})\hat{j}_\nu \frac{dG^-(E)}{dE}\right\rangle_c \tag{16}$$

with $\nu = (x, y, z)$ denoting Cartesian coordinates, $f(E)$ the Fermi-Dirac distribution function and $G^{\pm}(E) = (E - \hat{H} \pm i\delta)^{-1}$ the retarded and advanced Green function operators, and Ω denoting the volume of the unit cell. The simpler Kubo-Středa equation gives access to full conductivity tensor only in the athermal limit $T_{el} = 0$ K, i.e. it accounts for the contribution of the electrons at the Fermi energy. The well known Kubo-Greenwood equation

$$\sigma_{\mu\nu} = \frac{\hbar}{\pi V}\mathrm{Tr}\left\langle \hat{j}_\mu \Im G^+ \hat{j}_\nu \Im G^+ \right\rangle_c . \tag{17}$$

gives only the the symmetric part of the electrical conductivity tensor. It should be noted that for other response functions the Kubo-Bastin-like equation has to be used. Dealing with a disordered alloy, the subscript c in Eqs. 16 and 17 indicates an average over all configurations for the distribution of the alloy components under the constrain of their concentrations. Adopting a fully relativistic formulation for Eq. (8) [32, 33] one gets in a natural way access to all spin-orbit induced properties as magnetoresistance and anomalous Hall effect (AHE) [49, 50] given in the latter case by the anti-symmetric part of $\underline{\sigma}$.

A scheme to account for the configurational average when calculating the conductivity tensor for an alloy has been worked out by Butler [51] within the framework of the KKR-CPA formalism. This leads in a natural way to two contributions to the conductivity:

$$\sigma_{\mu\nu} = \sigma^0_{\mu\nu} + \sigma^1_{\mu\nu} \tag{18}$$

with the site-diagonal and site-off-diagonal contributions, $\tilde{\sigma}^0_{\mu\nu}$ and $\tilde{\sigma}^1_{\mu\nu}$, respectively [52]

$$\sigma^0_{\mu\nu} = -\frac{4m^2}{\pi\hbar^3\Omega}\sum_\alpha \sum_{\substack{\Lambda_1,\Lambda_2\\ \Lambda_3,\Lambda_4}} x_\alpha \,\mathrm{Tr}\, \tilde{J}^{\alpha\mu}_{\Lambda_1\Lambda_2}\tau^{\mathrm{CPA},00}_{\Lambda_2\Lambda_3} J^{\alpha\nu}_{\Lambda_3\Lambda_4}\tau^{\mathrm{CPA},00}_{\Lambda_4\Lambda_1} \tag{19}$$

$$\sigma^1_{\mu\nu} = -\frac{4m^2}{\pi\hbar^3\Omega}\sum_{\alpha,\beta} \sum_{\substack{\Lambda_1,\Lambda_2\\ \Lambda_3,\Lambda_4}} x_\alpha x_\beta \,\mathrm{Tr}\, \tilde{J}^{\alpha\mu}_{\Lambda_1\Lambda_2}\left[(1-\chi\,\omega)^{-1}\chi\right]_{\substack{\Lambda_1\Lambda_2\\ \Lambda_3\Lambda_4}} \tilde{J}^{\beta\nu}_{\Lambda_3\Lambda_4} , \tag{20}$$

where the quantities $J^{\alpha\mu}_{\Lambda\Lambda'}$ are matrix elements of the μ-component of the current density operator $\vec{j}$ for the alloy component α, and $\tilde{J}^{\alpha\mu}_{\Lambda_1\Lambda_2}$ stands for renormalized matrix elements involving, in addition, the component projected scattering path operators $\underline{\tau}^\alpha$. The

quantity $\chi^{\Lambda_1\Lambda_2}_{\Lambda_3\Lambda_4}$ represents a lattice sum over products of scattering path operators $\tau^{\mathrm{CPA}0n}_{\Lambda_1\Lambda_2}\tau^{\mathrm{CPA}n0}_{\Lambda_3\Lambda_4}$ with $n \neq 0$ and for that reason has four indices. This summation can be performed by Fourier transformation leading to a Brillouin zone integral over the product of two Fourier transformed scattering path operators $\tau^{\mathrm{CPA}}_{\Lambda_1\Lambda_2}(\vec{k}, E)$. The additional factor $[(1-\chi\,\omega)^{-1}]^{\Lambda_1\Lambda_2}_{\Lambda_3\Lambda_4}$ in Eq. (20) represents the so-called vertex corrections accounting for the difference between the exact configurational average $\langle\hat{j}_\mu \Im G^+ \hat{j}_\nu \Im G^+\rangle_c$ and the approximated value $\langle\hat{j}_\mu \Im G^+\rangle_c\ \langle\hat{j}_\nu \Im G^+\rangle_c$, that corresponds to the scattering-in terms of the Boltzmann formalism. A corresponding scheme to calculate the resistivity of disordered systems within the TB-LMTO-GF-CPA formalism that also accounts for the vertex corrections has been developed by Turek et al. [53], while the spin-polarized relativistic KKR (SPRKKR) based formulation is given in Refs. [54].

As an example of an application of this formalism to realistic materials, we represent the residual resistivity ρ calculated for disordered alloy $Cu_{1-x}Zn_x$, obtained with (solid line) and without (dashed line) vertex corrections. Fig. 3 represents ρ as a function of concentration x, demonstrating a significant impact of vertex corrections for this alloy system, leading to a strong modification of the resistivity.

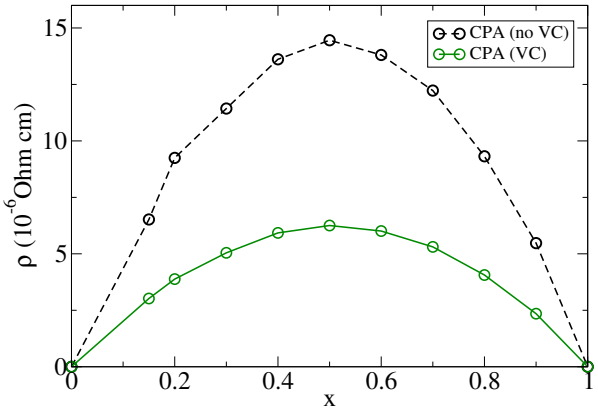

Figure 3. Residual resistivity of random $Cu_{1-x}Zn_x$ alloys, i.e. for $T = 0$ K. The dashes line gives the CPA results neglecting vertex corrections, whereas the solid line corresponds to the results accounting for them.

Concerning the AHE, one has to stress that the anomalous Hall conductivity (AHC) is non-vanishing only for the systems with broken time-reversal symmetry. It general, it can be splitted into the so-called intrinsic (related to the Berry curvature and fully determined by the features of all occupied electronic states, i.e. Fermi sea) and extrinsic contributions. The latter one arises due to any type of disorder in materials as a consequence of SOC-driven asymmetric scattering of electrons (skew- and side-jump scattering mechanism). It is accounted for via the vertex corrections and can be obtained from the difference $\sigma^{\mathrm{extr}} = \sigma_1^{\mathrm{VC}} - \sigma_1^{\mathrm{NVC}}$. It should be noted that it is determined by the electrons at the Fermi energy, whereas vertex corrections for the Fermi sea contribution to the AHC vanish exactly, as it was demonstrated by Turek et al. [55].

The impact of vertex corrections on the AHC for Fe_xPd_{1-x} can be seen in Fig. 4 showing calculated results in comparison with experiment [56]. The circles show theoretical results for the AHC accounting for vertex corrections while the triangles show the results calculated without them. The difference between these quantities can be attributed to the extrinsic contribution to the AHC.

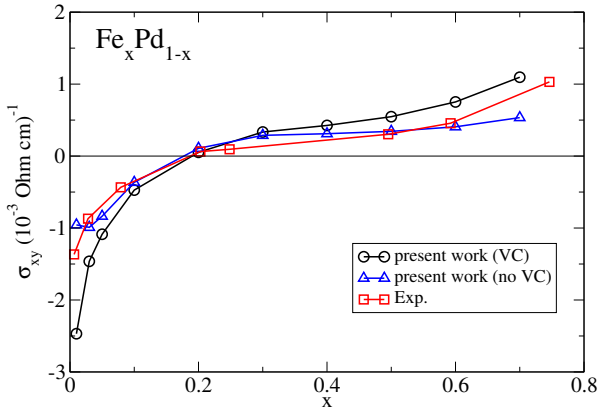

Figure 4. The AHC of Fe_xPd_{1-x} for $T = 0$ K. The circles show results including vertex corrections and the triangles show results without vertex corrections. The squares show experimental data from Ref. [56] for $T = 4.2$ K [54].

The KKR-CPA based implementation of the Kubo linear response formalism can be transferred with minor modifications to deal with other response quantities. An example for this is the Gilbert damping parameter α that can be expressed by a Kubo-Greenwood-like equation [57]

$$\alpha_{\mu\mu} = \frac{g}{\pi \mu_{tot}} \sum_n \mathrm{Tr} \left\langle \underline{T}^{\mu_0} \, \underline{\tilde{\tau}}^{0n} \, \underline{T}^{\mu_n} \, \underline{\tilde{\tau}}^{n0} \right\rangle_c \tag{21}$$

with the g-factor $2(1 + \mu_{orb}/\mu_{spin})$ in terms of the spin and orbital moments, μ_{spin} and μ_{orb}, respectively, the total magnetic moment $\mu_{tot} = \mu_{spin} + \mu_{orb}$, $\tilde{\tau}^{0n}_{\Lambda\Lambda'} = \frac{1}{2i}(\tau^{0n}_{\Lambda\Lambda'} - \tau^{0n}_{\Lambda'\Lambda})$ and with the energy argument E_F omitted. The matrix elements in Eq. (21) are identical to those occurring in the context of the exchange coupling [58]:

$$T^{\mu_n}_{\Lambda'\Lambda} = \int d^3r \; Z^{n\times}_{\Lambda'}(\vec{r}, E) \; [\beta \sigma_\mu B_{xc}(\vec{r})] \, Z^n_\Lambda(\vec{r}, E) \; , \tag{22}$$

where β is one of the standard Dirac matrices, σ_α is a 4×4-Pauli matrix [35] and $\vec{B}_{\mathrm{xc}}(r) = B_{\mathrm{xc}}(r)\hat{z}$ is the spin-dependent part of the exchange-correlation potential set up within local spin-density theory [58].

Similar to the electrical conductivity, the calculation of the Gilbert damping parameter for disordered systems requires to perform a configurational average. As an example, Fig. 5 represents the Gilbert damping parameter for the disordered alloy $Fe_{1-x}V_x$, as a function of the concentration, calculated neglecting vertex corrections, α^{NVC} (open symbols), and with vertex corrections taken into account, α^{VC} (full symbols) [59]. One can clearly see very pronounced changes of α^{VC} at low concentrations of V.

In particular, one finds a transition from conductivity-like to resistivity-like behavior of α^{VC} when varying x from 0 to 1, reflecting the dominance of intra- and inter-band transitions, respectively [60]. However, concentration-dependent changes of the Gilbert damping neglecting vertex corrections, α^{NVC}, are much more pronounced. In particular, it is found negative at small V concentrations, indicating non-physical results in this regime. In terms of the Boltzmann transport formalism, this is a consequence of the neglected scattering-in term [43] leading obviously to an incomplete description of the energy transfer processes. At high V concentration, neglecting the scattering-in term leads to an overestimation of the Gilbert damping, that may be discussed in analogy to the spin-pumping-out mechanism in the interpretation of the Gilbert damping by Tserkovnyak et al. [61].

3. Alloy-analogy model: theory

More or less all magnetic and response properties of materials depend on temperature. Accordingly, it is of great importance to account for the impact of a finite temperature within first-principles calculations in order to compare the results with experiment and to find out the mechanisms responsible for the temperature dependence of the considered properties. The finite temperature leads to a change in the occupation of electronic states as well as for the electronic structure due to different types of thermal excitations, as e.g. phonons and magnons. In general, experiments are performed in the temperature regime $k_{\mathrm{B}}T << E_{\mathrm{F}}$, leading to a weak re-population in the vicinity to the Fermi energy and usually does not have a pronounced impact on physical properties - at least for metallic systems. On the other hand, much more pronounced thermally induced changes are associated with thermally induced phonons and magnons. This holds in particular for the transport properties of metals. The calculation of the corresponding conductivity tensor $\sigma_{\mu\nu}$ for finite temperature requires to account for different types of thermal excitations, as mentioned before. As will be demonstrated below, they can be

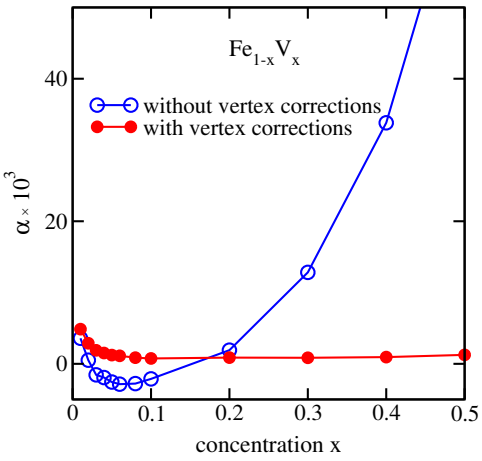

Figure 5. The Gilbert damping parameter for bcc $\mathrm{Fe}_{1-x}\mathrm{V}_x$ ($T = 0$ K) as a function of the V concentration x. Full (open) symbols give results obtained with (without) vertex corrections [59].

accounted for in a relatively simple way due to the fact that the dynamics of phonons and magnons is much slower compared to the electronic propagation. This allows to use the adiabatic approximation in the calculations of the electronic structure and related properties.

3.1. Treatment of thermal lattice displacement

A simple way to account for the impact of the thermal displacement of atoms from their equilibrium positions, i.e. for thermal lattice vibrations, on the electronic structure is to set up a representative displacement configuration for the atoms within an enlarged unit cell (super cell technique). In this case one has to use either a very large super cell or to take the average over a set of super cells. Alternatively, one may make use of the alloy analogy for the averaging problem. This allows in particular to restrict to the standard unit cell. Neglecting the correlation between the thermal displacements of neighboring atoms they can be treated using the mean-field approximation, giving access to the thermal average calculated by making use of the single-site CPA. This basic idea is illustrated by Fig. 6. To make use of this scheme a discrete set of N_v

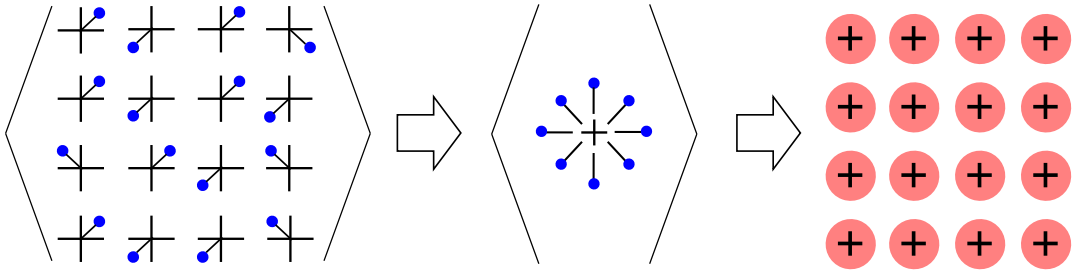

Figure 6. Configurational averaging for thermal lattice displacements: the continuous distribution $P(\Delta\vec{R}_n(T))$ for the atomic displacement vectors is replaced by a discrete set of vectors $\Delta\vec{R}_v(T)$ occurring with the probability x_v. The configurational average for this discrete set of displacements is made using the CPA leading to a periodic effective medium.

displacement vectors $\Delta\vec{R}_v^q(T)$ with probability x_v^q $(v = 1, .., N_v)$ is constructed for each basis atom q within the standard unit cell that is conform with the local symmetry and the temperature dependent root mean square displacement $(\langle u^2\rangle_T)^{1/2}$ according to:

$$\sum_{v=1}^{N_v} x_v^q |\Delta\vec{R}_v^q(T)|^2 = \langle u_q^2\rangle_T \ . \tag{23}$$

In general, the mean square displacement along the direction μ $(\mu = x, y, z)$ of the atom i can be either taken from experimental data or represented by an expression based on phonon calculations [62]

$$\langle u_{i,\mu}^2\rangle_T = \frac{3\hbar}{2M_i}\int_0^\infty d\omega g_{i,\mu}(\omega)\frac{1}{\omega}\coth\frac{\hbar\omega}{2k_{\rm B}T} \ , \tag{24}$$

where $\hbar$ is the reduced Planck constant, $k_{\rm B}$ is the Boltzmann constant and $g_{i,\mu}(\omega)$ is a projected phonon density of states [62]. On the other hand, a rather good estimate for the root mean square displacement can be obtained using Debye's theory. In this case, for systems with one atom per unit cell, Eq. (24) can be reduced to the expression:

$$\langle u^2 \rangle_T^{\rm D} = \frac{1}{4} \frac{3h^2}{\pi^2 M k_{\rm B} \Theta_D} \left[\frac{\Phi(\Theta_{\rm D}/T)}{\Theta_{\rm D}/T} + \frac{1}{4} \right] \tag{25}$$

with $\Phi(\Theta_{\rm D}/T)$ the Debye function and $\Theta_{\rm D}$ the Debye temperature [63]. Ignoring the zero temperature term 1/4 (see, e.g. Ref. [64]) and assuming a frozen potential for the atoms, the situation can be dealt with in full analogy to the treatment of disordered alloys on the basis of the CPA. Using a homogeneous distortion of displacement directions $\Delta \vec{R}_v^q$ in Eq. (23), the probability x_v for a specific displacement v may normally be chosen as $1/N_v$. The Debye temperature Θ_D used in Eq. (25) can be either taken from experimental data or calculated representing it in terms of the elastic constants [65]. In general the latter approach should give more reliable results in the case of multi-component systems.

To simplify notation we restrict in the following to systems with one atom per unit cell. The index q numbering sites in the unit cell can therefore be dropped, while the index n numbers the lattice sites.

Assuming a rigid displacement of the atomic potential in the spirit of the rigid muffin-tin approximation [66, 67] the corresponding single-site t-matrix $\underline{t}^{\rm loc} = \underline{t}^n$ with respect to the local frame of reference connected with the displaced atomic position is unchanged. With respect to the global frame of reference connected with the equilibrium atomic positions $\vec{R}_n$, however, the corresponding t-matrix $\underline{t}$ is given by the transformation:

$$\underline{t} = \underline{U}(\Delta \vec{R})\, \underline{t}^{\rm loc}\, \underline{U}(\Delta \vec{R})^{-1} \; . \tag{26}$$

The so-called U-transformation matrix $\underline{U}(\vec{s})$ is given in its non-relativistic form by [66, 67] :

$$U_{LL'}(\vec{s}) = 4\pi \sum_{L''} i^{l+l''-l'}\, C_{LL'L''}\, j_{l''}(|\vec{s}|k)\, Y_{L''}(\hat{s}) \; . \tag{27}$$

Here $L = (l, m)$ represents the non-relativistic angular momentum quantum numbers, $j_l(x)$ is a spherical Bessel function, $Y_L(\hat{r})$ a real spherical harmonics, $C_{LL'L''}$ a corresponding Gaunt number and $k = \sqrt{E}$ is the electronic wave vector. The relativistic version of the U-matrix is obtained by a standard Clebsch-Gordan transformation [35].

With Eq. (26), the various displacement vectors $\Delta \vec{R}_v(T)$ can be used to determine the scattering properties of a corresponding pseudo-component of a pseudo alloy. Each of the $N_{\rm v}$ pseudo-components with $|\Delta \vec{R}_{\rm v}(T)| = \langle u^2 \rangle_T^{1/2}$ is characterized by a corresponding U-matrix $\underline{U}_{\rm v}$ and accordingly with an individual t-matrix $\underline{t}_{\rm v}$. As for a substitutional alloy the site diagonal configurational average can be determined by solving the multi-component CPA equations with all quantities expressed w.r.t. the global frame of

reference:

$$\underline{\tau}_{\rm CPA} = \sum_{v=1}^{N_v} x_v \underline{\tau}_v \tag{28}$$

$$\underline{\tau}_v \quad = \left[(\underline{t}_v)^{-1} - (\underline{t}_{\rm CPA})^{-1} + (\underline{\tau}_{\rm CPA})^{-1}\right]^{-1} \tag{29}$$

$$\underline{\tau}_{\rm CPA} = \frac{1}{\Omega_{\rm BZ}} \int_{\Omega_{\rm BZ}} d^3k \left[(\underline{t}_{\rm CPA})^{-1} - \underline{G}(\vec{k}, E)\right]^{-1} \ , \tag{30}$$

where the underline indicates matrices with respect to the combined index Λ. As it was pointed out in the literature [59], the cutoff for the angular momentum expansion in these expressions should be taken $l \geq l_{\rm max}+1$ with $l_{\rm max}$ the value used in the calculations for the non-distorted lattice. In all calculations we have used $N_{\rm v} = 14$ with $\Delta\vec{R}_v$ pointing along $[\pm1, 0, 0]$, $[0, \pm1, 0]$, $[0, 0, \pm1]$ and $[\pm1, \pm1, \pm1]$. Increasing the set of directions for the atomic displacements led only to minor changes of the final results.

The first CPA equation (28) represents the requirement that embedding of a component v into the mean-field CPA medium should lead in the average to no additional scattering. Eq. (29) gives the scattering path operator for the embedding of the component v, while Eq. (30) gives the CPA scattering path operator in terms of a Brillouin zone integral with $\underline{G}(\vec{k}, E)$ the so-called KKR structure constants, and $\underline{t}_{CPA}$ the single-site t-matrix of the CPA medium to be determined iteratively.

Having solved the CPA equations any linear response quantity of interest may be calculated using Eq. (16) as for an ordinary substitutional alloy [68, 51]. This implies that one also has to deal with the so-called vertex corrections [68, 51] that take into account that one has to deal with a thermal configuration average of the type $\langle \hat{A}_\mu \, \Im G^+ \, \hat{A}_\nu \, \Im G^+ \rangle_{\rm c}$ that in general will differ from the simpler product $\langle \hat{A}_\mu \, \Im G^+ \rangle_{\rm c} \langle \hat{A}_\nu \, \Im G^+ \rangle_{\rm c}$.

3.2. Treatment of thermal spin fluctuations

As for the disorder connected with thermal displacements the impact of disorder due to thermal spin fluctuations may be accounted for by use of the super cell technique [69]. Alternatively one may again use the alloy analogy and determine the necessary configurational average by means of the CPA as indicated in Fig. 7. As for the thermal displacements in a first step a set of representative orientation vectors $\hat{e}_f$ (with $f = 1, ..., N_f$) for the local magnetic moment is introduced (see below). Using the rigid spin approximation the spin-dependent part $B_{\rm xc}$ of the exchange-correlation potential does not change for the local frame of reference fixed to the magnetic moment when the moment is oriented along an individual orientation vector $\hat{e}_f$. This implies that the single-site t-matrix $\underline{t}_f^{\rm loc}$ in the local frame is the same for all orientation vectors. With respect to the common global frame that is used to deal with the multiple scattering (see Eq. (30)) the t-matrix for a given orientation vector is determined by:

$$\underline{t} = \underline{R}(\hat{e}) \, \underline{t}^{\rm loc} \, \underline{R}(\hat{e})^{-1} \ . \tag{31}$$

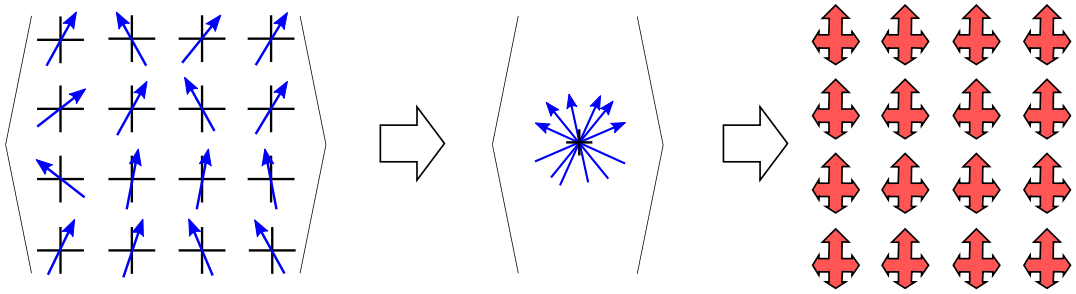

Figure 7. Configurational averaging for thermal spin fluctuations: the continuous distribution $P(\hat{e}_n)$ for the orientation of the magnetic moments is replaced by a discrete set of orientation vectors $\hat{e}_\mathrm{f}$ occurring with a probability x_f. The configurational average for this discrete set of orientations is made using the CPA leading to a periodic effective medium.

Here the transformation from the local to the global frame of reference is expressed by the rotation matrices $\underline{R}(\hat{e})$ that are determined by the vectors $\hat{e}$ or corresponding Euler angles [35].

Again the configurational average for the pseudo-alloy can be obtained by setting up and solving the CPA equations in analogy to Eqs. (28) to (30).

3.3. Models of spin disorder

The central problem with the scheme described above is obviously to construct a realistic and representative set of orientation vectors $\hat{e}_f$ and probabilities x_f for each temperature T to be used in the subsequent calculation of the response quantity using the alloy analogy model. A rather appealing approach is to calculate the exchange-coupling parameters J_{ij} of a system in an ab-initio way [70, 71, 58] and to use them in subsequent Monte Carlo (MC) simulations. Fig. 8 (left) shows results for the temperature dependent average reduced magnetic moment of corresponding simulations for bcc-Fe obtained for a periodic cell with 4096 atom sites. These results have been obtained using the exchange coupling parameters calculated for the disordered-local-moment (DLM) state, modeling the disordered magnetic state above T_C that gave the best agreement with the experimental Curie temperature [72]. The MC calculations for Fe using a classical Heisenberg Hamiltonian have been discussed in [73] in more detail. The full line in Fig. 8 (left) gives the value for the reduced magnetic moment of the MC cell $M_{\mathrm{MC}^*}(T) = \langle m_z \rangle_T / m_0$ projected on the z-axis, calculated for the last Monte Carlo step ($\hat{z}$ is the orientation of the total moment, i.e. $\langle \vec{m} \rangle_T \| \hat{z}$; the saturated magnetic moment at $T = 0$ K is $m_0 = |\langle \vec{m} \rangle_{T=0}|$). This scheme is called MC* in the following. In spite of the rather large number of sites (4096) the curve is rather noisy in particular when approaching the Curie temperature. Nevertheless, the spin configuration of the last MC step was used as an input for subsequent SPRKKR-CPA calculations using the orientation vectors $\hat{e}_f$ with the probability $x_f = 1/N_f$ with $N_f = 4096$. As Fig. 8 (left) shows, the temperature dependent reduced magnetic moment $M_{\mathrm{KKR(MC}^*)}(T)$

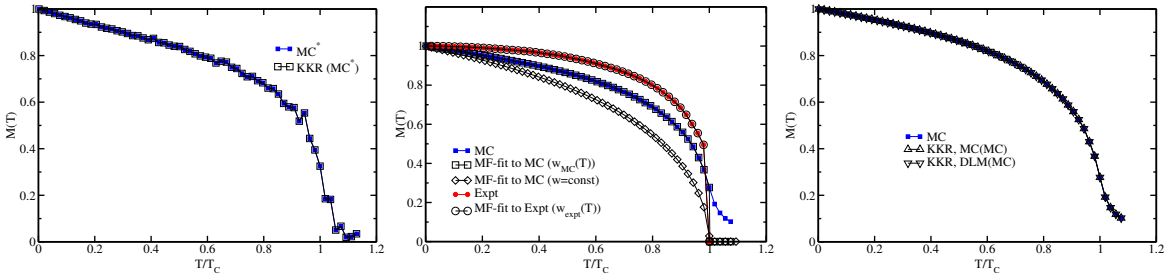

Figure 8. Averaged reduced magnetic moment $M(T) = \langle m_z \rangle_T / |\langle \vec{m} \rangle_{T=0}|$ of Fe along the z-axis as a function of the temperature T. Left: results of Monte Carlo simulations using scheme MC* (full squares) compared with results of subsequent KKR calculations (open squares). Middle: results of Monte Carlo simulations using scheme MC (full squares) compared with results using a mean-field fit with a constant Weiss field parameter $w_{\rm MC}(T_C)$ (open diamonds) and a temperature dependent Weiss field parameter $w_{\rm MC}(T)$ (open squares). In addition experimental data (full circles) together with a corresponding mean-field fit obtained for a temperature dependent Weiss field parameter $w_{\rm exp}(T)$. Right: results of Monte Carlo simulations using scheme MC (full squares) compared with results subsequent KKR calculations using the MC (triangles up) and a corresponding DLM (triangle down) spin configuration, respectively [44].

deduced from the electronic structure calculations follows one-to-one the Monte Carlo data $M_{\rm MC^*}(T)$. This is a very important result that demonstrates that the CPA although being a mean-field method and used here in its single-site formulation is nevertheless capable to reproduce the results of MC simulations that go well beyond the mean-field level.

Using the set of vectors $\hat{e}_f$ of the MC* scheme also for calculations of the Gilbert damping parameters α as a function of temperature, however, led to extremely noisy and unreliable curves for $\alpha(T)$. For that reason an average has been taken over many MC steps (scheme MC) leading to a much smoother curve for $M_{\rm MC}(T)$ as can be seen for the reduced magnetic moment in Fig. 8 (middle). As this enlarged set of vectors $\hat{e}_f$ got too large to be used directly in subsequent SPRKKR-CPA calculations, a scheme was worked out to get a set of vectors $\hat{e}_f$ and probabilities x_f that is not too large but nevertheless leads to smooth curves for $M(T)$.

The first attempt was to use the Curie temperature $T_{\rm C}^{\rm MC}$ to deduce a corresponding temperature independent Weiss field parameter $w(T_{\rm C})$ on the basis of the standard mean-field relation:

$$w(T_{\rm C}) = \frac{3k_{\rm B}T_C}{m_0^2} \ . \tag{32}$$

This leads to a reduced magnetic moment curve $M_{\rm MF}(T)$ that shows by construction the same Curie temperature as the MC simulations. For temperatures between $T = 0$ K and $T_{\rm C}$, however, the mean-field reduced magnetic moment $M_{\rm MF}(T)$ is well below the MC curve (see Fig. 8 (middle)). As an alternative to this simple approach we introduced a temperature dependent Weiss field parameter $w(T)$. This allows to describe the temperature dependent magnetic properties using input data obtained beyond the mean-

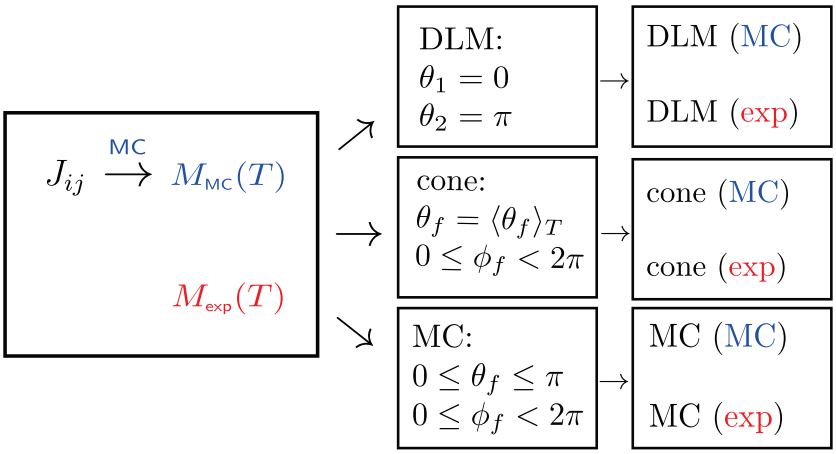

Figure 9. Overview of the different models to treat spin disorder together with the notation used in the main text. Starting point is a temperature dependent magnetization $M(T)$ either (i) taken from experiment ($M_{exp}(T)$) or (ii) obtained from a Monte Carlo simulation ($M_{MC}(T)$) that uses exchange-coupling constants from an first-principles electronic structure calculation. Three different models abbreviated as MC, DLM and cone are then used to obtain a representative distribution of moments (weights and directions $\{x_f, \hat{e}_f(\theta,\phi)\}$) that in turn reproduce $M(T)$. On the right in parenthesis the source is given ("MC" or "exp" data) upon which the calculation of response quantities is based [44].

field approximation. At the same time the statistical average can be determined treating the underlying model Hamiltonian in terms of the mean field theory. For this reason the reduced magnetic moment $M(T)$, being a solution of equation (see, e.g. Ref. [74])

$$M(T) = L\left(\frac{wm_0^2 M(T)}{k_{\text{B}}T}\right) , \tag{33}$$

was fitted to that obtained from MC simulations $M_{\text{MC}}(T)$ with the Weiss field parameter $w(T)$ as a fitting parameter, such that

$$\lim_{w \to w(T)} M(T) = M_{MC}(T) , \tag{34}$$

with $L(x)$ the Langevin function.

The corresponding temperature dependent probability $x(\hat{e})$ for an atomic magnetic moment to be oriented along $\hat{e}$ is proportional to $\exp(w(T)\hat{z}\cdot\hat{e}/k_{\text{B}}T)$ (see, e.g. Ref. [74]). To calculate this value we used N_θ and N_ϕ points for a regular grid for the spherical angles θ and ϕ, respectively, corresponding to the vector $\hat{e}_f$:

$$x_f = \frac{\sin(\theta_f)\exp[w(T)\hat{z}\cdot\hat{e}_f/k_{\text{B}}T]}{\sum_{f'}\sin(\theta_{f'})\exp[w(T)\hat{z}\cdot\hat{e}_{f'}/k_{\text{B}}T]} \tag{35}$$

Fig. 10 shows for three different temperatures the θ-dependent behavior of $x(\hat{e})$. As one notes, the MF-fit to the MC-results perfectly reproduces these data for all

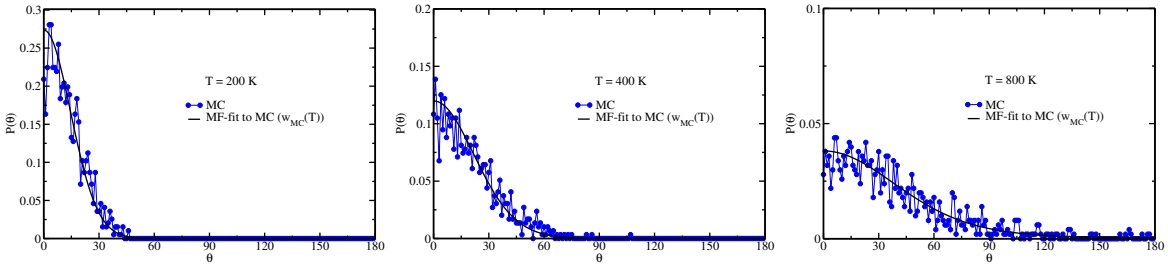

Figure 10. Angular distribution $P(\theta)$ of the atomic magnetic moment $\vec{m}$ obtained from Monte Carlo simulations (MC) for the temperature T = 200, 400, and 800 K compared with field mean-field (MF) data, x_f, (full line) obtained by fitting using a temperature dependent Weiss field parameter $w(T)$ (Eq. 33) [44].

temperatures. This applies of course not only for the angular resolved distribution of the magnetic moments shown in Fig. 10 but also for the average reduced magnetic moment recalculated using Eq. (33), shown in Fig. 8. Obviously, the MF-curve $M_{\mathrm{MF(MC)}}(T)$ obtained using the temperature dependent Weiss field parameter $w(T)$ perfectly reproduces the original $M_{\mathrm{MC}}(T)$ curve. The great advantage of this fitting procedure is that it allows to replace the MC data set with a large number N_f^{MC} of orientation vectors $\hat{e}_f$ (pointing in principle into any direction) with equal probability $x_f = 1/N_f^{\mathrm{MC}}$ (for illustration: $N_f^{MC} = 10^6$ MC steps have been used to calculate $M_{\mathrm{MC}}(T)$ for each T) by a much smaller data set with $N_f = N_\theta\, N_\phi$ (where $N_\theta = 180$ and $N_\phi = 18$ has been used in all calculations presented here) with x_f given by Eq. (35).

Accordingly, the reduced data set can straight forwardly be used for subsequent electronic structure calculations. Fig. 8 (right) shows that the calculated temperature dependent reduced magnetic moment $M_{\mathrm{KKR-MC(MC)}}(T)$ agrees perfectly with the reduced magnetic moment $M_{\mathrm{MC}}(T)$ given by the underlying MC simulations.

The DLM method has the appealing feature that it combines ab-initio calculations and thermodynamics in a coherent way. Using a non-relativistic formulation, it was shown that the corresponding averaging over all orientations of the individual atomic reduced magnetic moments can be mapped onto a binary pseudo-alloy with one pseudo-component having up- and downward orientation of the spin moment with concentrations $x_\uparrow$ and $x_\downarrow$, respectively [75, 76]. For a fully relativistic formulation, with spin-orbit coupling included, this simplification cannot be justified anymore and a proper average has to be taken over all orientations [77]. As we do not perform DLM calculations but use here only the DLM picture to represent MC data, this complication is ignored in the following. Having the set of orientation vectors $\hat{e}_f$ determined by MC simulations the corresponding concentrations $x_\uparrow$ and $x_\downarrow$ can straight forwardly be fixed for each temperature by the requirement:

$$\frac{1}{N_f}\sum_{f=1}^{N_f}\hat{e}_f = x_\uparrow\hat{z} + x_\downarrow(-\hat{z})\ , \tag{36}$$

with $x_\uparrow + x_\downarrow = 1$. Using this simple scheme electronic structure calculations have been

performed for a binary alloy having collinear magnetization. The resulting reduced magnetic moment $M_{\mathrm{KKR-DLM(MC)}}(T)$ is shown in Fig. 8 (right). As one notes, again the original MC results are perfectly reproduced. This implies that when calculating the projected reduced magnetic moment M_{z} that is determined by the averaged Green function $\langle G \rangle$ the transversal magnetization has hardly any impact.

Fig. 8 (middle) gives also experimental data for $M(T)$ [78]. While the experimental Curie-temperature $T_{\mathrm{C}}^{\mathrm{exp}} = 1044$ K [78] is rather well reproduced by the MC simulations $T_{\mathrm{C}}^{\mathrm{MC}} = 1082$ K one notes that the MC-curve $M_{\mathrm{MC}}(T)$ is well below the experimental curve. In particular, $M_{\mathrm{MC}}(T)$ drops too fast with increasing T in the low temperature regime and does not show the $T^{3/2}$-behavior. The reason for this is that the MC simulations do not properly account for the low-energy long-ranged spin wave excitations responsible for the low-temperature magnetization variation. Performing ab-initio calculations for the spin wave energies and using these data for the calculation of $M(T)$ much better agreement with experiment can indeed be obtained in the low-temperature regime than with MC simulations [2].

As the fitting scheme sketched above needs only the temperature reduced magnetic moment $M(T)$ as input it can be applied not only to MC data but also to experimental data. Fig. 8 shows that the mean field fit $M_{\mathrm{MF(exp)}}(T)$ again perfectly fits the experimental reduced magnetic moment curve $M_{\mathrm{exp}}(T)$. Based on this good agreement this corresponding data set $\{\hat{e}_f, x_f\}$ has also been used for the calculation of response tensors (see below).

An additional much simpler scheme to simulate the experimental $M_{\mathrm{exp}}(T)$ curve is to assume the individual atomic moments to be distributed on a cone, i.e. with $N_\theta = 1$ and $N_\phi >> 1$ [79]. In this case the opening angle $\theta(T)$ of the cone is chosen such to reproduce $M(T)$. In contrast to the standard DLM picture, this simple scheme allows already to account for transversal components of the magnetization. Corresponding results for response tensor calculations will be shown below.

Finally, it should be stressed here that the various spin configuration models discussed above assume a rigid spin moment, i.e. its magnitude does not change with temperature nor with orientation. In contrast to this Ruban et al. [80] use a longitudinal spin fluctuation Hamiltonian with the corresponding parameters derived from ab-initio calculations. As a consequence, subsequent Monte Carlo simulations based on this Hamiltonian account in particular for longitudinal fluctuations of the spin moments. A similar approach has been used by Drchal et al. [81, 82] leading to good agreement with the results of Ruban et al. However, the scheme used in these calculations does not supply in a straightforward manner the necessary input for temperature dependent transport calculations. This is different from the work of Staunton et al. [83] who performed self-consistent relativistic DLM calculations without the restriction to a collinear spin configuration. This approach in particular accounts in a self-consistent way for longitudinal spin fluctuations.

3.4. Combined chemical and thermally induced disorder

The various types of disorder discussed above may be combined with each other as well as with chemical i.e. substitutional disorder. In the most general case a pseudo-component (vft) is characterized by its chemical atomic type t, the spin fluctuation f and lattice displacement v. Using the rigid muffin-tin and rigid spin approximations, the single-site t-matrix $t_t^{\rm loc}$ in the local frame is independent from the orientation vector $\hat{e}_f$ and displacement vector $\Delta\vec{R}_v$, and coincides with $\underline{t}_t$ for the atomic type t. With respect to the common global frame one has accordingly the t-matrix:

$$\underline{t}_{vft} = \underline{U}(\Delta\vec{R}_v)\,\underline{R}(\hat{e}_f)\,\underline{t}_t\,\underline{R}(\hat{e}_f)^{-1}\underline{U}(\Delta\vec{R}_v)^{-1}\ . \tag{37}$$

With this the corresponding CPA equations are identical to Eqs. (28) to (30) with the index v replaced by the combined index (vft). The corresponding pseudo-concentration $x_{\rm vft}$ combines the concentration $x_{\rm t}$ of the atomic type t with the probability for the orientation vector $\hat{e}_{\rm f}$ and displacement vector $\Delta\vec{R}_{\rm v}$. In summary, the AAM approach can be applied to calculate various temperature dependent properties both for ordered and for disordered alloy systems. Below we present several examples, discussing the role of different types of thermally induced excitations in non-magnetic and magnetic materials.

4. Applications: Equilibrium electronic structure at finite temperature

First, we will discuss the impact of thermal lattice vibrations and spin fluctuations on the ground state electronic structure of a solid, focusing on the temperature induced modification of the density of states (DOS). Thermally induced lattice vibrations and spin fluctuations lead to disorder that should have an impact on the electronic structure in a similar way as chemical disorder in alloy systems. Using the alloy analogy model described above, the corresponding Green function in multiple scattering representation is given in terms of a configurational average of the scattering path operator $\underline{\tau}_{\rm CPA}$ (see Eqs. (28)-(30)). This gives direct access to the temperature-dependent DOS $n(E)$ by modifying the expression in Eq. (4), accordingly:

$$n(E) = -\frac{1}{\pi}\Im\,{\rm Tr}\int \left\langle G^{+}(\vec{r},\vec{r},E)\right\rangle_c\, d^3r\ . \tag{38}$$

Obviously, the same holds for the Bloch spectral function $A^{\rm B}(\vec{k},E)$ given in Eq. (12) that can be seen as a $\vec{k}$-resolved DOS function. As an example for a rather strong temperature-induced modification of the electronic structure caused by thermal lattice vibrations, Fig. 11 shows the Bloch spectral function $A^{\rm B}_\sigma(\vec{k},E)$ of Ag calculated for $T = 100$ (left) and $T = 600\,{\rm K}$ (right). The strong smearing of the electronic energy bands for $T = 600\,{\rm K}$ indicates a decrease of the life time of the electron states, which is reflected by the width of the $A^{\rm B}_\sigma(\vec{k},E,T)$ functions changing as a function of temperature.

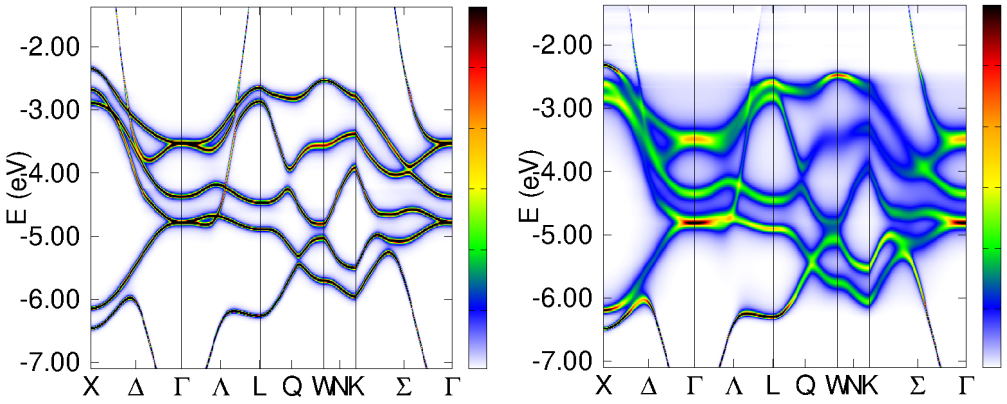

Figure 11. The BSF for Ag at $T = 100$ (left) and $T = 600$ (right) K, respectively [84].

In the second example, we consider the impact of thermal lattice vibrations and spin fluctuations on the electronic structure of the ferromagnet bcc Fe (see Ref. [85]). For this, we show in Fig. 12 the spin projected DOS calculated for several temperatures, represented w.r.t. two different frames of reference: the local one with the $\hat{z}$ axis seen as a quantization axis, and the global one fixed to the crystal lattice. One can see in Fig. 12(b) that spin fluctuations dominate the temperature induced modification of the electronic structure, especially for temperatures approaching T_{C} (see Fig. 13). Therefore, we will focus mainly on the impact of thermal spin fluctuations on the electronic structure in the following. The scattering path operator averaged over spin fluctuations at a given temperature can be written as follows $\underline{\tau}_{\mathrm{CPA}} = \sum_{\mathrm{f}} x_f \underline{\tau}_{\mathrm{f}}$, where $\underline{\tau}_{\mathrm{f}}$ is associated with the spin fluctuation with direction $\hat{e}_{\mathrm{f}}$, giving access to a corresponding contribution $n_{\mathrm{f},\sigma}(E)$ to the DOS. The spin-projected DOS $n^{loc}_{\mathrm{f},\sigma}(E)$ evaluated in the

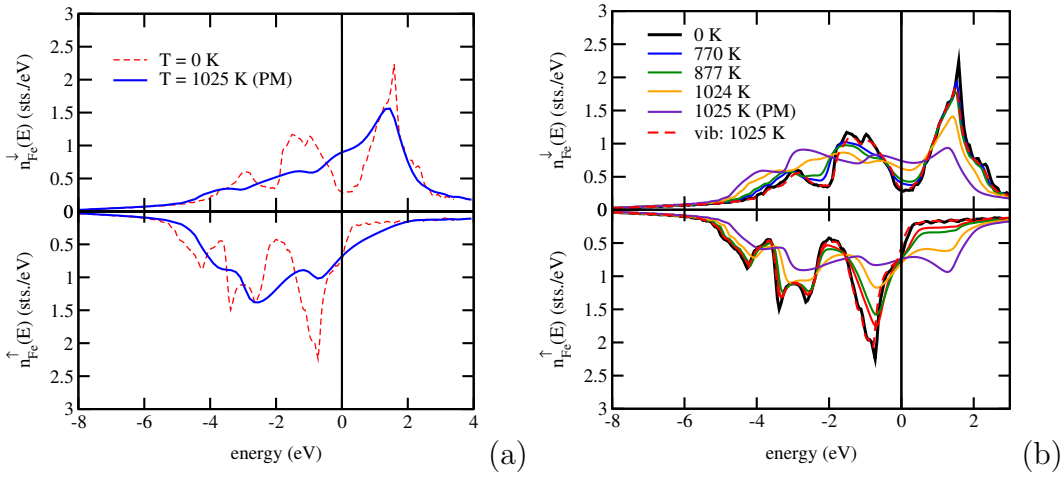

Figure 12. Total spin projected DOS for bcc Fe in the local (a) and global (b) frames of reference [85].

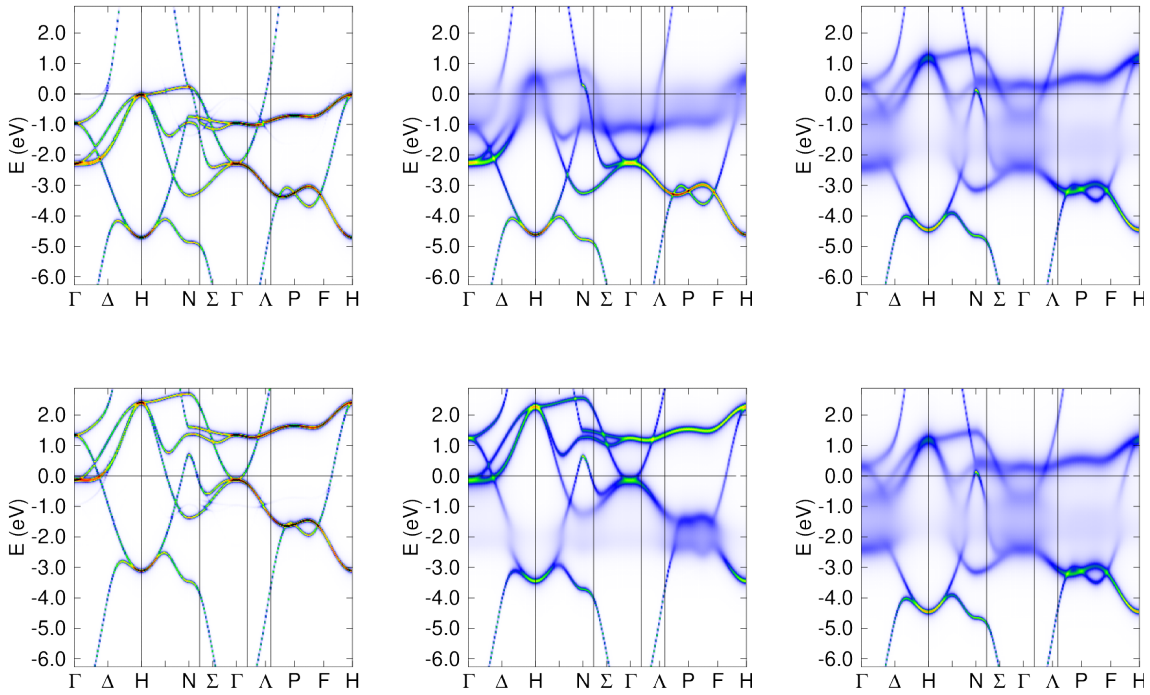

Figure 13. The spin projected BSF $A^{\mathrm{B}}_{\sigma}(\vec{k}, E)$ (global frame of reference) for bcc Fe at $T = 0$ K (left), $T = 800$ K (middle) and $T = T_{\mathrm{C}}$ (right). The top and bottom panel show the majority- and the minority-spin states, respectively.

local frame of reference with $\hat{z}_{\mathrm{f}} || \hat{e}_{\mathrm{f}}$ is different for different spin channels in the case of a non-zero local magnetic moment even in the paramagnetic (PM) (i.e. magnetically disordered) state with $\langle \hat{m} \rangle = 0$. In this frame of reference the electronic states are well characterized by the spin quantum number, in case of a weak spin-orbit interaction (SOI) in the material. However, the average spin-projected DOS curves calculated in the fixed global frame of reference for the PM state are equal for the two spin channels, i.e. $\langle n_{+} \rangle(E) = \langle n_{-} \rangle(E)$. The indices $'+'$ and $'-'$ imply here a spin orientation along the global $\hat{z}$ direction and opposite to it, respectively. Due to the random orientation of the atomic spin magnetic moments in the system, the $\langle n_{+} \rangle(E)$ and $\langle n_{-} \rangle(E)$ DOS curves have contributions from the electronic states characterized by different quantum numbers, implying a mixed-spin character of the electronic states (see also the spin projected BSF $A^{\mathrm{B}}_{\sigma}(\vec{k}, E)$ in Fig. 13). Fig. 12 (a) represents the DOS for bcc Fe calculated for the PM state ($\langle \hat{m} \rangle = 0$) in the local frame of reference (solid line), averaged over all possible orientations of the magnetic moment. This result is compared with the DOS for $T = 0$ K. One can see, first of all, a finite exchange splitting of the majority and minority spin states at $T > T_{\mathrm{C}}$. The main temperature effect is a significant broadening of the energy bands when compared to $T = 0$ K. However, in the global frame of reference the difference between the majority and minority-spin states decreases approaching the critical temperature $T_{\mathrm{C}} = 1024$ K and above. Above T_{C}, in the PM state, the difference

between the spin-projected DOS curves disappeared. The same can also be seen for the spin projected BSF shown in Fig. 13. However, the situation is different when only thermal lattice vibrations are taken into account (dashed line in Fig. 12 (b) for $T = 1025$ K). In this case only a weak broadening of the energy bands occurs, which is much weaker when compared to that due to spin fluctuations.

5. Applications:Temperature dependent exchange coupling parameters

5.1. Theoretical background

The phenomenological Heisenberg Hamiltonian

$$H_{ex} = -\sum_{ij} J_{ij}(\hat{e}_i \cdot \hat{e}_j) - \sum_{ij} \vec{D}_{ij}[\hat{e}_i \times \hat{e}_j] \; . \tag{39}$$

is a well established basis for the investigation of finite-temperature and dynamical magnetic properties of materials. Compared to its standard form, the Hamiltonian in Eq. (39) is extended to account relativistic effects, and includes apart from the isotropic exchange coupling parameters J_{ij} the Dzyaloshinskii-Moriya (DM) interaction parameters $\vec{D}_{ij}$, connected with the spin moments on sites i and j, pointing along the directions $\hat{e}_i$ and $\hat{e}_j$, respectively. Very often these parameters are derived from experimental data. Alternatively, they can be calculated on an ab-initio level. Adopting for example the multiple scattering formalism and restricting to $T = 0$ K, the full exchange coupling tensor can be obtained from the expression [71, 58]:

$$J_{ij}^{\alpha_i\alpha_j} = -\frac{1}{2\pi}\Im \int dE \; \mathrm{Tr} \; \Delta\underline{V}^{\alpha_i}(E)\underline{\tau}^{ij}(E)\Delta\underline{V}^{\alpha_j}(E)\underline{\tau}^{ji}(E) \; . \tag{40}$$

The DMI parameters are given by the antisymmetric part of the exchange coupling tensor $J_{ij}^{\alpha_i\alpha_j}$, while the isotropic exchange parameters J_{ij} are given by the average over its diagonal elements [71]. In Eq. (40) $\underline{\tau}^{ij}$ is the scattering path operator connecting sites i and j with the underline indicating matrices in the $\Lambda = (\kappa, \mu)$-representation [35]. The corresponding on-site coupling for site i is represented by the matrix $\Delta V_{\Lambda\Lambda'}^{\alpha_i} = T_{\Lambda'\Lambda}^{\alpha_i}$ [58], with $T_{\Lambda'\Lambda}^{\alpha_i}$ given by Eq. (22). For simplicity, below we consider only systems with one atom per unit cell.

Considering finite temperature magnetic properties one has to account first of all for the impact of thermally induced lattice vibrations and spin fluctuations on the electronic structure. Its temperature dependent modification will have a corresponding impact on the properties depending on it. As an example, we consider the temperature dependence of the exchange parameters, that can be calculated making use of the AAM approach. Focusing on the impact of thermal lattice vibrations and assuming a frozen potential for the displaced atoms and neglecting correlations between the atomic displacements, Eqs. (28) to (30) allow to perform the necessary thermal configurational averaging when dealing with Eq. (40) for finite temperatures. This way one gets for the temperature dependent exchange coupling tensor:

$$\bar{J}_{ij}^{\alpha_i\alpha_j} = -\frac{1}{2\pi}\Im \int dE \; \mathrm{Tr}\langle\Delta\underline{V}^{\alpha_i}\underline{\tau}^{ij}\Delta\underline{V}^{\alpha_j}\underline{\tau}^{ji}\rangle_{\mathrm{c}} \; , \tag{41}$$

where $\langle ... \rangle_c$ represents the configurational average with respect to the set of displacements. Note that here the temperature dependent change of the electron occupation function is not taken into account, as this is normally relevant for very high temperatures (see Ref. [1]). Furthermore, as the expression in Eq. (41) refers explicitly to a specific pair of sites, the vertex corrections have been ignored here; i.e. the configuration average has been simplified to $\langle \Delta \underline{V}^{\alpha} \ \underline{\tau}^{ij} \rangle_c \langle \Delta \underline{V}^{\beta} \ \underline{\tau}^{ji} \rangle_c$.

5.1.1. bcc Fe As an example, we represent here corresponding results for the temperature dependent exchange coupling parameters of bcc Fe, determined by thermal lattice vibrations. The isotropic exchange coupling parameters J_{ij} calculated for the FM reference state of Fe are plotted in Fig. 14 (a) for different amplitudes of thermal lattice vibrations related to a corresponding *lattice temperature* $T_{\rm lat}$ according to the Debye model. As one can see, there are indeed pronounced modifications of the exchange

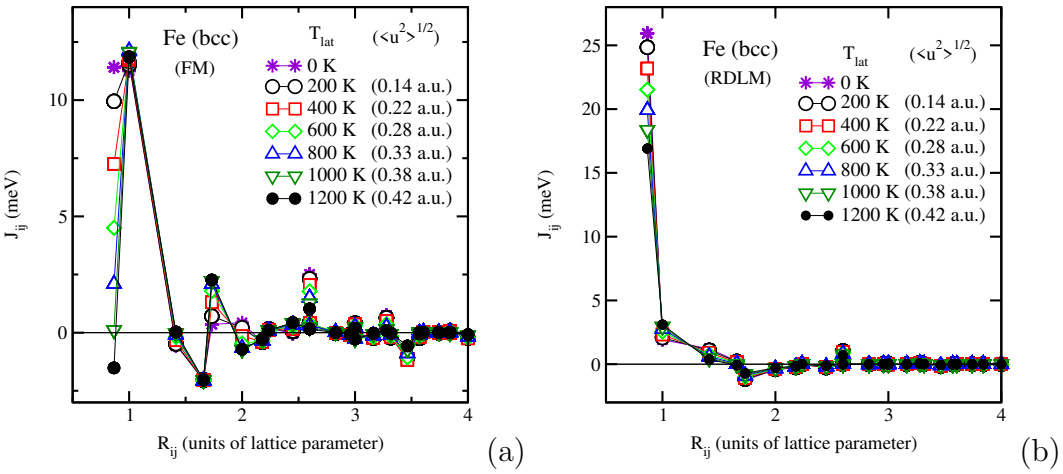

Figure 14. The isotropic exchange coupling parameters J_{ij} for bcc Fe calculated for the FM (a) and DLM (b) reference states. The results are represented for different amplitudes of the thermal lattice vibrations given in terms of the rms displacement $(\langle u^2 \rangle_T)^{1/2}$ that can be related to a specific *lattice temperature* $T_{\rm lat}$, for example via the Debye model.

coupling parameters due to the lattice vibrations that depend strongly on the considered pair of sites. By far the most significant changes are found for the nearest-neighbor interaction parameters that decrease strongly with an increase of the amplitude of the thermal displacements or the *lattice temperature*, respectively. This in turn should have a corresponding impact on the Curie temperature $T_{\rm C}$. Within the mean-field approximation (MFA), $T_{\rm C}$ is essentially given by the sum $\sum_j J_{ij}$ over the coupling parameters allowing therefore in a simple way to monitor the dependence of $T_{\rm C}$ on the effective *lattice temperature* $T_{\rm lat}$ or, equivalently, on the temperature dependent rms displacement $(\langle u^2 \rangle_T)^{1/2}$. Fig. 15 (circles) shows corresponding results for $T_{\rm C}$ as a function of $(\langle u^2 \rangle_T)^{1/2}$ obtained by summing J_{ij} within a sphere with radius $R_{\rm max} = 5a$, with a being the lattice parameter.

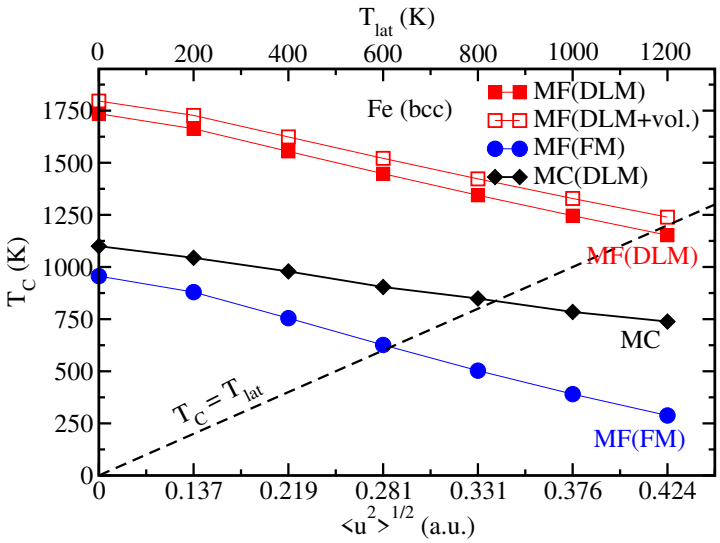

Figure 15. Theoretical Curie temperature T_{C} for bcc Fe plotted as a function of the amplitudes of thermal lattice vibrations $(\langle u^2 \rangle_T)^{1/2}$ calculated for the FM (circles) and DLM reference states either using the MFA (squares) or MC simulations (diamonds) together with the relation between the *lattice temperature* T_{lat} and $(\langle u^2 \rangle_T)^{1/2}$. Open squares represent the results on DLM-based mean-field T_{C} calculated for lattice parameter corresponding to experimental Curie temperature.

Keeping in mind that the mean field approximation (MFA) normally overestimates the critical temperature when compared to results obtained from Monte Carlo (MC) simulations or RPA (random phase approximation) based calculations, one notes that the MFA result for T_{C} of bcc Fe, evaluated without accounting for the lattice vibrations, is rather close to the experimental value, $T_{\mathrm{C}}^{\mathrm{exp}} = 1043$ K. However, a finite amplitude of the lattice vibrations leads to a significant monotonous decrease of $T_{\mathrm{C}}^{\mathrm{MF}}$ with $(\langle u^2 \rangle_T)^{1/2}$ implying a corresponding deviation from experiment.

As mentioned above, more reliable results for the Curie temperature can be obtained on the basis of the exchange coupling parameters calculated for the PM reference state described here within the disordered local moment (DLM) approximation. The significant difference of the electronic structure for the magnetically disordered state compared to that for the FM state (see Fig. 12) leads to a corresponding difference for the exchange coupling parameters. Figure 14 (b) gives the resulting exchange coupling parameters for the DLM reference state of Fe. The MFA Curie temperature (≈ 1700 K) exceeds the value obtained for the FM reference state in an appreciable way when thermal lattice vibrations are ignored. This observation was already reported in the literature before (see, e.g. [86]). However, a finite amplitude of the thermal atomic displacements leads again to a lower MFA-based Curie temperature, as it is shown in Fig. 15 (squares), reaching the value $T_{\mathrm{C}}^{\mathrm{MF}} \approx 1200$ K when requiring that the Curie temperature and *lattice temperature* coincide. In order to compare the impact of thermal lattice vibrations on the exchange interactions with the impact of a thermal lattice expansion, the DLM-based calculations have been performed also for bcc Fe with the

lattice parameter $a = 5.48$ a.u. as determined for the Curie temperature [87]. The mean-field results for T_C obtained in this case show only a rather small increase when compared to the case without account of the lattice expansion (open squares in Fig. 15). This implies a dominating influence on J_{ij} for thermal lattice vibrations when compared to the impact of the thermal lattice expansion.

Fig. 15 gives also results for the Curie temperature obtained by MC simulations considering 15 atomic shells around each atom using DLM-based exchange parameters (diamonds). In this case, the Curie temperature $T_{\rm C}^{\rm MC}$, calculated for an unperturbed lattice slightly overestimates the experimental value. When the amplitude of thermal lattice vibrations increases, $T_{\rm C}^{\rm MC}$ also goes down and coincides with the *lattice temperature* $T_{\rm lat}$ at around 1000 K underestimating slightly the experimental Curie temperature this way. This small deviation might among others be ascribed to the approximate treatment of lattice vibrations when calculating J_{ij} that in particular neglects correlations in the thermal motion of the atoms.

To get more insight concerning the impact of lattice vibrations on the temperature dependence of the exchange coupling parameters, one can represent them in terms of the spin-lattice coupling (SLC) parameters $\mathcal{J}_{ij,k}^{{\rm diag},\mu}$ and $\mathcal{J}_{ij,kl}^{{\rm diag},\mu\nu}$ characterizing the corrections of $J_{ij}^{\rm diag}$ caused by atomic displacements u_k^μ. The temperature dependent parameters $\langle J_{ij}\rangle_T$ may be estimated by averaging over all lattice excitations corresponding to a given temperature T. This can be expressed as follows

$$\langle J_{ij}\rangle_T = J_{ij}^0 + \sum_{k,\mu} \mathcal{J}_{ij,k}^{{\rm diag},\mu} \langle u_k^\mu\rangle_T + \sum_{kl,\mu\nu} \mathcal{J}_{ij,kl}^{{\rm diag},\mu\nu} \langle u_k^\mu u_l^\nu\rangle_T + \dots \,. \tag{42}$$

As the average $\langle u_k^\mu\rangle_T$ of the linear term vanishes, the second-order SLC parameters give rise to the lowest-order contribution to the temperature dependence of the exchange parameters, leading to [88]

$$\langle J_{ij}\rangle_T = J_{ij}^0 + \langle u^2\rangle_T^{\rm D} \sum_\mu \left[\mathcal{J}_{ij,ij}^{{\rm diag},\mu\mu} + \mathcal{J}_{ij,ii}^{{\rm diag},\mu\mu} + \mathcal{J}_{ij,jj}^{{\rm diag},\mu\mu}\right] . \tag{43}$$

Note that $\langle u^2\rangle_T^{\rm D}$ stands for the mean square displacement corresponding to a certain temperature T is estimated via the Debye model used also when applying the AAM to calculate the thermal average of the exchange parameters. The values for $\langle J_{ij}\rangle_T$ obtained this way for bcc Fe are compared in Fig. 16 with corresponding results calculated on the basis of the alloy analogy model [89]. One can see that in this particular case the contribution due to displacements of the interacting atoms are dominating, while in general one might have to account also for contributions due to the displacements of all surrounding atoms l and k different from i and j.

6. Applications: Transport properties of metals at finite temperature

As we will show in this section, the AAM approach is a very useful tool to investigate finite temperature behavior of various types of linear response functions. First we will discuss transport properties, calculated using using Kubo's linear response formalism by

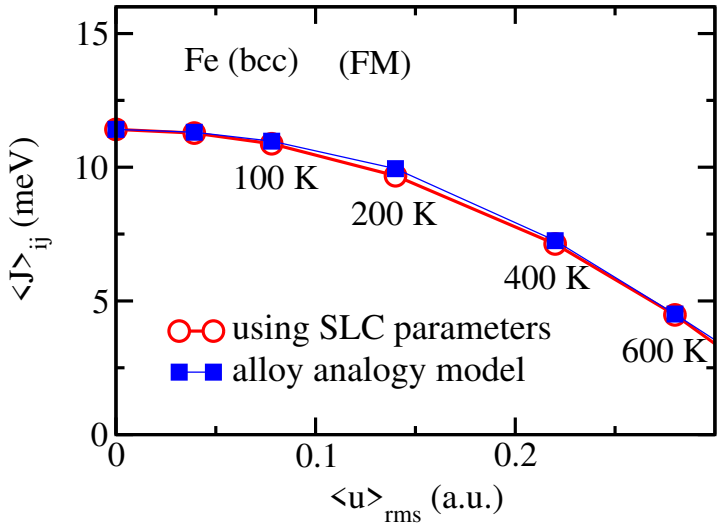

Figure 16. The dependence of the nearest-neighbor exchange coupling parameters $\langle J_{ij}\rangle_T$ of bcc Fe on the root-mean-square thermal displacement $\sqrt{\langle u^2\rangle_T^{\mathrm{D}}}$ of the atoms. Corresponding temperatures are attached to some data points. Open symbols represent the results based on the SLC parameters using Eq. (43) while full squares correspond to results obtained via the alloy-analogy model [89].

means of Eq. (17). We will consider separately non-magnetic and magnetic systems. In the first case only thermal lattice vibrations give rise to temperature dependent changes of the transport properties, e.g. the electrical resistivity, while in the latter case both thermal lattice vibrations as well as spin fluctuations contribute to the temperature dependence of their transport properties.

6.1. Temperature dependent conductivity of non-magnetic systems

6.1.1. Electrical conductivity of fcc Cu To give an impression on the impact of thermally induced atomic displacements alone on the electrical resistivity, Fig. 17 shows the temperature dependent resistivity $\rho(T)$ for pure Cu ($\Theta_{\mathrm{Debye}} = 315$ K), that is found in very good agreement with corresponding experimental data [90]. This implies that the alloy analogy model that ignores any inelastic scattering events should in general lead to rather reliable results for the resistivity induced by thermal displacements. Accordingly, comparison with experiment should allow for magnetically ordered systems to find out the most appropriate model for spin fluctuations.

The finite temperature [84] SHE and OHE have been investigated for elemental non-magnetic 3*d*, 4*d* and 5*d* transition metals [84]. Again, this implies the impact of only thermal lattice vibrations characterized by the lattice temperature T_{lat}, therefore we will use everywhere in this section the term 'temperature' instead of 'lattice temperature'. Fig. 18 shows the total (full circles) and extrinsic (open circles) OHC for some selected transition metals, plotted as a function of temperature. Similar plots are shown also for the total (full squares) and extrinsic (open squares) SHC.

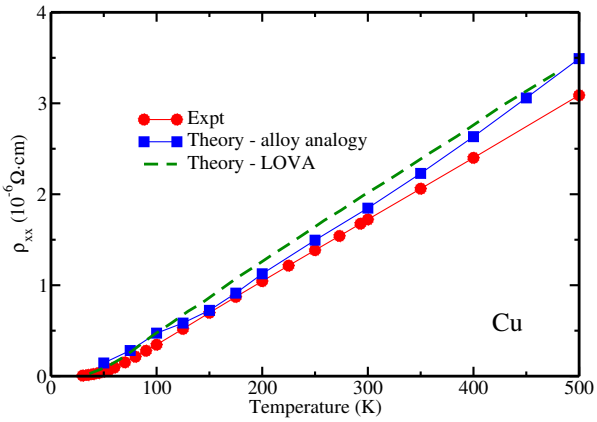

Figure 17. Temperature dependent longitudinal resistivity of fcc-Cu $\rho(T)$ obtained by accounting for thermal vibrations as described in section 3.1 compared with corresponding experimental data [90]. In addition results are shown based on the LOVA (lowest order variational approximation) to the Boltzmann formalism [18].

For all systems the intrinsic OHC and SHC are dominating in the low-temperature limit, as the extrinsic contributions have to vanish for T approaching 0 K. For the temperature window shown in Fig. 18, on the other hand, the extrinsic contributions are almost unchanged. As it is concluded in Ref. [84] concerning the properties of the OHC and SHC originating from thermal lattice vibrations: the contribution due to skew scattering to the extrinsic OHC and SHC in pure metals is rather small, and the extrinsic OHC and SHC are dominated by the side-jump scattering mechanism, which is in line with theoretical predictions for the anomalous Hall effect, reported by Crépieux and Bruno [91].

The results presented in Fig. 18 show substantial temperature-dependent changes of the intrinsic OHC in pure transition metals, associated with corresponding changes of the Fermi sea contribution. This can be attributed to the changes of the electronic structure caused by thermal lattice vibrations leading first of all to a smearing of the energy bands implying a decreasing lifetime for the electronic states. In contrast to the OHC, a weak temperature-induced change can be seen for both the intrinsic and extrinsic contributions to the SHC. To gain insight into to origin for this different behavior we have performed calculations for the OHC and SHC as a function of the occupation of the electron states, using Ag as a representative system as its OHC varies quite strongly with temperature. In the calculations, the occupation is controlled by the upper energy limit $E_{\rm occ}$ which is equal to E_F under normal condition. The calculations have been done for two lattice temperatures, $T = 100$ and 600 K. Fig. 19 shows the results for the total OHC and SHC, which, however, are mainly determined by the intrinsic contributions, as it is shown in Fig. 18. One can see in Fig. 19 (bottom) a minor difference between the results for the SHC obtained for two different temperatures, that, however, is not the case for the OHC (Fig. 19 top). The difference between the results for the OHC at $T = 100$ and 600 K increases with increasing occupation, i.e. $E_{\rm occ}$, of the d-states, and almost does

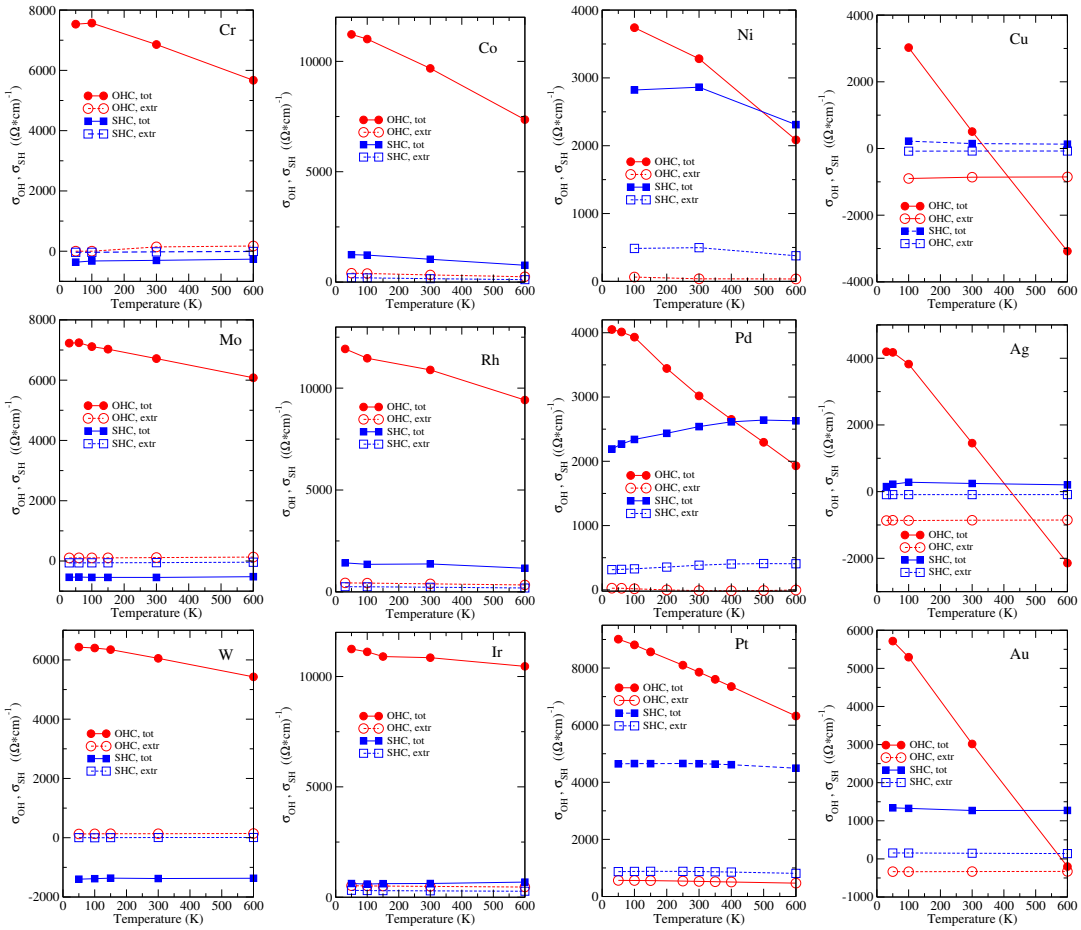

Figure 18. OH and SH conductivities (full red circles and full blue squares, respectively) for selected elemental $3d$, $4d$ and $5d$ non-magnetic metals, calculated accounting for thermal lattice vibrations and plotted as a function of temperature. Empty symbols represent the extrinsic contributions to the OHC and SHC [84].

not change when E_{occ} goes beyond the top of the d-band. This occupation dependence, in particular, may be responsible for a weaker temperature dependence of the OHC for the early transition metals. The strong temperature-induced modification of the OHC can be attributed to the impact of thermal lattice vibrations on the electronic structure leading to a strong smearing of the energy bands, increasing with temperature. This can be seen in Fig. 11 that gives the Bloch spectral function $A^{\mathrm{B}}(\vec{k}, E, T)$ for Ag, calculated for $T = 100$ (left) and 600 K (right). Furthermore, it is crucial that the temperature-induced lattice distortion breaks the local symmetry at each lattice site. When the origin of the OHE is associated with the $\vec{k}$-dependent orbital texture controlled by symmetry [92, 93, 94, 95, 96], the OHC variation at finite temperature may stem from broken local symmetry at every atomic position, leading to a modification of the orbital texture, increasing with temperature (see also discussions in Ref. [95]). Interestingly, only minor changes occur for the SHC, in conflict with the idea that the SOC-driven spin Hall current density originates from the orbital Hall current density [92]. This indicates in

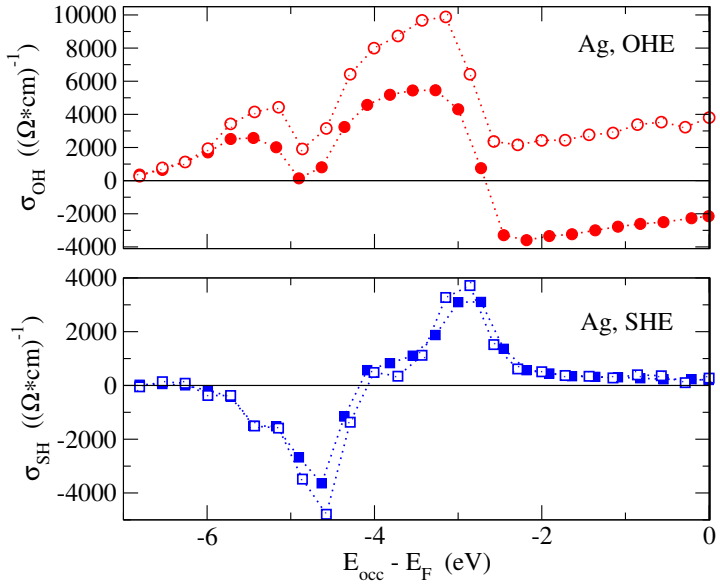

Figure 19. The OHC, $\sigma_{\rm OH}(E_{\rm occ})$ (top) and SHC, $\sigma_{\rm SH}(E_{\rm occ})$ (bottom) calculated for Ag at $T = 100$ (open symbols) and $T = 600$ K (full symbols), represented as a function of occupation of electron states $E_{\rm occ}$ [84].

particular a rather weak impact of the temperature-induced lattice distortions on the SOC-driven spin texture within the Brillouin zone, in contrast to the SOC-independent orbital texture.

6.1.2. Temperature effect in doped systems In the case of doped materials, the impact of temperature induced lattice vibrations on the OHE and SHE is quite different when compared to pure metals. Fig. 20 demonstrates this for the OHC (circles) and SHC (squares) for $Ir_{0.99}Rh_{0.01}$ (a) and $Ir_{0.99}Au_{0.01}$ (b), plotted as a function of temperature, and compared with the results for pure Ir. The most pronounced difference between the results for the doped and undoped systems occurs at low temperature. This difference gradually vanishes in the high-temperature regime, when the OHC and SHC for doped and undoped systems approach the values mainly given by their intrinsic contributions. The strong temperature dependence of the OHC and SHC for $Ir_{0.99}Rh_{0.01}$ at low temperature (see Fig. 20 (a)) stems from the extrinsic skew-scattering contributions arising due to chemical disorder, that quickly decrease with raising temperatures. As $\sigma^{\rm skew}_{\rm OH/SH} \propto \langle V_s\rangle^3/\langle V_s^2\rangle^2$, at finite temperature the scattering potential can be split into 'atomic' and 'electron-phonon' parts. While the nominator $\langle V_s\rangle \approx \langle V_a\rangle$, as $\langle V_{e-ph}\rangle = 0$ [91], the denominator accounts for both types of scattering contributions, i.e. $\langle (V_a + V_{e-ph})^2\rangle$, increasing with temperature due to an increasing amplitude of the lattice vibrations.

As is discussed in Ref. [84], in the case of $Ir_{0.99}Rh_{0.01}$, the large value of the skew scattering conductivity at $T = 0$ K estimated by $\sigma^{\rm skew}_{\rm OH/SH} \propto \frac{1}{x}\frac{1}{\Delta_d}$ [91] with $\Delta_d \approx 0.2$ eV, decreases at finite temperature due to electron-phonon scattering (with values up

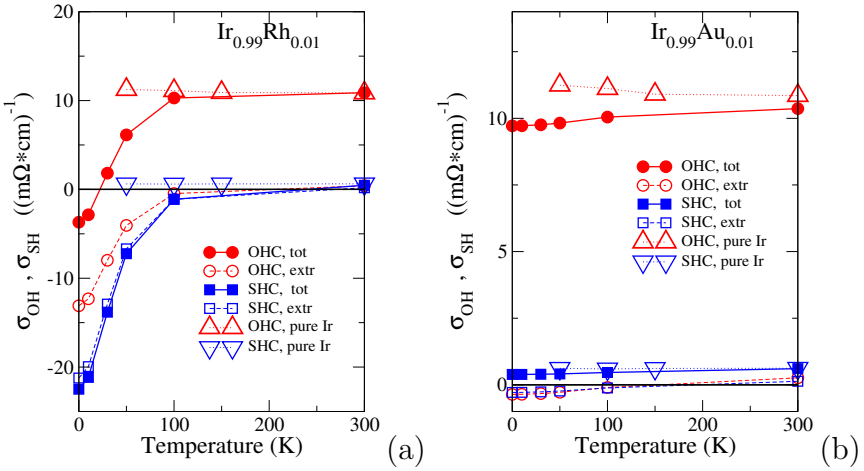

Figure 20. OH (circles) and SH (squares) conductivities for $Ir_{0.99}Rh_{0.01}$ (a) and $Ir_{0.99}Au_{0.01}$ (b) plotted as a function of temperature. Full symbols represent total values calculated accounting for vertex corrections, while open symbols show only the extrinsic contribution to the OHC and SHC. Triangles represent the results on the OHC and SHC for pure Ir.

to $\langle V_{e-ph}^2 \rangle^{1/2} \sim 0.1$ eV) according to $\sigma_{\rm OH/SH}^{\rm skew} \propto \langle V_a \rangle^3 / \langle (V_a + V_{e-ph}(T))^2 \rangle^2$. In the case of $Ir_{0.99}Au_{0.01}$, however (see Fig. 20(b)), $\Delta_d >> V_{e-ph}$ as $\Delta_d \approx 1.6$ eV, leading to a weak dependence on the temperature according to $\sigma_{\rm OH/SH}^{\rm skew} \propto \frac{1}{x}\frac{1}{\Delta_d}(1 - O(\langle V_{el-ph}^2 \rangle / \langle V_a^2 \rangle))$. At high temperatures $\sigma_{\rm SH}$ and $\sigma_{\rm OH}$ approach the intrinsic SHC and OHC, as it was seen also for $Ir_{0.99}Rh_{0.01}$.

6.1.3. Electrical conductivity of random alloys Fig. 21 represents the calculated results for the electrical resistivity of the non-magnetic random alloy $Ni_{0.33}Co_{0.33}Cr_{0.33}$ in comparison with experiment, for which a detailed discussion is given in Ref. [97]. As the $Ni_{0.33}Co_{0.33}Cr_{0.33}$ alloy is nonmagnetic, the temperature dependence of the resistivity is determined by lattice vibrations only. As seen in Fig. 21 a rather good agreement with experiment is achieved also in the case when chemical and thermal disorder are present at the same time. It should be noted that the calculations assume an undistorted lattice. Corrections to this simplification may indeed increase the resistivity remarkably (for further discussions see Ref. [98]).

7. Applications: Temperature dependent conductivity for magnetic systems

7.1. 3d transition metals

Fig. 22 (a) shows theoretical results for $\rho(T)$ of bcc-Fe due to thermal displacements $\rho_v(T)$, spin fluctuations described by the scheme MC $\rho_{\rm MC(MC)}(T)$ as well as the combination of the two influences ($\rho_{\rm v,MC(MC)}(T)$). First of all one notes that $\rho_{\rm v}(T)$ is not influenced within the adopted model by the Curie temperature $T_{\rm C}$ but is determined only by the Debye temperature. The resistivity $\rho_{\rm MC(MC)}(T)$, on the other hand, reaches

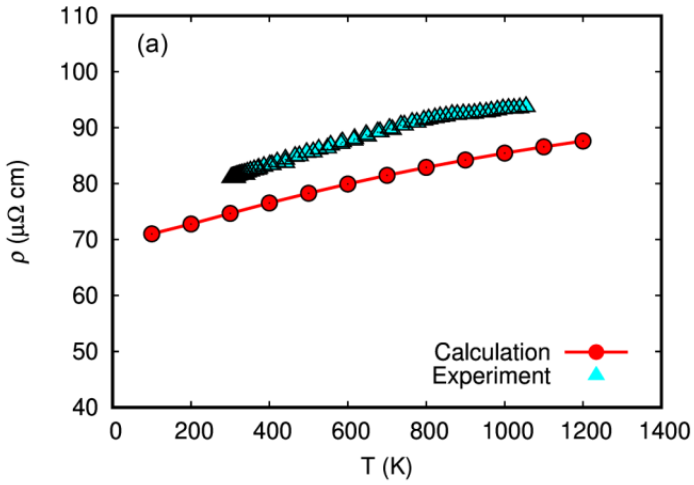

Figure 21. Electrical resistivity of the non-magnetic alloy $Ni_{0.33}Co_{0.33}Cr_{0.33}$: theory vs experiment. Calculated results are shown by red circles, while cyan triangles represent experimental data [97].

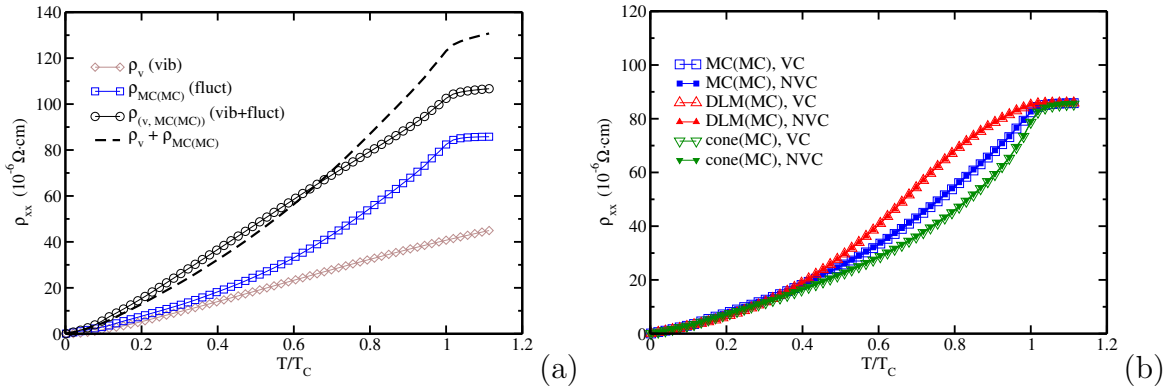

Figure 22. Temperature dependent longitudinal resistivity of bcc-Fe $\rho(T)$ obtained by accounted for thermal vibrations and spin fluctuations as described in section 3.1. (a) Accounting for vibrations (vib, diamonds), spin fluctuations using scheme MC (fluct, squares) and both (vib+fluct, circles). Dashed line represents the sum of the resistivities contributed by lattice vibrations or spin fluctuations only. (b) Accounting for spin fluctuations $\hat{e}_f = \hat{e}(\theta_f, \phi_f)$ using the schemes (see Fig. 9): MC(MC) (squares), DLM(MC) (triangles up), and cone(MC) (triangles down). The full and open symbols represent the results obtained with the vertex corrections included (VC) and excluded (NVC), respectively.

saturation for T_C as the spin disorder does not increase anymore with increasing temperature in the paramagnetic regime. Fig. 22 also shows that $\rho_v(T)$ and $\rho_{MC(MC)}(T)$ are comparable for low temperatures but $\rho_{MC(MC)}(T)$ exceeds $\rho_v(T)$ more and more for higher temperatures. Most interestingly, however, the resistivity for the combined influence of thermal displacements and spin fluctuations $\rho_{v,MC(MC)}(T)$ does not coincide with the sum of $\rho_v(T)$ and $\rho_{MC(MC)}(T)$ but exceeds the sum for low temperatures and

lies below the sum when approaching T_{C}.

Fig. 22 (b) shows the results of three different calculations including the effect of spin fluctuations as a function of the temperature. The curve $\rho_{\mathrm{MC(MC)}}(T)$ is identical with that given in Fig. 22 (a) based on Monte Carlo simulations. The curves $\rho_{\mathrm{DLM(MC)}}(T)$ and $\rho_{\mathrm{cone(MC)}}(T)$ are based on a DLM- and cone-like representation of the MC-results, respectively. For all three cases results are given including as well as ignoring the vertex corrections. As one notes, the vertex corrections play a negligible role for all three spin disorder models. This is fully in line with the experience for the longitudinal resistivity of disordered transition metal alloys: as long as the the states at the Fermi level have dominantly *d*-character the vertex corrections can be neglected in general. On the other hand, if the *sp*-character dominates inclusion of vertex corrections may alter the result in the order of 10 % [99, 53].

Comparing the DLM-result $\rho_{\mathrm{DLM(MC)}}(T)$ with $\rho_{MC(MC)}(T)$ one notes in contrast to the results for $M(T)$ shown above (see Fig. 8 (right)) quite an appreciable deviation. This implies that the restricted collinear representation of the spin configuration implied by the DLM-model introduces errors for the configurational average that seem in general to be unacceptable. For the Curie temperature and beyond in the paramagnetic regime $\rho_{\mathrm{DLM(MC)}}(T)$ and $\rho_{\mathrm{MC}}(T)$ coincide, as it was shown formally before [100].

Comparing finally $\rho_{\mathrm{cone(MC)}}(T)$ based on the conical representation of the MC spin configuration with $\rho_{\mathrm{MC(MC)}}(T)$ one notes that also this simplification leads to quite strong deviations from the more reliable result. Nevertheless, one notes that $\rho_{\mathrm{DLM(MC)}}(T)$ agrees with $\rho_{\mathrm{MC(MC)}}(T)$ for the Curie temperature and also accounts to some extent for the impact of the transversal components of the magnetization.

The theoretical results for bcc-Fe ($\Theta_{\mathrm{Debye}} = 420$ K) based on the combined inclusion of the effects of thermal displacements and spin fluctuations using the MC scheme ($\rho_{\mathrm{v,MC(MC)}}(T)$) are compared in Fig. 23 (top) with experimental data ($\rho_{\mathrm{exp}}(T)$). For the Curie temperature obviously a very good agreement with experiment is found while for lower temperatures $\rho_{\mathrm{v,MC(MC)}}(T)$ exceeds $\rho_{\mathrm{exp}}(T)$. This behavior correlates well with that of the temperature dependent reduced magnetic moment $M(T)$ shown in Fig. 8 (middle). The too rapid decrease of $M_{\mathrm{MC}}(T)$ compared with experiment implies an essentially overestimated spin disorder at any temperature leading in turn to a too large resistivity $\rho_{\mathrm{v,MC(MC)}}(T)$. On the other hand, using the temperature dependence of the experimental reduced magnetic moment $M_{\mathrm{exp}}(T)$ to set up the temperature dependent spin configuration as described above a very satisfying agreement of $\rho_{\mathrm{v,MC(expt)}}(T)$ is found with the experimental resistivity data $\rho_{\mathrm{exp}}(T)$. Note also that above T_C the calculated resistivity reaches saturation in contrast to the experimental data where the continuing increase of $\rho_{\mathrm{exp}}(T)$ can be attributed to the longitudinal spin fluctuations leading to a temperature dependent distribution of local magnetic moments on Fe atoms [80]. However, this contribution was not accounted for because of the restriction in present calculations using a fixed value for the local reduced magnetic moments.

Fig. 23 (right) shows corresponding results for the temperature dependent resistivity of fcc-Ni ($\Theta_{\mathrm{Debye}} = 375$ K). For the ferromagnetic (FM) regime the theoretical results are

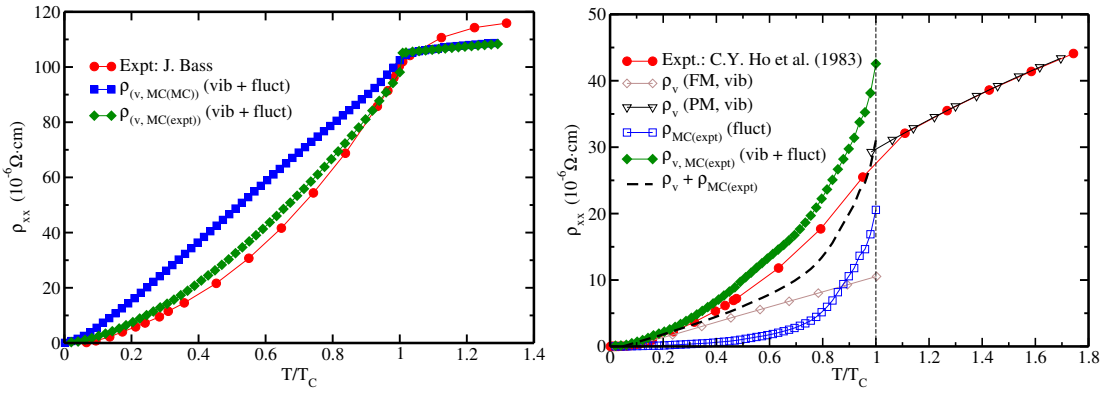

Figure 23. Left: Temperature dependent longitudinal resistivity of bcc-Fe $\rho(T)$ obtained by accounted for thermal vibrations and spin fluctuations using the scheme MC (vib+fluct(MC(MC)), squares) and a mean-field fit to the experimental temperature magnetic moment $M_{\rm exp}$ (vib+fluct(MC(exp)), diamonds) compared with experimental data (circles) [90]. Right: corresponding results for fcc-Ni. In addition results are shown accounting for thermal displacements (vib) only for the ferromagnetic (FM) as well paramagnetic (PM) regime. The dashed line represents the sum of the resistivity contributed by lattice vibrations or spin fluctuations only. Experimental data have been taken from Ref. [101].

comparable in magnitude when only thermal displacements ($\rho_{\rm v}(T)$) or spin fluctuations ($\rho_{\rm MC(expt)}(T)$) are accounted for. In the later case the mean field $w(T)$ has been fitted to the experimental $M(T)$-curve. Taking both into account leads to a resistivity ($\rho_{\rm v,MC(expt)}(T)$) that is well above the sum of the individual terms $\rho_{\rm v}(T)$ and $\rho_{\rm MC(expt)}(T)$. Comparing $\rho_{\rm v,MC(expt)}(T)$ with experimental data $\rho_{\rm exp}(T)$ our finding shows that the theoretical results overshoots the experimental one the closer one comes to the critical temperature. This is a clear indication that the assumption of a rigid spin moment is quite questionable as the resulting contribution to the resistivity due to spin fluctuations is much too small. In fact the simulations of Ruban et al. [80] on the basis of a longitudinal spin fluctuation Hamiltonian led in the case of fcc-Ni to a strong diminishing of the average local magnetic moment when the critical temperature is approached from below (about 20 % compared to $T = 0$ K). For bcc-Fe, the change is much smaller (about 3 %) justifying in this case the assumption of a rigid spin moment. Taking the extreme point of view that the spin moment vanishes completely above the critical temperature or the paramagnetic (PM) regime only thermal displacements have to be considered as a source for a finite resistivity. Corresponding results are shown in Fig. 23 (bottom) together with experimental data. The very good agreement between both obviously suggests that remaining spin fluctuations above the critical temperature are of minor importance for the resistivity of fcc-Ni.

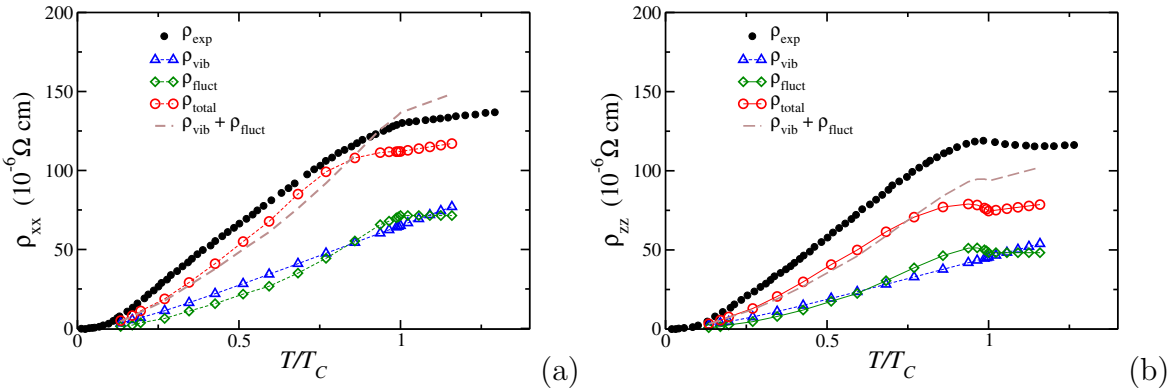

Figure 24. (Color online) Temperature-dependent electrical resistivity of hcp Gd: in-plane (a), and out of plane (b) components. The various symbols represent: black solid circles – experimental results [103], empty blue triangles – only thermal lattice vibrations, empty green diamonds – only spin fluctuations, empty red circles – total resistivity including both effects simultaneously, brown dashed line corresponds to the sum of individual contributions [102].

7.2. The ferromagnetic hcp Gd

Impact of finite temperatures on the transport properties of Gd has been studied in Ref. [102]. One of the central transport properties of metallic systems is their electrical resistivity. The experimentally measured temperature-dependent resistivity of Gd exhibits an anisotropy with different magnitudes along the hexagonal axis (ρ_{zz}) and in the basal plane (ρ_{xx}) [103] (see Fig. 24). Both $\rho(T)$ curves are characterized by an abrupt slope change close to the Curie temperature.

In addition, the temperature dependence caused separately by different contributions to the total $\rho(T)$, i.e. only by lattice vibrations (vib) or only by magnetic fluctuations (fluct), have been investigated in Ref. [102], which appear to be of comparable magnitude. This led to the conclusion that these sources of the temperature-dependent resistivity are additive only in the case of the weak disorder (low temperatures), which does not hold when approaching the Curie temperature (strong disorder) [104]. In this regime they must be taken into account simultaneously, since only then the overall behavior of the resistivity curves agrees well with experiment. This allows to conclude that the maximum of the experimental ρ_{zz} (close to the Curie temperature) is not a result of short range magnetic order as it was suggested in the earlier literature [103], since the present calculations are based on the single-site CPA. The results in Ref. [102] suggest its origin to be a combination of two competitive mechanisms. On the one hand side, this is the thermally induced increase of disorder, leading to an increase of the electrical resistivity. On the other hand side, the DOS around E_F, characterizing quantitatively the electrical conductivity, increases with increasing temperature at $T < T_c$, which effectively reduces the resistivity.

While the calculated resistivities agree with the experiment rather well, there is a quantitative underestimation (see Fig. 24). This can have various sources. One could be

the so-called 'frozen'-potential approximation used in the calculations. A second reason, which is more crucial for ρ_{zz}, might be the neglect of the anisotropy of the thermal atomic displacements. A third source for discrepancy may be the use of the single-site approximation by the CPA, which neglects the coherent scattering or interference effects which might show up in multiple scattering.

The results for the anomalous Hall resistivity (AHR) of Gd are shown in Fig. 25 (a) in comparison with experimental results (for polycrystalline samples as well as single crystals) and theoretical results, obtained on the basis of model calculations by Fert [105]. One can see that the anomalous Hall resistivity shows a pronounced temperature dependence: the resistivity increases from zero at $T = 0$ K to a maximum value just below the Curie temperature and then drops to zero as the magnetization vanishes with further increasing temperature. Overall there is qualitative and quantitative agreement of our first principles results with experiment as well as with the model calculations. In Fig. 25 (b) the individual contributions arising from the scattering by the lattice vibrations and spin fluctuations are shown. One can see that both mechanisms provide contributions nearly of the same order of magnitude. The qualitative behavior of the total AHR is determined by the scattering due to spin disorder, while the contribution due to lattice vibrations shows, as expected, a monotonous increase with temperature. It is interesting to compare the sum of the individual contributions with the total AHR. From Fig. 25 (b) one can see that the total AHR significantly exceeds the sum of these contributions. Therefore for the correct description of the total AHR it is necessary to account simultaneously for the combination of scattering due to the thermal lattice vibrations and spin fluctuations.

Comparing the calculated anomalous Hall resistivity with experimental data, one

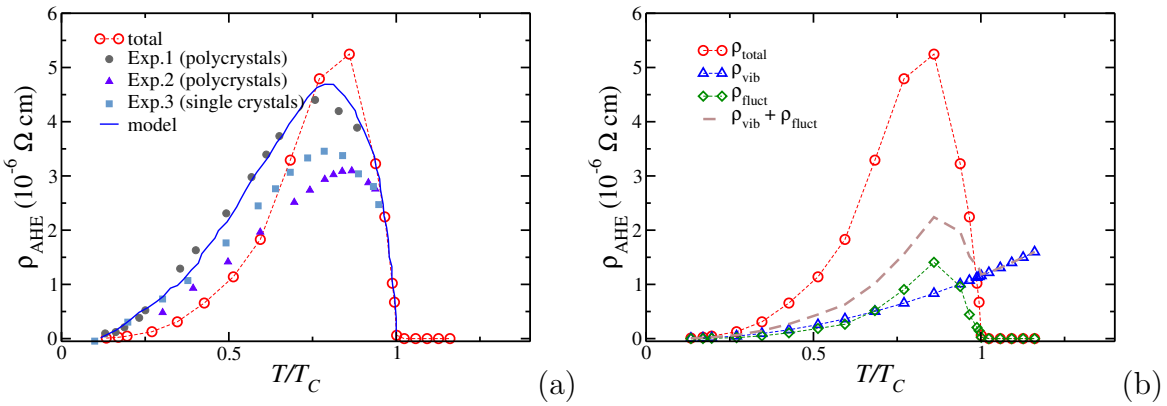

Figure 25. Anomalous Hall resistivity for Gd as a function of temperature: (a) in comparison with experimental results (Exp. 1 – Ref. [106], Exp. 2 – Ref. [106], Exp.3 – Ref. [107, 108]) and results from model calculations [105]; (b) individual contributions. The used symbols represent: empty blue triangles – only thermal lattice vibrations, empty green diamonds – only spin fluctuations, empty red circles – total resistivity including both effects simultaneously, brown dashed line corresponds to the sum of individual contributions.

notices that the discrepancy is more pronounced at low temperatures, and is rather weak at the temperature approaching T_C (see Fig. 25).

7.3. AFM-FM phase transition of FeRh

The finite temperature properties of the electrical resistivity of FeRh making use of the AAM were studied in Ref. [109]. To account for the effect of spin fluctuations in these calculations, the temperature dependent magnetization of the Fe sublattice has been obtained via Monte Carlo simulations, using exchange coupling parameters calculated in an ab-initio way [110].

Figure 26(a) shows the electrical resistivity, $\rho_{xx}(T)$, calculated for ordered FeRh with CsCl structure, accounting for the impact of thermal spin and lattice excitations, in comparison with the experimental data. One can clearly see a rather good agreement between the theoretical and experimental results. In particular, this concerns the difference $\rho_{xx}^{AFM}(T_m) - \rho_{xx}^{FM}(T_m)$, that is a result of a steeper increase of the AFM-resistivity with temperature, when compared to that for the FM state. Note that the experimental measurements have been performed for a sample with 1% intermixing between Rh and Fe sublattices leading to a finite residual resistivity at $T \to 0$ K, and as a consequence in a shift of the experimental $\rho_{xx}(T)$ curve with respect to the theoretical results [83].

The separate contributions of spin fluctuations and lattice vibrations to the electrical resistivities, $\rho_{xx}^{\mathrm{f}}(T)$ and $\rho_{xx}^{\mathrm{v}}(T)$, calculated for the AFM and FM states are shown in Fig. 26(b). For both magnetic states spin moment fluctuations have a dominant

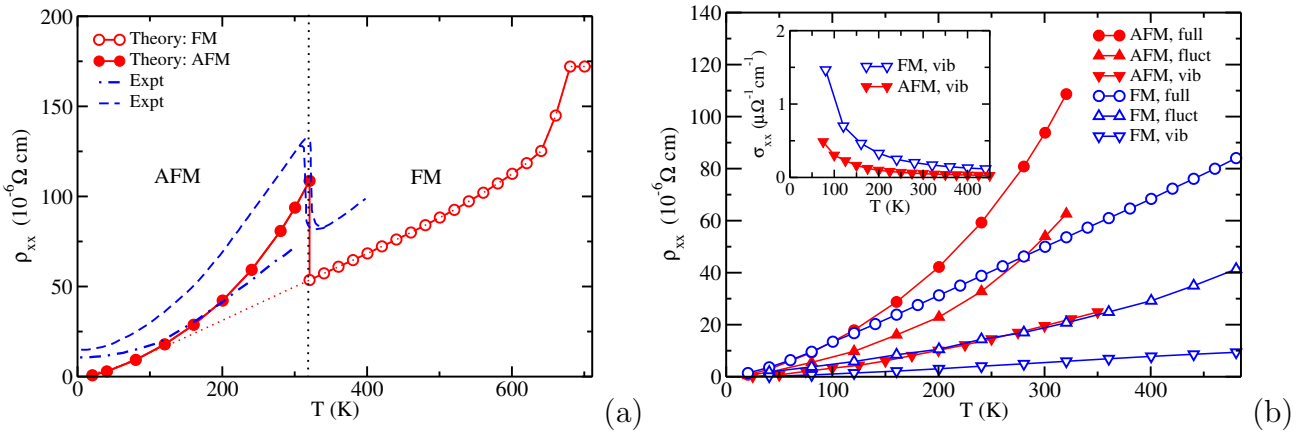

Figure 26. (a) Calculated longitudinal resistivity (closed circles - AFM state, open circles - FM state) in comparison with the experiment [111]. The dashed line represents the results for $Fe_{0.49}Rh_{0.51}$, while the dash-dotted line gives results for $(Fe\text{-}Ni)_{0.49}Rh_{0.51}$ with the Ni concentration $x = 0.05$ to stabilize the FM state at low temperature); (b) electrical resistivity calculated for the AFM (closed symbols) and FM (open symbols) states accounting for all thermal scattering effects (circles) as well as effects of lattice vibrations (diamond) and spin fluctuations (squares) separately. The inset shows the temperature dependent longitudinal conductivity for the AFM and FM states due to lattice vibrations only [109].

impact on the resistivity when compared to the thermal lattice displacements. One can also see, that both components, $\rho^{\mathrm{f}}_{xx}(T)$ and $\rho^{\mathrm{v}}_{xx}(T)$, in the AFM state have a steeper increase with temperature when compared to the FM state.

In order to clarify the origin of such a behavior, the results were discussed using Mott's model [112] that distinguishes between delocalized *sp*-electrons that primarily determine the transport properties due to their high mobility, and localized *d*-electrons. This allows in particular to consider separately the following factors which determine the conductivity (see, e.g. [113]): (i) the carrier (having essentially *sp*-character) concentration n and (ii) relaxation time $\tau \sim [V^2_{\mathrm{scatt}} n(E_F)]^{-1}$, where V_{scatt} is the average scattering potential and $n(E_F)$ the total density of states at the Fermi level. Corresponding discussions were done on the basis of the electronic structure.

This model was applied in particular to explain the abrupt change of the $\rho(T)$ dependence in the vicinity of the Curie temperature using the element projected DOS for Fe and Rh shown in Fig. 27 for two temperatures just below and above T_C. In particular, Fig. 27 demonstrates the induced spin-splitting of the Rh electronic states

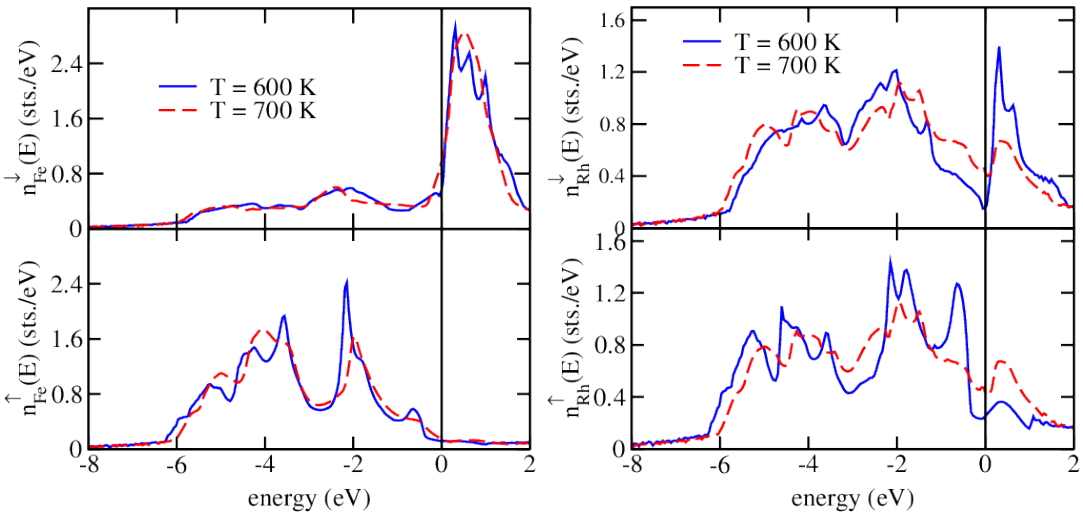

Figure 27. Comparison of the element resolved Fe (left) and Rh (right) DOS calculated for the FM (solid line) and PM (dashed line) states at finite temperatures $T = 600$ K ($M/M_0 = 0.66$) and $T = 700$ K ($M/M_0 = 0$) [109].

in FeRh for $T < T_C$ ($T = 600$ K (left panel)), which disappears above T_C ($T = 700$ K (right panel)), so that the Rh DOS increases at the Fermi level. As a consequence, the differences in the $\rho(T)$ behavior in the vicinity to T_C for different systems may be attributed to specific features of their electronic structures relevant to their PM states. In particular, an increase of the Rh DOS at the Fermi level should lead to the sharp increase of the resistivity as the critical temperature is approached, since $\rho(T)$ is inversely proportional to the relaxation time τ, i.e. $\rho(T) \sim [V^2_{\mathrm{scatt}} n(E_F)]$ [109].

Fig. 28(a) shows the calculated anomalous Hall resistivity for FeRh in the FM state (ρ_{xy}), represented as a function of temperature, in comparison with experimental data

[114]. As the FM state is unstable in pure FeRh at low temperatures, the measurements were performed for $(Fe_{0.965}Ni_{0.035})Rh$, for which the FM state has been stabilized by Ni doping. The calculations have been performed both, for the pure FeRh compound as well as for FeRh with 5% Ni doping, $(Fe_{0.95}Ni_{0.05})Rh$, that is found from the calculations to be ferromagnetically ordered down to T =0 K. As can be seen, the magnitude of $\rho_{xy}(T)$ increases in a more pronounced way for the undoped system. Nevertheless, both results are in rather good agreement with experiment.

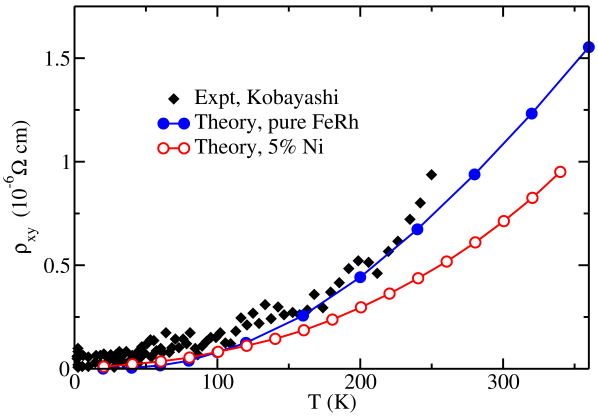

Figure 28. The temperature dependence of the anomalous Hall resistivity for the FM state of $(Fe_{0.95}Ni_{0.05})Rh$ in comparison with experimental data [114].

7.4. Fe-intercalated 2H-TaS_2

The finite temperature transport properties of the 2H-$Fe_{0.28}TaS_2$ alloy were calculated [115] accounting for both temperature induced lattice vibrations and spin fluctuations [44]. The information on the temperature dependent magnetization has been taken from experiment [116]. The electrical resistivity $\rho_{xx}(T)$ as well as $\rho_{xy}(T)$, characterizing the AHE, are shown in Fig. 29 as a function of temperature. As the occupation of the Fe sublattice is incomplete, the Fe concentration is non-stoichiometric implying $x_{Fe} \approx 1/3$, 'chemical' disorder has an additional impact on the resistivity leading to a finite residual resistivity in the system.

As one can see, the resistivity $\rho_{xx}(T)$ contribution due to spin fluctuations has a very weak dependence on temperature. On the other hand, the temperature induced lattice vibrations result in a strong temperature dependence of $\rho_{xx}(T)$, leading to a change of the slope at a temperature close to the Curie temperature. This implies that the temperature dependence of $\rho_{xx}(T)$ around T_C cannot be associated with the direct impact of the temperature induced magnetic disorder on the electron scattering by spin fluctuations and with this on the electron transport, but with the impact of the magnetic disorder on the 'electron-phonon' scattering. The $\rho_{zz}(T)$ component shows a higher residual value at $T = 0$ K when compared to $\rho_{xx}(T)$, and also a change of the slope close to T_C, approaching the $\rho_{xx}(T)$ curve with increasing temperature. It is worth to

mention again the temperature induced modifications of the electronic structure, namely, the smearing of the energy bands due to electron scattering via lattice vibrations. This can result in a rather fast increase of the resistivity due to an increasing cross-section for the interband scattering. However, a further smearing with increasing the temperature leads to a saturation of the number of channels for the interband scattering and as a result - to the observed change of the slope of the $\rho_{xx}(T)$ curve. Another consequence of the smearing of the electronic states is the decrease of the anisotropy of the transport properties at high temperature. Note also that in general, the results of the present calculations are in good agreement with experiment and demonstrate the leading role of lattice vibrations for the temperature dependence of $\rho_{xx}(T)$.

The off-diagonal resistivity $\rho_{xy}(T)$ as a function of temperature is compared in Fig. 29(b) with experimental results showing reasonable agreement. It has a maximum at $T \approx 30$ K and goes to 0 at the Curie temperature due to magnetic disorder in the system, demonstrating the crucial role of spin fluctuations for the temperature-dependence of $\rho_{xy}(T)$.

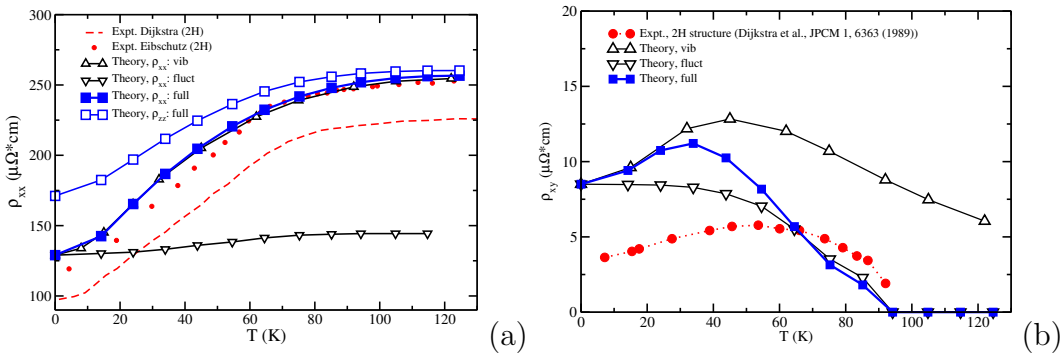

Figure 29. (a) Temperature-dependent longitudinal resistivities, $\rho_{xx}(T) = \rho_{yy}(T)$ and $\rho_{zz}(T)$ (filled and open squares),for ferromagnetic disordered $Fe_{0.28}TaS_2$. The dots [117] and the dashed line [118] represent corresponding experimental data. (b) Temperature-dependent transverse resistivity, $\rho_{xy}(T)$. Results for $\rho_{xx}(T)$ and $\rho_{xy}(T)$ that were obtained accounting only for lattice vibrations and spin fluctuations are represented in both cases by up and down triangles, respectively [115]

.

7.5. Doped Permalloy (Py)

The temperature dependence of the electrical resistivity of chemically disordered Permalloy (Py) $Fe_{0.19}Ni_{0.81}$, studied in Ref. [119] using the AAM is shown in Fig. 30 in comparison with the experimental data and with the results of calculations by Starikov et al. [69], who modeled the temperature induced disorder by means of the supercell technique. The SPRKKR calculation of $\rho_{aver} = \frac{1}{3}(2\rho_{xx} + \rho_{zz})$ accounts quite well for the trend with a reasonable agreement with experiment. Some discrepancy with the results of Starikov et al. [69] may be attributed to the different models used to describe the

thermal disorder by Starikov et al. [69] (supercells) in contrast to the CPA-based AAM used in the SPRKKR calculations.

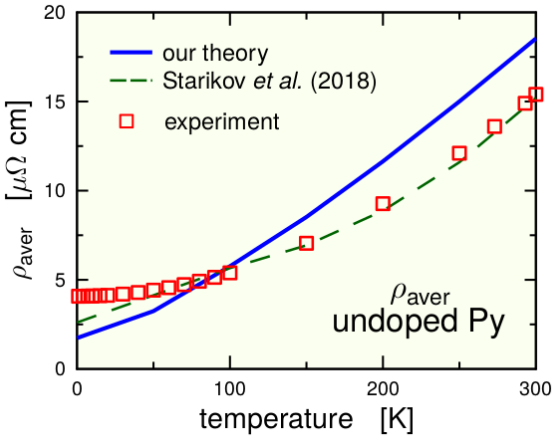

Figure 30. Dependence of the resistivity ρ_{aver} of undoped Py on the temperature as obtained by our calculation (blue solid line), by calculations of Starikov et al. [69] (green dashed line), and by experiment [101] (red squares) [119].

In addition to Py, the electrical conductivities as well as the AHE and SHE have been investigated for Py doped by 3*d* elements. Fig. 31 represents the temperature dependence of the transverse charge and spin conductivities, σ_{xy} (left) and σ^z_{xy} (right), respectively, for undoped Py (diamonds) and for Py doped with 6% of V (asterisks), Co (crossed circles), Pt (triangles), and Au (squares). A strong impact of the vertex corrections on the AHE and SHE in the low-temperature region can be seen in Fig. 32 for Co and Au doped Py, which decreases however rather quickly when the temperature increases. As is discussed in Sec. 6.1.2 as well as in Ref. [84], this effect can be attributed to the competition of the electron scattering due to chemical disorder and on thermally induced atomic displacements with their amplitude increasing with a temperature.

7.6. The high entropy alloy $Ni_{0.33}Co_{0.33}Fe_{0.33}$

The electrical resistivity calculated for FM-ordered $Ni_{0.33}Co_{0.33}Fe_{0.33}$ [97] is plotted in Fig. 33. The rapid increase of the resistivity at $T \lesssim T_C$ is determined by a dominating scattering by thermal spin fluctuations. This contribution reaches saturation above T_C, i.e. in the magnetically disordered state, for which the strength of the electron scattering on thermal spin fluctuations also saturates. As a consequence, the temperature dependence of the resistivity above T_C is determined by the electron scattering on lattice vibrations, which grows linearly with temperature. The difference between the experimental and theoretical results on $\rho(T)$ below T_C is ascribed to a discrepancy between the experimental temperature dependence of the magnetization and the magnetization calculated within the Monte Carlo simulations based on the classical Heisenberg model [97].

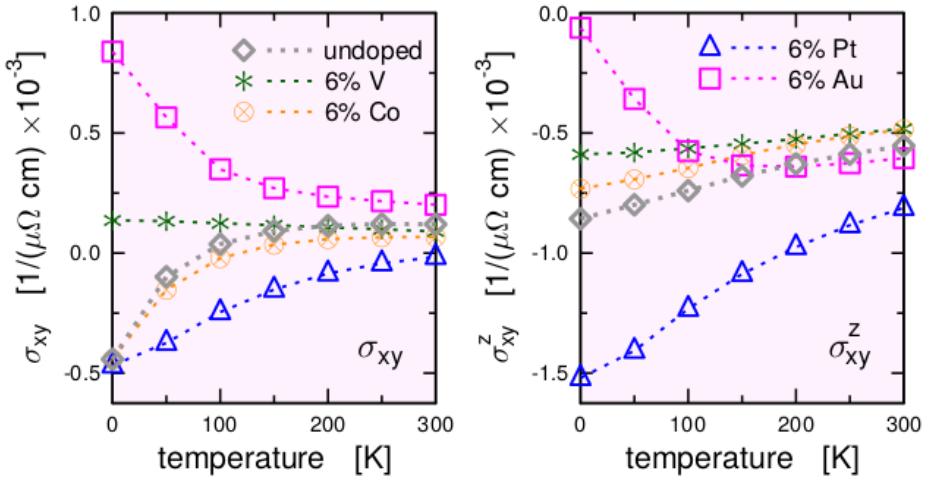

Figure 31. Theoretical temperature-dependence of σ_{xy} (left) and σ^z_{xy} (right) for undoped Py (diamonds) and for Py doped with 6% of V (asterisks), Co (crossed circles), Pt (triangles), and Au (squares) [119].

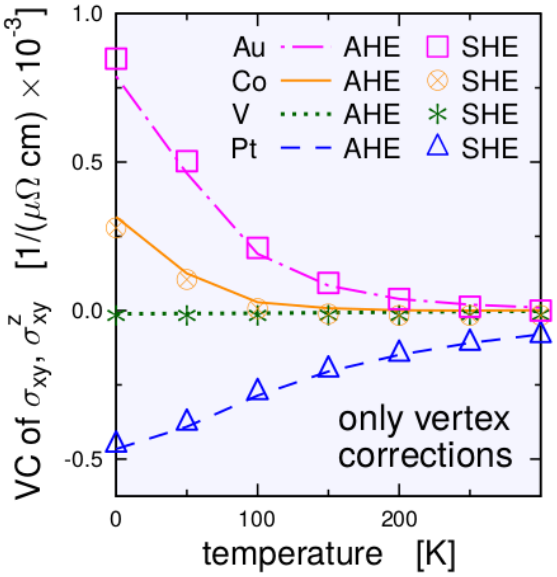

Figure 32. The temperature-dependence of the contributions to σ_{xy} (lines) and σ^z_{xy} (markers) due to the vertex corrections for Py doped by 6% of V, Co, Pt, and Au [119].

7.7. Solid solutions of the 3d-transition metals

In the case of random alloys, two types of atomic displacements with different origin may occur. One is due to thermally induced lattice vibrations, which were already discussed above as they are responsible for temperature dependence of the transport properties. Another type of displacements stems from the different atomic size of neighboring atoms in a chemically disordered system, which leads in turn to randomly

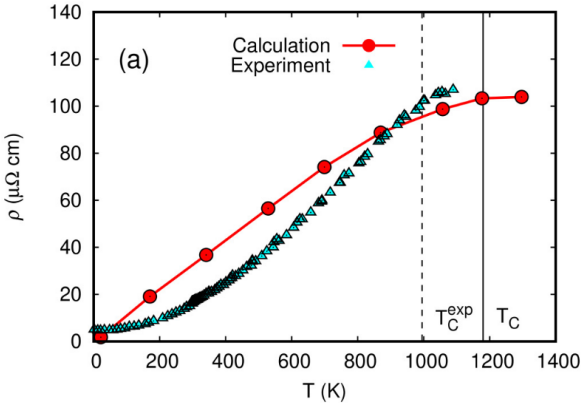

Figure 33. Electrical resistivity of ferromagnetic $Ni_{0.33}Co_{0.33}Fe_{0.33}$: theory vs experiment. Calculated results are shown by red circles, while cyan triangles represent experimental data [97].

distributed local distortions in the alloy. These displacements can also be treated within the AAM, but have only a weak dependence on the temperature. The combined effects of these displacements on the transport properties have been discussed together with the impact of chemical disorder in Ref. [98], considering the medium-entropy fcc NiCoMn equiatomic solid solution alloys. Fig. 34 illustrates the resistivity enhancements ($\Delta\rho$) due to two types of atomic displacements, static and thermally-induced, plotted as a function of temperature when the static displacement is included (red dots) or not (black diamonds), respectively.

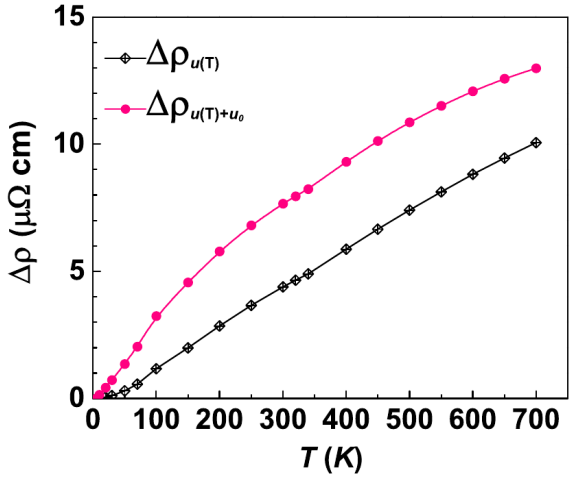

Figure 34. The resistivity enhancement $\Delta\rho(T)$ ($\mu\Omega\cdot$ cm) of NiCoMn due to the effect of thermal displacements $u(T)$, with (red dots) and without (black diamonds) taking into account the static displacements u_0 [98].

In the absence of the static displacements, the thermal displacement induced resistivity enhancement $\Delta\rho(u(T))$ increases almost linearly with temperature in the

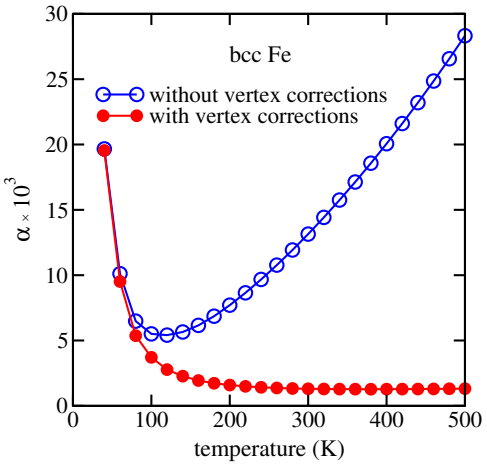

Figure 35. The Gilbert damping parameter for bcc-Fe as a function of temperature. Full (open) symbols give results with (without) the vertex corrections [59].

regime above 100 K. However, accounting for static displacements in addition, one can see that the temperature dependent resistivity enhancement $\Delta\rho(\langle(\vec{u}_0+\vec{u}(T))^2\rangle^{1/2})$ changes remarkably. This is due to the fact that the coupling between the $\vec{u}_0$ and $\vec{u}(T)$ contributes a $\langle\vec{u}_0\cdot\vec{u}(T)\rangle^{1/2}$ term in the expansion of $\sqrt{\langle(\vec{u}_0+\vec{u}(T))^2\rangle}$.

8. Applications: Gilbert damping at finite temperature

Similar to transport properties one can calculate the temperature dependent Gilbert damping parameter for magnetic materials. The expression given by Eq. (21) for disordered alloys, can be used also to take thermally induced lattice vibrations and spin fluctuations into account. In this case the configurational average can again be calculated using the AAM formalism. As an example, we present the results for the Gilbert damping parameter at finite temperature for pure 3d transition metals [57, 59] calculated accounting for the temperature induced atomic displacements via the alloy analogy scheme. This leads, even for pure systems, to a finite electronic lifetime and in this way to a finite value for α. First, we demonstrate the role of vertex corrections for the temperature dependence of α, using bcc Fe as a prototype system. Fig. 35 represents the Gilbert damping parameter (with and without vertex corrections) for pure Fe in the presence of temperature induced disorder and plotted as a function of temperature. A significant impact of the vertex corrections is noticeable, similar to the one found for the binary alloy $Fe_{1-x}V_x$, depending on the concentration of V. However, one can see some difference concerning the impact of thermal and chemical disorder on the Gilbert damping. Dealing with temperature effects via the alloy analogy model, the system is considered as a pseudo-alloy consisting of a fixed number of components representing different types of displacements. Thus, in this case the temperature effect is associated with the increase of the disorder in the system caused only by an increase of the displacement amplitude, or, in other words – with the strength of the scattering

potential experienced by the electrons represented by $\underline{t}^n(T) - \underline{t}^n_0$. In the case of a random alloy $A_{1-x}B_x$ the variation of the scattering potential, as well as the difference $\underline{t}^n_B - \underline{t}^n_A$, upon changing the concentration is less pronounced for small amounts of impurities B and the concentration dependence is determined by the amount of scatterers of different types. However, when the concentration of the impurities increases, the potentials of the components are also modified (this is reflected, e.g. in a shift of electronic states with respect to the Fermi level) and this can lead to a change of the concentration dependence of the vertex corrections. Furthermore, one can see in Fig. 35, that a neglect of the vertex corrections for $\alpha(T)$ leads to wrong results at high temperatures, similar to the case of high V concentrations in $Fe_{1-x}V_x$.

Next, we compare the Gilbert damping parameters for Fe, Co and Ni calculated as a function of temperature, with corresponding experimental results available in the literature. The Gilbert damping obtained for bcc Fe (circles, $a = 5.44$ a.u.) is compared in Fig. 36(a) with experiment showing a rather good agreement at temperatures above 100 K despite the scattering of the experimental results. A more detailed comparison is done in Ref. [57].

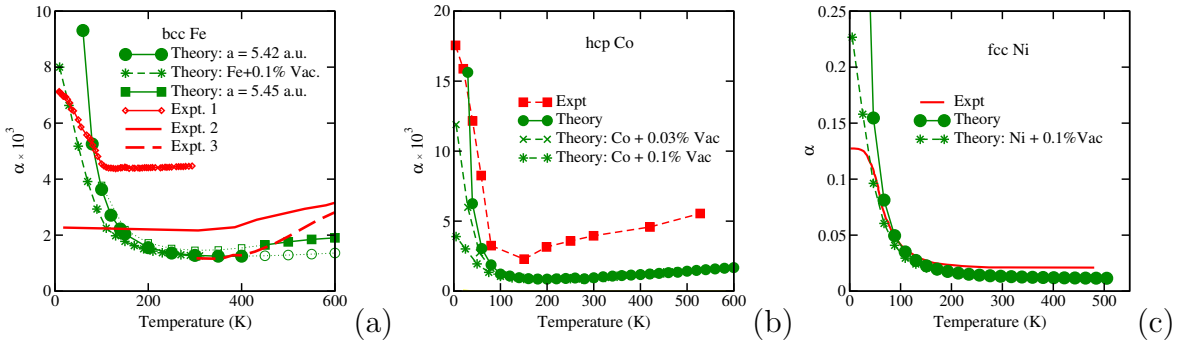

Figure 36. Temperature variation of the Gilbert damping parameter of pure systems. Comparison of theoretical results with experiment: (a) bcc-Fe: circles and squares show the results for ideal bcc Fe for two lattice parameters, $a = 5.42$ a.u. and $a = 5.45$ a.u.; stars show theoretical results for bcc Fe ($a = 5.42$ a.u.) with 0.1% of vacancies (Expt. 1 - Ref. [121], Expt. 2 - Ref. [120], Expt. 3 - Ref. [122]); (b) hcp-Co: circles show theoretical results for ideal hcp Co, stars - for Co with 0.03% of vacancies, and 'pluses' - for Co with 0.1% of vacancies (Expt. Ref. [120]); and (c) fcc-Ni (Expt. Ref. [120]).

Results for the temperature dependent Gilbert damping parameter α for hcp Co are presented in Fig. 36(b) which shows, despite certain underestimation, reasonable agreement with the experimental results [120]. The general trends at low and high temperatures are similar to those seen in Fe.

The results for pure Ni are given in Figs. 36(c) and 37(top) that show in full accordance with experiment a rapid decrease of α with increasing temperature until a regime with a weak variation of α with T is reached. Adding small amount of Cu to Ni, even less than 1 at.% Cu, strongly reduces the conductivity-like behavior (see, e.g. Ref. [60]) at low temperatures while leaving the high-temperature behavior essentially

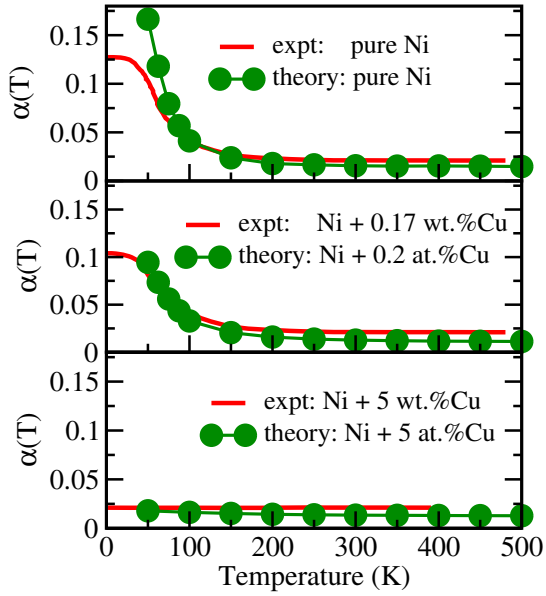

Figure 37. Temperature variation of Gilbert damping of pure Ni and Ni with Cu impurities: present theoretical results vs experiment [120].

unchanged. This is shown in the middle panel of Fig. 37. A further increase of the Cu content leads to impurity-scattering processes responsible for the band broadening dominating α. This effect completely suppresses the conductivity-like behavior in the low-temperature regime because of the increase of scattering events due to chemical disorder (see Fig. 37, bottom). This is fully in line with the experimental data, providing a straightforward explanation for their peculiar variation with temperature and composition.

9. Applications in spectroscopy

9.1. One-step theory of photo emission

The AAM also allows to investigate the temperature-dependence of photoemission. This was demonstrated making use of the one-step theory of photoemission. The main idea of the one-step model is to describe the actual excitation process, the transport of the photoelectron to the surface as well as the escape into the vacuum as a single quantum mechanical process [123]. It is based on Fermi's golden rule and was originally implemented for ordered surfaces using the multiple scattering KKR Green function formalism (for more details see the review [124]). This approach has been generalized to describe the photoemission of disordered alloys by means of the CPA [125, 126] and recently it was extended to deal with thermal lattice vibration and spin fluctuation (in magnetic materials) effects exploiting the AAM approach described above. Based on the CPA approach the temperature-dependent spin-density matrix ρ at a given kinetic energy ϵ_f and wave vector $\vec{k}_\parallel$ can be written in the following form:

$$\begin{aligned}\langle \overline{\rho}_{ss'}(\epsilon_f, \vec{k}_\parallel, T)\rangle \;\propto\; & \langle \overline{\rho}^{at}_{ss'}(\epsilon_f, \vec{k}_\parallel, T)\rangle + \langle \overline{\rho}^{c}_{ss'}(\epsilon_f, \vec{k}_\parallel, T)\rangle \\ & + \langle \overline{\rho}^{inc}_{ss'}(\epsilon_f, \vec{k}_\parallel, T)\rangle + \langle \overline{\rho}^{surf}_{ss'}(\epsilon_f, \vec{k}_\parallel, T)\rangle, \end{aligned} \tag{44}$$

with contributions from a purely atomic part (at), a coherent part (c) with multiple scattering involved and an incoherent (inc) part as described in detail in Refs. [127, 128] in the context of chemical disorder in alloys. The third contribution which appears due to the CPA-averaging procedure represents an on-site quantity that behaves DOS-like [127]. The last contribution defines the surface ($surf$) part of the spin-density matrix. As dispersing and non-dispersing contributions are clearly distinguishable we can define the spin-density matrix which describes the angle-integrated (AI) photoemission spectra (PES) (i.e. AI-PES)

$$\begin{aligned}\langle \overline{\rho}_{ss'}^{\mathrm{AI-PES}}(\epsilon_f, \vec{k}_\parallel, T)\rangle \sim \langle \overline{\rho}_{ss'}^{at}(\epsilon_f, \vec{k}_\parallel, T)\rangle \\ + \langle \overline{\rho}_{ss'}^{inc}(\epsilon_f, \vec{k}_\parallel, T)\rangle + \langle \overline{\rho}_{ss'}^{surf}(\epsilon_f, \vec{k}_\parallel, T)\rangle \ ,\end{aligned} \tag{45}$$

where the $\vec{k}$-dependence in the atomic and incoherent contributions is only due to the final state. A $\vec{k}$-averaging is not necessary because the $\vec{k}$-dependence of the (SP)LEED-type final state is very weak and can be neglected in explicit calculations. Furthermore, by use of the single-scatter approximation for the final state the $\vec{k}$-dependence vanishes completely. This way a direct comparison to corresponding measurements is possible in both cases. From this the intensity of the photocurrent results in:

$$I(\epsilon_f, \vec{k}_\parallel, T) \ = \ Tr\left(\ \rho_{ss'}(\epsilon_f, \vec{k}_\parallel, T) \ \right) \ , \tag{46}$$

with the corresponding spin polarization vector given by:

$$\vec{P} \ = \ \frac{1}{I} \, Tr \ (\ \boldsymbol{\sigma} \ \rho \ ) \ . \tag{47}$$

Finally, the spin-projected photocurrent is obtained from the following expression:

$$I_{\hat{n}}^{\pm} \ = \ \frac{1}{2} \ \left(\ 1 \ \pm \ \hat{n} \cdot \vec{P} \ \right) \ , \tag{48}$$

with the spin polarization ($\pm$) referring to an arbitrary vector $\hat{n}$.

9.1.1. Soft and hard x-ray angle-resolved (AR) temperature-dependent photoemission The impact of lattice vibrations and spin fluctuations have been investigated for the soft and hard x-ray angle-resolved photoemission regimes using the temperature-dependent one-step theory sketched above. The validity of this approach has been demonstrated in Ref. [10] with illustrative soft and hard x-ray calculations for Au (see Fig. 38) and Pt, as well as by direct comparison to experimental soft x-ray data from W(110) (see Fig. 39). As one can see in Fig. 38, the photoemission spectra for Au(111) for two different photon energies of 1.0 and 6.4 keV, calculated using the AAM-based approach correctly converge at high energy and/or photon energies to the so called XPS limit in photoemission, in particular the development of matrix-element-weighted density-of-states (MEW-DOS)-like features in the intensity distribution. Note that Au was chosen as a typical transition metal with a low Debye temperature of $\Theta_D = 165$ K. The left panel shows angle-resolved intensity distributions for an excitation energy of 1.0 keV

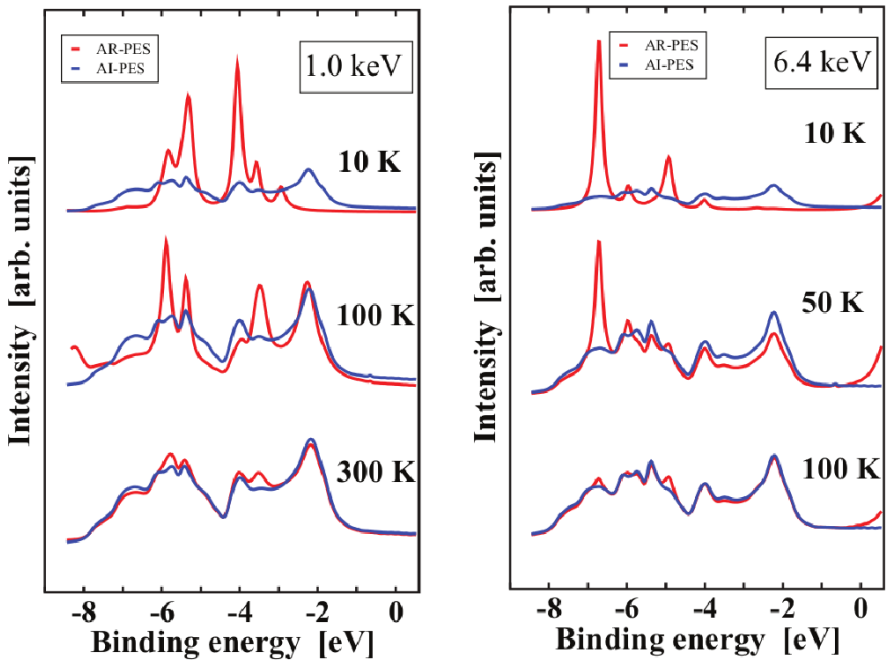

Figure 38. Calculated photoemission spectra for Au(111) at two different excitation energies as a function of temperature. Shown is the comparison between normal emission angle-resolved data (AR-PES, red curves) and corresponding angle- integrated calculations (AI-PES, blue curves). Left panel: Intensity distributions for an excitation energy of 1.0 keV for three temperatures of 10, 100, and 300 K. Right panel: As the left panel, but for an excitation energy of 6.4 keV and a selection of lower temperatures of 10, 50, and 100 K [10].

for normal emission that are labeled AR-PES (red curves) in comparison to 2π angle-integrated PES (AI-PES) intensities (blue curves) at 10, 100, and 300 K. The AI-PES curves are expected to represent very closely the XPS-limit or MEW-DOS results, even at zero temperature, and thus to be only weakly dependent on temperature. While the normal emission AR-PES spectral distribution strongly deviate from AI-PES as a function of binding energy at low temperature, for higher temperatures, the overall shape of the angle-resolved spectra significantly changes approaching the shape of the angle integrated spectra, and showing only small deviations in their intensity profiles. As discussed in Ref. [10], in the case of AI-PES, only phonon-assisted transitions take place producing small temperature-dependent changes in the matrix elements. On the other hand, in the angle-resolved case the temperature-dependent matrix elements are responsible for a decrease of the angle-resolved intensity profiles due to a redistribution of spectral weight. This mechanism, associated with a Debye-Waller-like suppression of the direct part of the photocurrent is primarily responsible for the so called XPS limit in ARPES, which clearly shows up in the left panel of Fig. 38 for 1 keV photon energy at 300 K. The right panel of Fig. 38 shows intensity distributions with an excitation energy of 6.4 keV, demonstrating more dramatic effects at lower temperature, with the XPS limit being reached already at 100 K. Note that a similar behavior was observed, for example, in HAXPES measurements on W(110) and GaAs(100) [129].

Similar trends were demonstrated also for Pt PES. However, the Debye temperature or Pt is much higher than for Au leading to higher Debye-Waller factors than for Au and thus to a preservation of the dispersing features in the spectra.

Fig. 39 shows a direct comparison of the calculated results with experimental data obtained for W(110) with soft x-ray excitation at 870 eV [130] for four different sample temperatures: (a) 300, (b) 470, (c) 607, and (d) 780 K. Experimental results shown in Fig. 39(i) demonstrate dispersive features for all four temperatures, which have a significant smearing as the temperature is raised. Fig. 39(ii) presents fully relativistic one-step calculations accounting for thermal lattice vibrations, whereas Fig. 39(iii) shows conventional one-step calculations in which phonon excitations are more simply considered through a temperature-dependent single-site scattering matrix [131]. Although at the lowest temperature of 300 K, the two different theoretical approaches yield very similar results, as expected for a Debye-Waller factor of 0.70, the temperature dependence of the experimental data is much better described within the temperature-dependent one-step calculations accounting for thermally induced atomic displacements explicitly. The simpler calculation based on the single-site scattering matrix predicts neither the smearing of the dispersing features nor the growth of MEW-DOS features for higher binding energies, but shows instead only the expected decrease of direct transition intensities.

9.1.2. Effect of spin fluctuations in the photoemission spectra of Fe(001) at finite temperature Most theoretical investigations of the photoemission for magnetic systems are based only on the ground-state electronic structure considering either the systems at $T = 0$ K or at temperatures above the critical temperature T_C treating them as non-magnetic (i.e. as Pauli paramagnetic) systems. A generalized spin-density matrix formalism for the photo current was worked out to include thermal spin fluctuations and lattice vibrations on the same level of accuracy making use of the AAM theory. As a consequence, the one-step theory of photoemission accounting for thermal effects can go beyond the FM and PM states, demonstrating that ARPES can distinguish between the different models describing finite-temperature spin correlations, such as the Stoner and Heisenberg models [85].

Fig. 40 represents theoretical LSDA-based spin-resolved photoemission data (left) in comparison with experiment (right), for two different temperatures, $T = 300$ and 900 K. Furthermore, theoretical results for 0 K are shown on the top panel as a reference obtained by using the standard one-step model of photoemission scheme. All spectra have been calculated for normal emission geometry assuming s-polarized light with 60 eV photon energy.

The spin-resolved spectra reveal three main transitions with bulk states as initial states: a minority peak close to the Fermi level and a majority peak at -2.4 eV binding energy, with the initial states having both t_{2g} symmetry. The initial state associated with majority peak at -0.9 eV binding energy has e_g symmetry. More details of the photo emission at $T = 0$ K are discussed in Ref. [85]. Obviously, one can see a reasonably

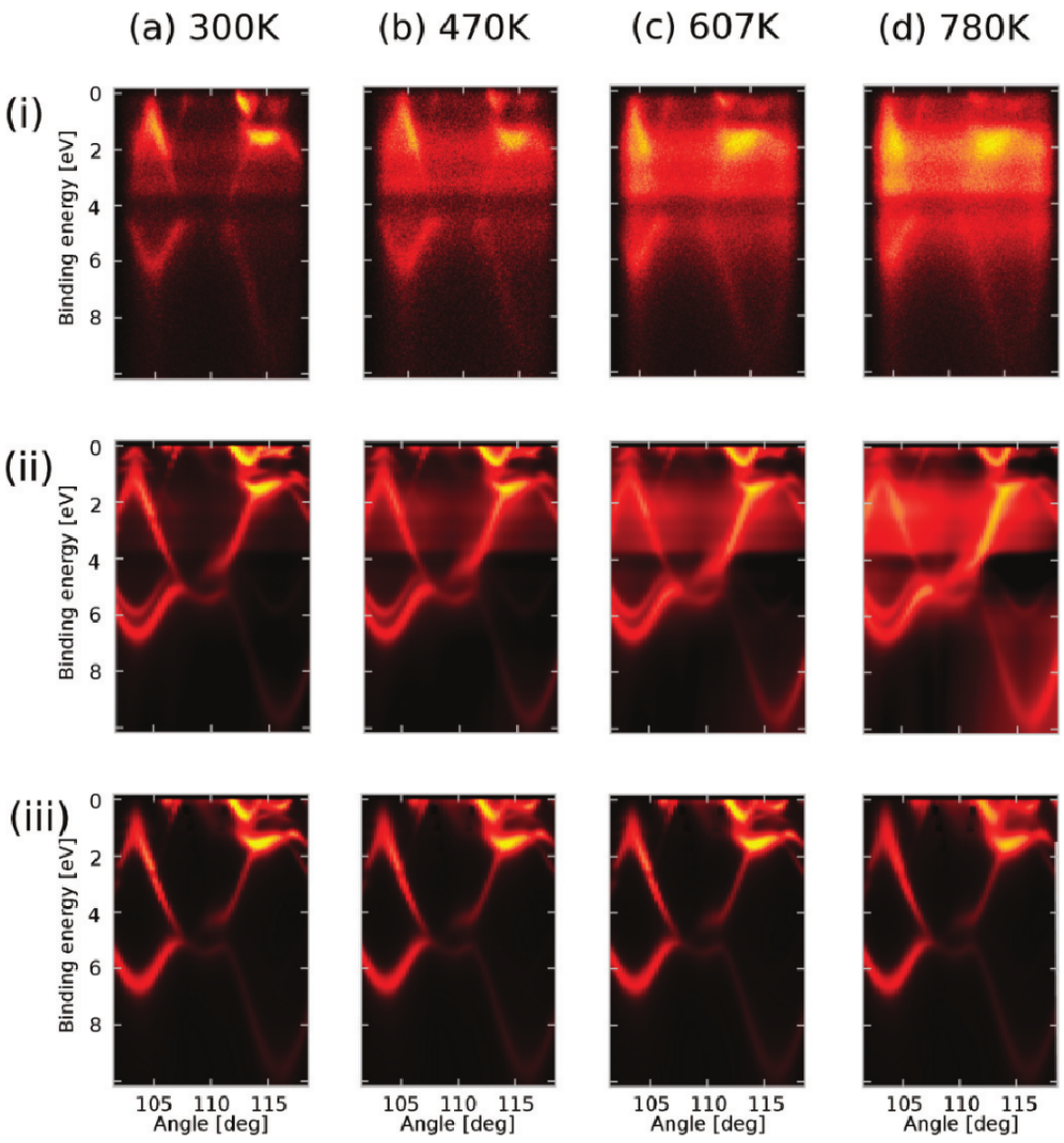

Figure 39. (i) Plots of measured intensity versus angle of emission for 870 eV excitation from the valence bands of W(110) approximately along the $\Gamma - N$ direction for four temperatures of (a) 300, (b) 470, (c) 607, and (d) 870 K (from Ref. [132]), where 90 deg corresponds to normal emission. (ii) Corresponding intensity distributions calculated from temperature-dependent one-step theory based on the CPA formulation. (iii) Conventional ARPES calculations of the direct contribution $I^{DT}(E, \vec{k})$ by use of complex scattering phase shifts and the Debye-Waller model (from Ref. [132]) [10].

good agreement with the experimental spectra. At $T = 900$ K the magnetization of Fe is decreased to roughly about 60% of the value at $T = 300$ K. At high temperature the e_g states are shifted towards the Fermi level. The exchange splitting of the t_{2g} states is reduced, but it still remains very high. In particular, not only a reduction of the exchange splitting is observed, but also an increase of the minority peak intensity at -2.5 and -0.9 eV is found, in accordance with the experimental findings. This results from an increasing contribution from the majority-spin states in line with the discussion in Sec. 4. The overall reduction in the minority-spin intensities at finite

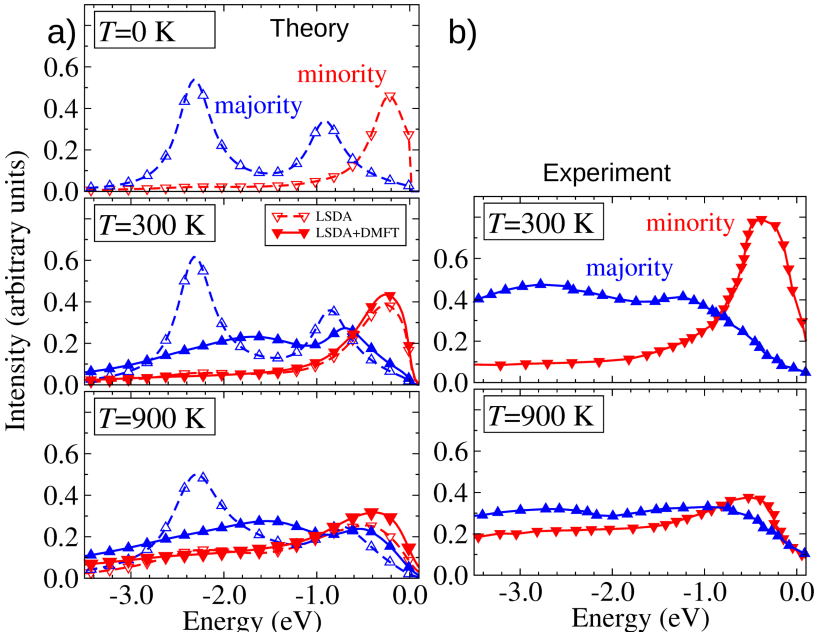

Figure 40. Comparison between experimental (right panels) and theoretical LSDA-based spectra (left panels, dashed lines) and LSDA+DMFT based spectra (left panels, solid lines) for temperature-dependent spin-resolved photoemission at $E_{phot} = 60$ eV and normal emission [85].

temperature is also a result of the varying contribution of the different spin channels to the spin-mixed electronic states. In the calculations we can turn the lattice vibrations or spin fluctuations separately on and off. The main broadening effect in the spectra results from the spin fluctuations, while lattice vibrations have a minor effect on the spin polarization. However, as shown in the case of soft- and hard-x-ray photoemission [10], lattice vibrations will become more noticeable at higher photon energies.

The formalism presented in this paper allows us to model quantitatively and to predict in detail all possible differences in the finite-temperature ARPES spectra accounting for thermal effects using Heisenberg and Stoner models. In the left panels of Fig. 41 are summarized spin-resolved spectra for the Heisenberg model as calculated by making use of the AAM for $T = 300$ and 900 K. In the right panel, calculated spectra are shown for a modified exchange field $B(\vec{r}) = \alpha B(\vec{r})$, where α is a scaling factor which has been chosen in such a way that the local magnetic moment of Fe follows the experimental magnetization curve. One can see significant differences between the two models. Within the Heisenberg model the minority-spin channel develops a second peak at higher binding energy, in this way reflecting the shadow bands and band-mirroring picture. However, the Stoner model leads to a shift in the minority spin states towards higher binding energies.

Finally, as shown in Fig. 42, the results above T_C, based on the Heisenberg model, still leads to a nonzero spin polarization in the spin-resolved ARPES spectra due to the photoemission process. On the other hand, the Stoner model leads to zero spin polarization above T_C and the main intensity is found at a binding energy of about 1 eV. As a consequence, one may state that these explicit spectroscopic calculations provide

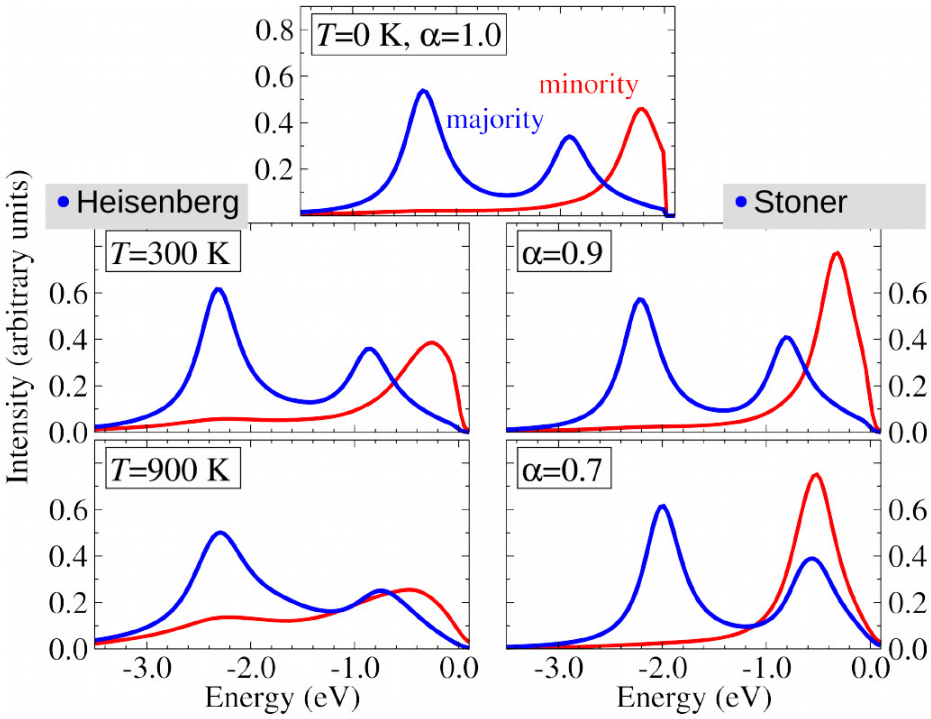

Figure 41. Calculated spin-resolved ARPES spectra for $E_{phot} = 60$ eV and normal geometry. The results in the top panel are calculated spectra for $T = 0$ K. Bottom left panels: calculated LSDA results based on the AAM (Heisenberg model). Bottom right panels: calculated LSDA results applying a modified exchange splitting (Stoner model) [85].

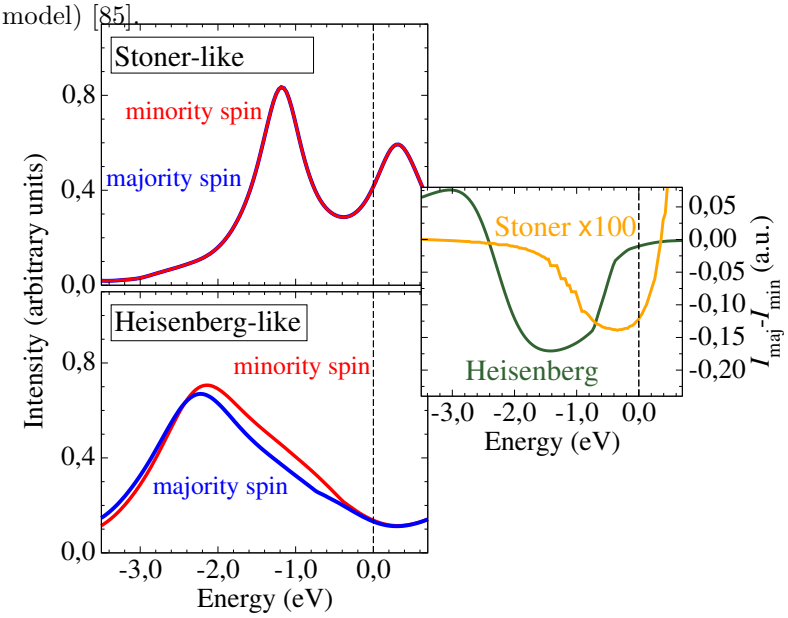

Figure 42. Left panels: Comparison of spin-resolved ARPES intensities between Stoner- and Heisenberg-like models calculated at $T = 1100$ K close to the ferro-to-paramagnetic transition. Right panel: Corresponding spin difference $I_{maj} - I_{min}$ [85].

an adequate tool to distinguish between the various physical mechanisms involved.

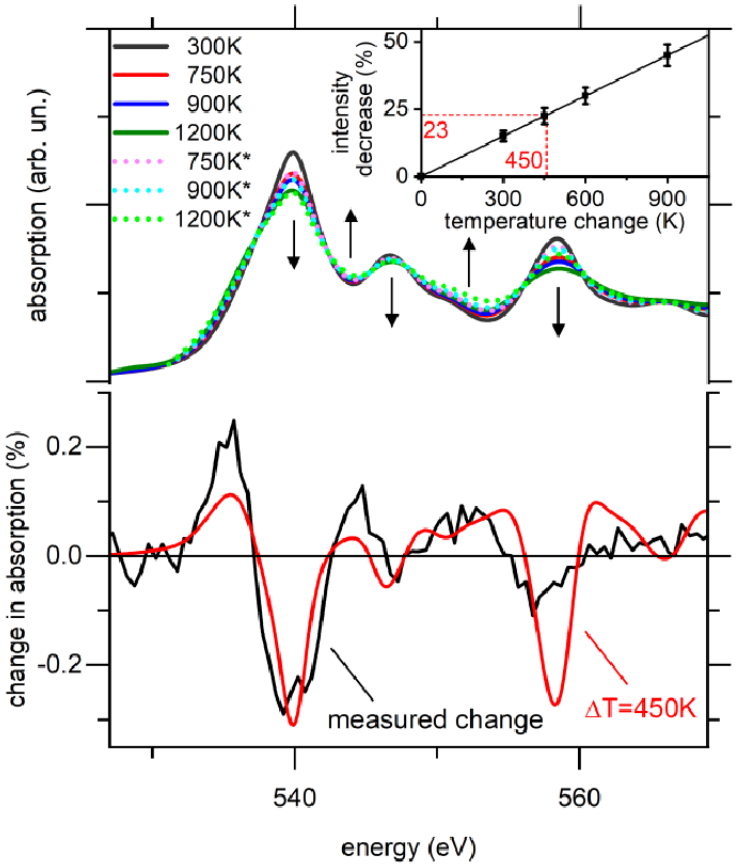

Figure 43. Top: DFT calculations of the O K-edge XAS of bulk MgO at four different temperatures modeled with a finite set of thermal displacements in the framework of the AAM (solid lines). With increasing temperature, the calculation shows an overall intensity suppression of the fine structures. There are well defined energy regions where the XAS at elevated temperature has lower or higher energy than the spectrum at lower temperature, indicated by the arrows. Additionally, spectra generated from the 300 K spectrum using the model discussed in Ref. [133], are shown by dotted lines. Bottom: Comparison of the experimental pump-induced signal (pump fluence 25 mJ/cm^2) with the relative difference of the calculated XAS at 300 and 750 K. For this comparison relative changes after subtraction of a base line are considered [133].

9.2. Effect of lattice vibrations on XAS

The effect of thermal lattice vibrations on transient near-edge x-ray absorption spectra is discussed in Ref. [133]. This work represents the results on time-dependent changes in soft near-edge x-ray absorption spectra (XAS) of an [Fe/MgO]$_8$ metal/insulator heterostructure after laser excitation. The oxygen K-edge absorption of the insulator features a uniform intensity decrease of the fine structure at elevated temperature. The ab initio calculations demonstrate that the transient intensity changes in XAS can be assigned to a transient lattice temperature.

Fig. 43 shows the results of KKR-based DFT calculations of the oxygen K-edge XAS of bulk MgO for different lattice temperatures, which have been obtained making use of the alloy analogy model. The DFT approach applies to larger timescales beyond 20

ps, for which the phonon systems of the individual layers and the entire heterostructure have equilibrated, making a quasi-static description by a common lattice temperature feasible. On these timescales, the lower energy acoustic phonon modes play a dominant role. The calculation shows that with increasing temperature, there is essentially no shifting of the spectral feature at the O K-edge but that the overall fine structures are suppressed in their intensity, in line with experimental results (see Fig. 43). Moreover, the calculation demonstrates that there are indeed defined regions where the XAS at elevated temperature has lower or higher intensity than the spectra at lower temperature, thus supporting others results discussed in Ref. [133]. Consequently, one can relate the magnitude of the intensity suppression to an induced lattice temperature change.

[1] Mankovsky S, Polesya S and Ebert H 2025 *Journal of Physics: Condensed Matter* **37** 315801 URL https://doi.org/10.1088/1361-648X/adf1ce

[2] Halilov S V, Eschrig H, Perlov A Y and Oppeneer P M 1998 *Phys. Rev. B* **58** 293–302 URL http://link.aps.org/doi/10.1103/PhysRevB.58.293

[3] Liu Y, Yuan Z, Wesselink R J H, Starikov A A, van Schilfgaarde M and Kelly P J 2015 *Phys. Rev. B* **91**(22) 220405 URL https://link.aps.org/doi/10.1103/PhysRevB.91.220405

[4] Mahan G D 1993 *Many-particle physics, 2nd ed.* Physics of Solids and Liquids (Plenum Press, New York) URL http://www.springer.com/us/book/9780306434235

[5] Eiguren A, Ambrosch-Draxl C and Echenique P M 2009 *Phys. Rev. B* **79**(24) 245103 URL http://link.aps.org/doi/10.1103/PhysRevB.79.245103

[6] Giustino F 2017 *Rev. Mod. Phys.* **89**(1) 015003 URL https://link.aps.org/doi/10.1103/RevModPhys.89.015003

[7] Gupta R, Abreu J and Verstraete M J 2025 URL https://arxiv.org/abs/2509.10192

[8] Oliva I G, Tillack S, Caruso F, Pavone P and Draxl C 2025 URL https://doi.org/10.48550/arXiv.2511.05781

[9] Migdal A B 1985 *JETP (Sov. ZhETF)* **7**(6) 996

[10] Braun J, Minár J, Mankovsky S, Strocov V N, Brookes N B, Plucinski L, Schneider C M, Fadley C S and Ebert H 2013 *Phys. Rev. B* **88**(20) 205409 URL http://link.aps.org/doi/10.1103/PhysRevB.88.205409

[11] Kumar A, Kumar S, Miyai Y and Shimada K 2022 *Phys. Rev. B* **106**(12) L121104 URL https://link.aps.org/doi/10.1103/PhysRevB.106.L121104

[12] Akhmetov F, Milov I, Makhotkin I A, Ackermann M and Vorberger J 2023 *Phys. Rev. B* **108**(21) 214301 URL https://link.aps.org/doi/10.1103/PhysRevB.108.214301

[13] Irkhin V Y and Katsnelson M I 1990 *Journal of Physics: Condensed Matter* **2** 7151 URL https://doi.org/10.1088/0953-8984/2/34/009

[14] Andres B, Weinelt M, Ebert H, Braun J, Aperis A and Oppeneer P M 2022 *Applied Physics Letters* **120** 202404 URL https://doi.org/10.1063/5.0089688

[15] Lihm J M and Park C H 2020 *Phys. Rev. B* **101**(12) 121102 URL https://link.aps.org/doi/10.1103/PhysRevB.101.121102

[16] Reinert F, Eltner B, Nicolay G, Ehm D, Schmidt S and Hüfner S 2003 *Phys. Rev. Lett.* **91**(18) 186406 URL http://link.aps.org/doi/10.1103/PhysRevLett.91.186406

[17] J S L and Ziman J 1963 *The Electron-Phonon Interaction* (*Solid State Physics* vol 15) (New York, London: Academic Press Inc.) p 221

[18] Savrasov S Y and Savrasov D Y 1996 *Phys. Rev. B* **54** 16487–16501 URL http://link.aps.org/doi/10.1103/PhysRevB.54.16487

[19] Mustafa J I, Bernardi M, Neaton J B and Louie S G 2016 *Phys. Rev. B* **94**(15) 155105 URL https://link.aps.org/doi/10.1103/PhysRevB.94.155105

[20] Fan D D, Liu H J, Cheng L, Liang J H and Jiang P H 2018 *J. Mater. Chem. A* **6**(25) 12125–12131 URL http://dx.doi.org/10.1039/C8TA01806E

[21] Vila F D, Rehr J J, Rossner H H and Krappe H J 2007 *Phys. Rev. B* **76**(1) 014301 URL https://link.aps.org/doi/10.1103/PhysRevB.76.014301

[22] Fujikawa T and Arai H 2002 *J. Electron. Spectrosc. Relat. Phenom.* **123** 19 – 46 URL http://www.sciencedirect.com/science/article/pii/S036820480100370X

[23] Fujikawa T, Sakuma H, Niki K and Sébilleau D 2015 *Journal of Electron Spectroscopy and Related Phenomena* **198** 57–67 URL https://univ-rennes.hal.science/hal-01109966

[24] Hubbard J 1963 *Proceedings of the Royal Society of London. A. Mathematical and Physical Sciences* **276** 238–257 URL https://doi.org/10.1098/rspa.1963.0204

[25] Hubbard J 1964 *Proceedings of the Royal Society of London. A. Mathematical and Physical Sciences* **281** 401–419 URL https://doi.org/10.1098/rspa.1964.0190

[26] Fukuyama H and Ehrenreich H 1973 *Phys. Rev. B* **7**(7) 3266–3273 URL https://link.aps.org/doi/10.1103/PhysRevB.7.3266

[27] Brouers F and Ducastelle F 1975 *J. Phys. France* **36** 851–858 URL https://doi.org/10.1051/jphys:01975003609085100

[28] Lacroix-Lyon-Caen C and Cyrot M 1977 *Solid State Communications* **21** 837–840 URL https://www.sciencedirect.com/science/article/pii/0038109877911668

[29] http://psi-k.net/software/

[30] Economou E N 2006 *Green's Functions in Quantum Physics* (*Springer Series in Solid-state Sciences* vol 7) (Berlin: Springer)

[31] Faulkner J S and Stocks G M 1980 *Phys. Rev. B* **21** 3222–3244 URL http://link.aps.org/doi/10.1103/PhysRevB.21.3222

[32] Weinberger P 1990 *Electron Scattering Theory for Ordered and Disordered Matter* (Oxford: Oxford University Press)

[33] Ebert H 2000 *Electronic Structure and Physical Properties of Solids* (*Lecture Notes in Physics* vol 535) ed Dreyssé H (Berlin: Springer) p 191

[34] Ebert H, Ködderitzsch D and Minár J 2011 *Rep. Prog. Phys.* **74** 096501 URL http://stacks.iop.org/0034-4885/74/i=9/a=096501

[35] Rose M E 1961 *Relativistic Electron Theory* (New York: Wiley)

[36] Faulkner J S 1977 *J. Phys. C: Solid State Phys.* **10** 4661–70 URL http://dx.doi.org/10.1088/0022-3719/10/23/003

[37] Gonis A and Butler W H 1999 *Multiple scattering in solids* Graduate Texts in Contemporary Physics (Berlin: Springer) URL http://www.springer.com/materials/book/978-0-387-98853-5

[38] Zabloudil J, Hammerling R, Szunyogh L and Weinberger P 2005 *Electron Scattering in Solid Matter* (*A Theoretical and Computational Treatise of Springer Series in Solid-state Sciences* vol 147) (Berlin: Springer) URL http://www.springer.com/materials/book/978-3-540-22524-9

[39] Faulkner J S 1982 *Prog. Mater. Sci.* **27** 1 – 187 URL http://www.sciencedirect.com/science/article/B6TX1-48KNR72-9/2/27d1da5fe007d87258daf6a95e657d12

[40] Soven P 1967 *Phys. Rev.* **156** 809–813 URL http://link.aps.org/doi/10.1103/PhysRev.156.809

[41] Ebert H, Vernes A and Banhart J 1997 *Properties of Complex Inorganic Solids* ed Gonis A, Meike A and Turchi P E A (New York: Plenum Press) p 283

[42] H Ebert et al 2017 *The Munich SPR-KKR package*, version 7.7, https://www.ebert.cup.uni-muenchen.de/en/software-en/13-sprkkr URL https://www.ebert.cup.uni-muenchen.de/en/software-en/13-sprkkr

[43] Butler W H and Stocks G M 1984 *Phys. Rev. B* **29** 4217–4223 URL http://link.aps.org/doi/10.1103/PhysRevB.29.4217

[44] Ebert H, Mankovsky S, Chadova K, Polesya S, Minár J and Ködderitzsch D 2015 *Phys. Rev. B* **91** 165132 URL http://journals.aps.org/prb/abstract/10.1103/PhysRevB.91.165132

[45] Kubo R 1957 *J. Phys. Soc. Japan* **12** 570 URL http://jpsj.ipap.jp/link?JPSJ/12/570/

[46] Bastin A, Lewiner C, Betbeder-matibet O and Nozieres P 1971 *Journal of Physics and Chemistry of Solids* **32** 1811 – 1824 URL http://www.sciencedirect.com/science/article/pii/S0022369771801476

[47] Středa P 1982 *J. Phys. C: Solid State Phys.* **15** L717

[48] Greenwood D A 1958 *Proc. Phys. Soc.* **71** 585 URL http://iopscience.iop.org/article/10.1088/0370-1328/71/4/306/meta

[49] Lowitzer S, Ködderitzsch D and Ebert H 2010 *Phys. Rev. Lett.* **105** 266604 URL http://link.aps.org/doi/10.1103/PhysRevLett.105.266604

[50] Lowitzer S, Gradhand M, Ködderitzsch D, Fedorov D V, Mertig I and Ebert H 2011 *Phys. Rev. Lett.* **106** 056601 URL http://link.aps.org/doi/10.1103/PhysRevLett.106.056601

[51] Butler W H 1985 *Phys. Rev. B* **31** 3260–3277 URL http://link.aps.org/doi/10.1103/PhysRevB.31.3260

[52] Ködderitzsch D, Lowitzer S, Staunton J B and Ebert H 2011 *phys. stat. sol. (b)* **248** 2248 URL http://dx.doi.org/10.1002/pssb.201147097
[53] Turek I, Kudrnovský J, Drchal V and Weinberger P 2004 *J. Phys.: Cond. Mat.* **16** S5607 URL http://stacks.iop.org/0953-8984/16/i=48/a=017
[54] Lowitzer S, Ködderitzsch D and Ebert H 2010 *Phys. Rev. B* **82** 140402(R) URL http://link.aps.org/doi/10.1103/PhysRevB.82.140402
[55] Turek I, Kudrnovský J and Drchal V 2019 *Phys. Rev. B* **100**(13) 134435 URL https://link.aps.org/doi/10.1103/PhysRevB.100.134435
[56] Matveev V A and Fedorov G V 1982 *Fiz. Met. Metalloved* **53** 34
[57] Ebert H, Mankovsky S, Ködderitzsch D and Kelly P J 2011 *Phys. Rev. Lett.* **107** 066603 URL http://link.aps.org/doi/10.1103/PhysRevLett.107.066603
[58] Ebert H and Mankovsky S 2009 *Phys. Rev. B* **79** 045209 URL http://link.aps.org/doi/10.1103/PhysRevB.79.045209
[59] Mankovsky S, Ködderitzsch D, Woltersdorf G and Ebert H 2013 *Phys. Rev. B* **87**(1) 014430 URL http://link.aps.org/doi/10.1103/PhysRevB.87.014430
[60] Gilmore K, Idzerda Y U and Stiles M D 2007 *Phys. Rev. Lett.* **99** 027204 URL http://link.aps.org/doi/10.1103/PhysRevLett.99.027204
[61] Tserkovnyak Y, Fiete G A and Halperin B I 2004 *Appl. Physics Lett.* **84** 5234 URL http://link.aip.org/link/?APL/84/5234/1
[62] Böttger H 1983 *Principles of the theory of lattice dynamics* (Berlin: Akademie-Verlag)
[63] Gololobov E M, Mager E L, Mezhevich Z V and Pan L K 1983 *phys. stat. sol. (b)* **119** K139
[64] Agafonov A I 2015 *International Journal of Modern Physics B* **29** 1550206 URL https://doi.org/10.1142/S0217979215502069
[65] Francisco E, Blanco M A and Sanjurjo G 2001 *Phys. Rev. B* **63**(9) 094107 URL http://link.aps.org/doi/10.1103/PhysRevB.63.094107
[66] Papanikolaou N, Zeller R, Dederichs P H and Stefanou N 1997 *Phys. Rev. B* **55** 4157–4167 URL http://link.aps.org/doi/10.1103/PhysRevB.55.4157
[67] Lodder A 1976 *J. Phys. F: Met. Phys.* **6** 1885 URL http://stacks.iop.org/0305-4608/6/i=10/a=018
[68] Velický B 1969 *Phys. Rev.* **184** 614–627 URL http://link.aps.org/doi/10.1103/PhysRev.184.614
[69] Starikov A A, Liu Y, Yuan Z and Kelly P J 2018 *Phys. Rev. B* **97**(21) 214415 URL https://link.aps.org/doi/10.1103/PhysRevB.97.214415
[70] Liechtenstein A I, Katsnelson M I, Antropov V P and Gubanov V A 1987 *J. Magn. Magn. Materials* **67** 65 URL http://www.sciencedirect.com/science/article/pii/0304885387907219
[71] Udvardi L, Szunyogh L, Palotás K and Weinberger P 2003 *Phys. Rev. B* **68** 104436 URL http://link.aps.org/doi/10.1103/PhysRevB.68.104436
[72] Gyorffy B L, Pindor A J, Staunton J, Stocks G M and Winter H 1985 *J. Phys. F: Met. Phys.* **15** 1337 URL http://stacks.iop.org/0305-4608/15/i=6/a=018
[73] Mankovsky S, Polesya S, Ebert H, Bensch W, Mathon O, Pascarelli S and Minár J 2013 *Phys. Rev. B* **88**(18) 184108 URL http://link.aps.org/doi/10.1103/PhysRevB.88.184108
[74] Tikadzumi S 1964 *Physics of Magnetism* (Ney York: Willey)
[75] Akai H and Dederichs P H 1993 *Phys. Rev. B* **47** 8739–8747 URL http://link.aps.org/doi/10.1103/PhysRevB.47.8739
[76] Akai H 1998 *Phys. Rev. Lett.* **81** 3002–3005 URL http://link.aps.org/doi/10.1103/PhysRevLett.81.3002
[77] Staunton J B, Ostanin S, Razee S S A, Gyorffy B L, Szunyogh L, Ginatempo B and Bruno E 2004 *Phys. Rev. Lett.* **93**(25) 257204 URL http://link.aps.org/doi/10.1103/PhysRevLett.93.257204
[78] Crangle J and Goodman G M 1971 *Proc. Roy. Soc. (London) A* **321** 477–491 URL http:

//rspa.royalsocietypublishing.org/content/321/1547/477.abstract
[79] Mankovsky S, Koedderitzsch D and Ebert H 2011 *unpublished*
[80] Ruban A V, Khmelevskyi S, Mohn P and Johansson B 2007 *Phys. Rev. B* **75**(5) 054402 URL http://link.aps.org/doi/10.1103/PhysRevB.75.054402
[81] Drchal V, Kudrnovský J and Turek I 2013 *EPJ Web of Conferences* **40** 11001 URL http://dx.doi.org/10.1051/epjconf/20134011001
[82] Drchal V, Kudrnovský J and Turek I 2013 *Journal of Superconductivity and Novel Magnetism* **26** 1997–2000 URL http://dx.doi.org/10.1007/s10948-012-2082-3
[83] Staunton J B, Banerjee dos Santos Dias M, Deak A and Szunyogh L 2014 *Phys. Rev. B* **89**(5) 054427 URL http://link.aps.org/doi/10.1103/PhysRevB.89.054427
[84] Mankovsky S and Ebert H 2024 *Phys. Rev. B* **110**(18) 184417 URL https://link.aps.org/doi/10.1103/PhysRevB.110.184417
[85] Minár J, Mankovsky S, Braun J and Ebert H 2020 *Phys. Rev. B* **102**(3) 035107 URL https://link.aps.org/doi/10.1103/PhysRevB.102.035107
[86] Buruzs A, Szunyogh L and Weinberger P 2008 *Phil. Mag.* **88** 2615–26 URL http://dx.doi.org/10.1080/14786430802438200
[87] Ridley N and Stuart H 1968 *Journal of Physics D: Applied Physics* **1** 1291–1295
[88] Mankovsky S, Lange H, Polesya S and Ebert H 2023 *Phys. Rev. B* **107**(14) 144428 URL https://link.aps.org/doi/10.1103/PhysRevB.107.144428
[89] Mankovsky S, Polesya S and Ebert H 2020 *Phys. Rev. B* **102**(13) 134434 URL https://link.aps.org/doi/10.1103/PhysRevB.102.134434
[90] Bass J 1982 *Electrical Resistivity of Pure Metals and Alloys* Landolt-Bornstein New Series, Group III, Part (a), Vol. 15 (Springer, New York)
[91] Crépieux A and Bruno P 2001 *Phys. Rev. B* **64** 094434 URL http://link.aps.org/doi/10.1103/PhysRevB.64.094434
[92] Kontani H, Tanaka T, Hirashima D S, Yamada K and Inoue J 2009 *Phys. Rev. Lett.* **102**(1) 016601 URL http://link.aps.org/doi/10.1103/PhysRevLett.102.016601
[93] Go D, Jo D, Lee H W, Kl????ui M and Mokrousov Y 2021 *Europhysics Letters* **135** 37001 URL https://dx.doi.org/10.1209/0295-5075/ac2653
[94] Go D, Lee H W, Oppeneer P M, Blügel S and Mokrousov Y 2024 *Phys. Rev. B* **109**(17) 174435 URL https://link.aps.org/doi/10.1103/PhysRevB.109.174435
[95] Tang P and Bauer G E W 2024 Role of disorder in the intrinsic orbital hall effect (*Preprint* 2401.17620)
[96] Han S, Lee H W and Kim K W 2023 *Current Applied Physics* **50** 13–24 URL https://www.sciencedirect.com/science/article/pii/S1567173923000597
[97] Samolyuk G D, Mu S, May A F, Sales B C, Wimmer S, Mankovsky S, Ebert H and Stocks G M 2018 Temperature dependent electronic transport in concentrated solid solutions of the 3*d*-transition metals ni, fe, co and cr from first principles URL https://link.aps.org/doi/10.1103/PhysRevB.98.165141
[98] Mu S, Yin J, Samolyuk G D, Wimmer S, Pei Z, Eisenbach M, Mankovsky S, Ebert H and Stocks G M 2019 *Phys. Rev. Materials* **3**(1) 014411 URL https://link.aps.org/doi/10.1103/PhysRevMaterials.3.014411
[99] Banhart J, Ebert H, Weinberger P and Voitländer J 1994 *Phys. Rev. B* **50**(4) 2104–2109 URL http://link.aps.org/doi/10.1103/PhysRevB.50.2104
[100] Kudrnovský J, Drchal V, Turek I, Khmelevskyi S, Glasbrenner J K and Belashchenko K D 2012 *Phys. Rev. B* **86**(14) 144423 URL http://link.aps.org/doi/10.1103/PhysRevB.86.144423
[101] Ho C Y, Ackerman M W, Wu K Y, Havill T N, Bogaard R H, Matula R A, Oh S G and James H M 1983 *J. Phys. Chem. Ref. Data* **12** 183 URL http://link.aip.org/link/JPCRBU/v12/i2/p183/s1
[102] Chadova K, Mankovsky S, Minár J and Ebert H 2017 *Phys. Rev. B* **95**(12) 125109 URL https://link.aps.org/doi/10.1103/PhysRevB.95.125109

[103] Nigh H E, Legvold S and Spedding F H 1963 *Phys. Rev.* **132**(3) 1092–1097 URL http://link.aps.org/doi/10.1103/PhysRev.132.1092
[104] Glasbrenner J K, Pujari B S and Belashchenko K D 2014 *Phys. Rev. B* **89**(17) 174408 URL http://link.aps.org/doi/10.1103/PhysRevB.89.174408
[105] Asomoza R, Fert A and Reich R 1983 *J. Less-Common Met.* **90** 177–201 URL http://www.sciencedirect.com/science/article/pii/0022508883900681
[106] Babushkina N 1966 *Sov. Phys. - Solid State* **7** 2450
[107] Lee R S and Legvold S 1967 *Phys. Rev.* **162**(2) 431–435 URL http://link.aps.org/doi/10.1103/PhysRev.162.431
[108] Volkenshtein N V, Grigorova I K and Fedorov G V 1966 *JEPT* **23** 1003
[109] Mankovsky S, Polesya S, Chadova K, Ebert H, Staunton J B, Gruenbaum T, Schoen M A W, Back C H, Chen X Z and Song C 2017 *Phys. Rev. B* **95**(15) 155139 URL https://link.aps.org/doi/10.1103/PhysRevB.95.155139
[110] Polesya S, Mankovsky S, Ködderitzsch D, Minár J and Ebert H 2015 *Cond. Mat. arXiv*
[111] Baranov N and Barabanova E 1995 *Journal of Alloys and Compounds* **219** 139 – 148 URL http://www.sciencedirect.com/science/article/pii/0925838894013756
[112] Mott N F 1964 *Adv. Phys.* **13** 325
[113] Tsymbal E Y, Pettifor D G and Maekawa S 2012 *Giant Magnetoresistance: Theory* (New York: Taylor and Francis Group)
[114] Kobayashi Y, Muta K and Asai K 2001 *Journal of Physics: Condensed Matter* **13** 3335 URL http://stacks.iop.org/0953-8984/13/i=14/a=308
[115] Mankovsky S, Chadova K, Ködderitzsch D, Minár J, Ebert H and Bensch W 2015 *Phys. Rev. B* **92**(14) 144413 URL http://link.aps.org/doi/10.1103/PhysRevB.92.144413
[116] Kim C, Kim C, Kim S and Hahn E 2012 *Journal of the Korean Physical Society* **60** 79–82 URL http://dx.doi.org/10.3938/jkps.60.79
[117] Eibschütz M, Mahajan S, DiSalvo F J, Hull G W and Waszczak J V 1981 *Journal of Applied Physics* **52** 2098–2100 URL http://scitation.aip.org/content/aip/journal/jap/52/3/10.1063/1.329629
[118] Dijkstra J, Zijlema P J, van Bruggen C F, Haas C and de Groot R A 1989 *J. Phys.: Cond. Mat.* **1** 6363 URL http://stacks.iop.org/0953-8984/1/i=36/a=005
[119] Šipr O, Wimmer S, Mankovsky S and Ebert H 2020 *Phys. Rev. B* **101**(8) 085109 URL https://link.aps.org/doi/10.1103/PhysRevB.101.085109
[120] Bhagat S M and Lubitz P 1974 *Phys. Rev. B* **10** 179
[121] Woltersdorf G *Privat communication*
[122] Heinrich B and Frait Z 1966 *phys. stat. sol. (b)* **16** K11 URL http://dx.doi.org/10.1002/pssb.19660160138
[123] Pendry J B 1976 *Surf. Sci.* **57** 679–705 URL http://www.sciencedirect.com/science/article/B6TVX-46SWPX8-CJ/2/ab2f0c8a362abbdd24b4039d7fb1cf6e
[124] Braun J 1996 *Rep. Prog. Phys.* **59** 1267 URL http://stacks.iop.org/0034-4885/59/i=10/a=002
[125] Durham P J, Temmerman W M, Larsson C G and Nilsson P O 1983 *Vacuum* **33** 771–4
[126] Braun J, Minár J, Matthes F, Schneider C M and Ebert H 2010 *Phys. Rev. B* **82** 024411 URL http://link.aps.org/doi/10.1103/PhysRevB.82.024411
[127] Ginatempo B, Durham P J and Gyorffy B I 1989 *J. Phys.: Cond. Mat.* **1** 6483 URL http://stacks.iop.org/0953-8984/1/i=36/a=016
[128] Durham P J 1981 *J. Phys. F: Met. Phys.* **11** 2475 URL http://stacks.iop.org/0305-4608/11/i=11/a=027
[129] Gray A X, Papp C, Ueda S, Balke B, Yamashita Y, Plucinski L, Minár J, Braun J, Ylvisaker E R, Schneider C M, Pickett W E, Ebert H, Kobayashi K and Fadley C S 2011 *Nature Materials* **10** 759 URL http://www.nature.com/nmat/journal/vaop/ncurrent/full/nmat3089.html
[130] Plucinski L, Minár J, Sell B C, Braun J, Ebert H, Schneider C M and Fadley C S 2008 *Phys.*

Rev. B **78** 035108 URL http://link.aps.org/doi/10.1103/PhysRevB.78.035108

[131] Paniago R, Matzdorf R, Meister G, Goldmann A, Braun J and Borstel G 1996 *Surface Science* **347** 46–52 URL https://www.sciencedirect.com/science/article/pii/0039602895009744

[132] Søndergaard C, Hofmann P, Schultz C, Moreno M S, Gayone J E, Vicente Alvarez M A, Zampieri G, Lizzit S and Baraldi A 2001 *Phys. Rev. B* **63**(23) 233102 URL http://link.aps.org/doi/10.1103/PhysRevB.63.233102

[133] Rothenbach N, Gruner M E, Ollefs K, Schmitz-Antoniak C, Salamon S, Zhou P, Li R, Mo M, Park S, Shen X, Weathersby S, Yang J, Wang X J, Šipr O, Ebert H, Sokolowski-Tinten K, Pentcheva R, Bovensiepen U, Eschenlohr A and Wende H 2021 *Phys. Rev. B* **104**(14) 144302 URL https://link.aps.org/doi/10.1103/PhysRevB.104.144302